AREAL GEAR METROLOGY WITH MODIFIED FLANKS

by

Kang Ni

A dissertation submitted to the faculty of
The University of North Carolina at Charlotte
in partial fulfillment of the requirements
for the degree of Doctor of Philosophy in
Mechanical Engineering

Charlotte

2017

Approved by:

_____
Dr. Gert Goch

_____
Dr. John C. Ziegert

_____
Dr. Christopher J. Evans

_____
Dr. Edward P. Morse

_____
Dr. Stuart T. Smith

_____
Dr. Tsinghua Her

_____
Dr. Gregory J. Gbur

©2017
Kang Ni
ALL RIGHTS RESERVED

ABSTRACT

KANG NI. Areal gear metrology with modified flanks. (Under the direction of DR.-ING. GERT GOCH)

Gears are critical mechanical components in power transmission systems, used across a board spectrum of industries such as automobile, aerospace and renewable energy. Given the advancement of design and manufacture of gears in the past decades, the current gear inspection based on line oriented geometric description and tactile measuring technology has shown several deficiencies (lack of areal information, high cycle time etc.), when assessing complex geometries on gears flanks. Advanced sensing methods can capture dense point clouds on a complete gear body, but no evaluation method is available to extract areal information from these point clouds. This imposes a technical gap for gear manufacturers and users since no quantitative parameters characterize the gear's deviations from its nominal geometry.

An implicit equation, which analytically describes the complete gear geometry including both flanks on all teeth is obtained, as a new interpretation of the plumb line distance equation. No nominal points are needed to obtain an areal distance map, which contains gear modification and deviation information. A set of new areal parameters are defined as an extension of standardized line oriented parameters. A novel evaluation method based on the principle of orthogonal decomposition using 2D Chebyshev polynomials is proposed to extract areal gear characteristics from an areal distance map. Numerical simulations are carried out by three numerical integration algorithms on four types of spatial point distributions, to obtain the areal parameters from discrete areal distance maps. Experimental verification using a calibrated gear modification artifact

compared the new areal parameters with the standardized line oriented parameters. A conformance of ± 1.5 µm between the evaluated areal parameters and the given certified line oriented parameter, obtained on four flank modifications and two pitch modifications, is achieved.

This dissertation offers a foundation for a paradigm shift of gear metrology, particularly gear evaluation algorithms. The proposed method enables an improved evaluation of areal flank data, collected by various sensing principles: tactile, optical and even computed tomography. It can form the basis for further studies of microstructure and surface topography of gear flanks. Thus, the developed evaluation method can improve future gear manufacturing processes and provide a holistic quality assessment of gear products.

ACKNOWLEDGMENTS

Above all, I would love to express my deepest gratitude to Prof. Gert Goch for his guidance, encouragement, and support over the past four years on my study and work. It is he who introduced me to the field of gear metrology, helped me build up the knowledge and skills and mentored me to a researcher. With his vision, intelligence, enthusiasm and dedication, he has set up an example for me to follow in years to come. I learned how to judge a challenge globally, solve a problem locally, articulate an idea cautiously and present a solution confidently from him. It is my great honor to be his first doctoral student in the USA.

I would love to thank Prof. John Ziegert, who enriched my industrial mindset by assigning me many interesting and challenging measurement tasks at the Siemens Large Manufacturing Laboratory. He taught me how to collaborate with engineers from industry without throwing fancy scientific terms. It is such a fun working with him, let alone his continuous financial support from the Siemens funds.

I must thank Prof. Christopher Evans. It is from his lectures that I learned the method of using Zernike polynomials in optics, which inspired me to apply Chebyshev polynomials in gear metrology.

I thank Prof. Edward Morse who offered me a one year Siemens project at my difficult time of transition after my master thesis. He showed how his elegant coding style on Quindos and reminded me every now and then on details I took for granted.

Thank you, Prof. Stuart Smith for kindly accepting my last minute request for serving my committee. It was my greatest pleasure to work with you on the project of "Beautiful Equations" on Facebook during the 2015 calendar year.

Many thanks go to Prof. Tsing-Hua Her for serving my committee member and Prof. Gregory Gbur for serving the Graduate Faculty Representative.

Special thanks due to Ms. Yue Peng, my dearest classmate, teammate, roommate and friend. The time we spent together in office, writing and polishing paper word by word; in lab, tuning and debugging Quindos errors at countless midnights and at home, fighting against each other's idea while cooking food or watching movies, is truly unforgettable. It is her who can always come up with brilliant insights toward gear geometry and solve tricky coding problems. I'm also grateful to Dr. Yuanye Liu, a wonderful roommate, who encouraged me to pursue the idea of applying 2D Chebyshev polynomials to characterize gear flanks given the fact that himself is a bright optical scientist.

Over past years, I was lucky to have many great teammates to work with, namely Mr. Jesse Groover who helped me on proof reading this dissertation and Mr. Qichang Wang who actively participated our weekly group meetings. I also must thank Dr. Anke Guenther for taking care of me during my visit at Wetzlar in early 2014 and for providing gear samples and measurement data while working at Reishauer at Wallisellen-Switzerland. I thank Mr. Kenta Kanto from Nikon Corporation at Yokohama-Japan for his continuous interest on my research by offering us optical gear measurement data from his team. Same appreciation goes to Dr. Uwe Buenting and Dr. Florian Tegeler from Mahr GmhH at Gottingen, Germany for providing measurement data on several gear artifacts.

I appreciate the Center for Precision Metrology (CPM) and the Energy Production and Infrastructure Center (EPIC) at UNC Charlotte and the Affiliates for funding this project. Many thanks go to CPM, MEES and EPIC staff members Dr. Jimmie Miller, Mr. Greg Caskey, Mr. John Brien, Mrs. Tracy Beauregard, Mrs. Robin Moose and Mrs.

Jennifer Chastain and who helped me during my studentship at UNC Charlotte. In particular, it is Jennifer who brought so many homemade cookies and brownies, that made numerous fresh starts of my Mondays!

Lastly, I would like to thank my friends at MEES and CPM since 2010, Dr. Liangyu He, Dr. Mark Rubeo, Dr. Mario Valdes, Dr. Lucas Valdez, Dr. Christopher Tyler, Mr. Michael Uwakwe, Mrs. Xiaoxue Chen, Dr. Hossein Shahinian, Dr. Zahra Hosseinimakarem, Mr. Farid Javidpour, Mr. Hang Yu, Mr. Christopher Hughes, Mr. Deepak Kohli, Mr. Chen Fu, Mr. Wenjun Kang, Mr. Fei Shen who made my life enjoyable in USA.

DEDICATION

To Mom and Dad

献给妈妈、爸爸

TABLE OF CONTENTS

LIST OF FIGURES XIII

LIST OF TABLES XXI

NONMENCLATURE XXIII

LIST OF ABBREVIATIONS XXXI

CHAPTER 1 : INTRODUCTION AND LITERATURES REVIEW 1

1.1 Motivation and background 1

1.2 Conventional measurement and evaluation principles 5

1.2.1 Measurement and evaluation of flank deviations 5

1.2.2 Measurement and evaluation of tooth-to-tooth deviations 7

1.3 Traceability, gear artifact and calibration of gear measuring instruments 9

1.4 Areal measurement of gear flanks 11

1.4.1 Mechanical methods 11

1.4.2 Optical methods 12

1.5 Contributions of this dissertation 15

1.6 Dissertation layout 16

CHAPTER 2 : COMPLETE 3D MODLES OF CYLINDRICAL GEARS 19

2.1 Mathematical description of pure involute geometry 19

2.1.1 2D involute curve as a gear profile 19

2.1.2 3D helical surface as gear flank 22

2.1.3 Surface normal vector and u-v-d system 25

2.2 Analytic formation of flank modifications of cylindrical gears 28

2.3 Distances for characterizing spatial deviations of gear flanks 31

2.3.1 Euclidean distance 32

2.3.2 Projected distance 33

2.3.3 Plumb line distance 34

2.4 Implicit equation for cylindrical gear 37

2.4.1 Implicit equation of individual flank 40

2.4.2 Implicit equation for a complete gear teeth system 40

CHAPTER 3 : APPROXIMATION BY CHEBYSHEV SERIES 45

3.1 Introduction and basic concepts 45

3.1.1 Chebyshev norm and Chebyshev approximation 46

3.1.2 Chebyshev polynomials (1D) 47

3.1.3 1D Chebyshev points 48

3.1.4 Chebyshev series and 1D Chebyshev expansion 49

3.2 Properties of 1D Chebyshev series and physical interpretation 50

3.2.1 Orthogonality 50

3.2.2 Near best approximation 51

3.2.3 Parseval's theorem 51

3.3 Approximation of discrete data by power series 53

3.3.1 Least squares solution of normal equation 54

3.3.2 Coefficients of 1D Chebyshev series and 1D power series 54

3.4 Chebyshev polynomials defined on 2D domain 57

3.4.1 Generation of 2D Chebyshev polynomials 57

3.4.2 Approximation of a bivariate function by 2D Chebyshev series 60

3.4.3 Coefficients of 2D Chebyshev series and 2D power series 60

CHAPTER 4 : FLANK GEOMETRY AND 2D CHEBYSHEV POLYNOMIALS 63

4.1 Areal distance map of gear flank 63

4.2 Areal gear parameters 64

4.2.1 Areal pitch deviations and zero order 2D Chebyshev polynomial 66

4.2.2 Linkage between 2D Chebyshev terms and 1st order flank features 69

4.2.3 Linkage between 2D Chebyshev terms and 2nd order flank features 70

4.3 Orthogonal decomposition of areal distance map 71

4.3.1 Analytic description of flank modifications 72

4.3.2 Conversion from evaluation zone to square zone 73

4.3.3 Calculation of 2D Chebyshev coefficients 75

4.3.4 Converting 2D Chebyshev coefficients to areal gear parameters 76

4.3.5 Numerical verification on a simulated flank 79

4.4 High order 2D Chebyshev polynomials and balancing terms 81

CHAPTER 5 : COMPUTATION OF 2D CHEBYSHEV COEFFICIENTS 83

5.1 Evaluation of double integral on discrete dataset 83

5.1.1 2D Empirical edge method 84

5.1.2 2D Cosine variable method 84

5.1.3 Delaunay Triangulation and numerical integration 85

5.1.4 2D Discrete cosine transform method 87

5.2 Distributions of nominal points on flank 89

5.2.1 Three types of equidistant distribution of spatial points 91

5.2.2 Comparisons of numerical algorithms 94

5.2.3 Random distributed points on flank 97

5.3 Non-orthogonality and post-sampling related issues 99

5.3.1 Loss of orthogonality on pixelated data 99

5.3.2 Sub-flank areal evaluation 103

5.4 Influence of misalignment 108

5.4.1 Areal parameters influenced by translational errors 112

5.4.2 Areal parameters influenced by rotational errors 120

CHAPTER 6 : VALIDATION ON GEAR MODIFICATION ARTIFACT 124

6.1 Conventional measurement of a calibrated modification artifact 124

6.1.1 Alignment and measurement process on Leitz PMMF302016 126

6.1.2 Conventional evaluation on Leitz PMMF302016 128

6.2 Areal measurement of artifact “M” using Leitz PMMF302016 129

6.2.1 Areal evaluation of flank modifications by 2D Chebyshev method 132

6.2.2 Evaluation of pitch modifications 136

CHAPTER 7 : CONCLUSIONS AND FUTURE WORK 143

7.1 Conclusions 143

7.2 Future work 144

7.2.1 Uncertainty analysis 144

7.2.2 Holistic evaluation 145

7.2.3 Function oriented analysis 145

REFERENCES 147

APPENDIX A: DERIVATION OF 3D NOMINAL HELICAL SURFACE 153

APPENDIX B: DERIVATION OF PLUMB LINE DISTANCE 155

LIST OF FIGURES

Figure 1.1: Role of metrology in production engineering (after [7]). 2

Figure 1.2: 3D nominal gear model: (a), geomeric illustration of a nominal flank; (b), mathematical formation of geometric parameters for 3D nominal flank model [10]. 2

Figure 1.3: Separation of geometric deviation for function-oriented evaluations (after [12]). 3

Figure 1.4: Basic kinematic pricniples for conventional gear measurement, (a) profile measurement in transverse plane; (b), al helix/lead measurement (source: Mahr). 5

Figure 1.5: Evaluation of profile deviation with unmodified involute [18]. 6

Figure 1.6: Evaluation of helix deviation with unmodified helix [18]. 6

Figure 1.7: Pitch measurement by tactile sensors: (a), direct measurement of single pitch by relative linear measurment; (b), pitch measurement with single flank contact; (c), pitch measurement with two flank contact [20]. 7

Figure 1.8: Individual single pitch deviation and cumulative pitch deviations [18]. 8

Figure 1.9: Three typical measurement configuration of industrial gear measurement: (a), CMM without rotary table (Leitz PMMF302016); (b), CMM with rotary table (Zeiss Prismo); (c), GMI with rotary table (Klingelnberg P26). 9

Figure 1.10: Hierarchy chain for maintaing traceability of artifacts based gear metrology. 9

Figure 1.11: Feature oriented gear artifacts: (a), involute artifact; (b), helix artifact; (c), pitch artifact; (d), gear segement artifact. 10

Figure 1.12: Geometry oriented artifacts: (a), wedge artifact for helix calibration [27] ; (b), ball plate artifact for pitch calibration [29]; (c), ball plate for bevel gear flank measurement [30]; (d), cylinder artifact for involute measurement [31]. 11

Figure 1.13: Areal flank measurement and evaluation by mechanical rolling test [34]: (a), measurement setup; (b), a measured areal flank map. 12

Figure 1.14. Optical gear flank measurement system: (a), configuration of the fringe projection system and gear sample; (b), a tooth with areal flank measurement (after [38]). 13

Figure 1.15: Instrument configuration of gear measurement systrem and image of measured flank by laser interferometry (after [39]). 13

Figure 1.16: Commercial non-contact gear measuring instruments: (a) MS3D [42]; (b) Nikon HN-C3030 [43]; (c) Gleason 300GMSL [44]. 14

Figure 1.17: Measurement of a gear sample by Nikon HN-C3030: (a), measurement setup; (b), measured point clouds of the gear sample, covering both flanks of all teeth. 14

Figure 2.1: Basic geometry of a 2D involute curve. 20

Figure 2.2: Basic geometric parameters of a nominal spur gear (viewed in transverse plane). 21

Figure 2.3: A right flank of a helical gear in 3D space, edited after [10]. 23

Figure 2.4: Definition of base space width half angle η_b on base circle, tooth thickness half angle ψ on pitch circle and space half angle η on pitch circle. 24

Figure 2.5: Generated teeth of a gear in 3D using parameters in Table 2.1. 25

Figure 2.6: Definition of profile slope modification $C_{H\alpha}$ [15]. 26

Figure 2.7: Illustration of curved coordinates (u,v) for the pure involute and surface normal vector of a spur gear's right flank. 27

Figure 2.8: Typical flank modifications for cylindrical gears in 3D space [15]: (a) profile slope modification, (b) profile crowning modification, (c) tip and root relief, (d) helix slope modifications, (e) helix crowning modification, (f) end relief at top and bottom face. 29

Figure 2.9: Slope and crowning modifications designed in profile direction. 29

Figure 2.10: Slope and crowning modifications designed in helix directions. 30

Figure 2.11: Euclidean distance between nominal point and measured point in a 2D Cartesian coordinate system. 32

Figure 2.12: Projected distance between nominal point and measured point in a 2D Cartesian coordinate system. 33

Figure 2.13: Plumb line distance between measured point and the nominal geometry in a 2D Cartesian coordinate system (nominal point with dashed line box). 35

Figure 2.14: Schematic of the plumb line distance of a measured point P_m in a 3D Cartesian coordinate system. 36

Figure 2.15: Relationship between nominal geometry and measured areal distance map: (a), superimposed deviation and/or modification to a nominal cylindrical gear flank; (b), mathematical conequences of (a) towards the implicit equation of cylindrical gear flank..... 39

Figure 2.16: Simulated nominal points on a flank: (a), in 3D Cartesian coordinate system; (b), the plumb line distance plotted as a function of spatial location in the X-Y plane..... 40

Figure 2.17: The half space angle (η) and the tooth thickness half angle (ψ) on the pitch circle of a counter-clock-wise indexed gear: left flank (dotted line) and right flank (solid line). 41

Figure 2.18: Schematic of the nominal starting angles on right flanks of tooth #1 and #2. 42

Figure 2.19: Schematic of the nominal starting angles on left flanks of tooth #1 and #2. 43

Figure 3.1 The first six terms $T_k(x)$ (k = 0, 1, 2,…, 5) of 1D Chebyshev polynomials..... 48

Figure 3.2: Location of 17 Chebyshev points (red dots) on the interval [-1,1]. 49

Figure 3.3: Comparisons of Chebyshev, Legendre, Jacobi and Gegenbauer polynoimals [53]..... 57

Figure 3.4: First nine terms of low order 2D Chebyshev polynomials..... 59

Figure 4.1: Cacluation of areal distance map: (a), raw measured point cloud on a flank; (b), obtained areal distance map, formed by the calculated plumb line distances from (a). 64

Figure 4.2: Schematic of the pitch circle (black dashed) and the pitch points on consecutive flanks (left and right) in transverse plane. 67

Figure 4.3: Angular offset and constant plumb line distance: (a), nominal and measured points of two involute profiles; (b), calculated plumb line distances for the two sets of simulated involute profiles..... 68

Figure 4.4: Geometric similarity between 2D Chebyshev polynomial and flank modification: (a), the 2D Chebyshev term #0; (b), 3D schematic of the individual cumulative pitch of a right flank, edited after [15]..... 68

Figure 4.5: Geometric similarity between 2D Chebyshev polynomial and flank

modification: (a), The 2D Chebyshev term #1; (b), 3D schematic of a modified flank with only profile slope modification, edited after [15]. 69

Figure 4.6: Geometric similarity between 2D Chebyshev polynomial and flank modification: (a), The 2D Chebyshev term #2; (b), 3D schematic of a modified flank with only helix slope modification , edited after [15]. 70

Figure 4.7: Geometric similarity between 2D Chebyshev polynomial and flank modification: (a), the 2D Chebyshev term #3; (b), 3D schematic of a modified flank with only profile crowning modification, edited after [15]. 70

Figure 4.8: Geometric similarity between 2D Chebyshev polynomial and flank modification: (a), The 2D Chebyshev term #4; (b), 3D schematic of a modified flank with flank twist, edited after [15]. 71

Figure 4.9: Geometric similarity between 2D Chebyshev polynomial and flank modification: (a), The 2D Chebyshev term #5; (b) 3D schematic of a modified flank with only helix crowning modification, edited after [15]. 71

Figure 4.10: Decomposition areal distance map into the first six 2D Chebyshev terms. 72

Figure 4.11: Converting from evaluation range domain: (a) areal flank evaluation range; (b) square domain for calculating the 2D Chebyshev coefficients. 74

Figure 4.12: Relationship between the coefficients of bivariate power polynomials, 2D Chebyshev polynomials and the flank modification and deviation. 79

Figure 4.13: Simulated gear flank with profile slope modification, profile crowning modification, helix slope modification, helix crowing modification, twist and pointwise deviation. 80

Figure 5.1: Illustration of a 2D triangulation of six spatial points in u'-v' plane for the cacluation of the volume of hexahedron. 86

Figure 5.2: Illustration of the calculation of 2D DCT at Chebyshev points: (a), location of 2D Chebyshev points in x and y axes; (b), interpolated surface and sampled data on 2D Chebyshev points..... 88

Figure 5.3: Illustration of nominal points distributions on a pure involute profile in the transverse plane: (a), three characteristic distance features for defining the location of a nominal point; (b), locations of the start and end roll angle on a pure invoute; (c), values of seven simulated start and end roll angles corresponding to each type of point distribution..... 90

Figure 5.4： Illustration of equidistant distribution of nominal points on roll angle (i.e. length of roll): (a) on transverse plane, (b) values of (u, v), (c)

locations in 3D Cartesian coordinate system. 92

Figure 5.5: Illustration of equidistant distribution of nominal on involute arc length: (a), points on transverse plane; (b), values of (u, v) for each nominal point; (c), locations in 3D Cartesian coordinate system. 93

Figure 5.6: Illustration of equidistant distribution of nominal points on radial distance: (a), points on transverse plane; (b), values of (u, v) for each nominal point; (c), location of simulated nominal points in 3D Cartesian coordinate system. 94

Figure 5.7: Computational performance on simulated three types of points distributions: (a), computing time (by the empirical edge method) as a function of points per flank; (b), number of iterations as a function of points per flank. 96

Figure 5.8: Computational performance on simulated three types of points distributions: (a), computational time (by the 2D Cosine variable method) as a function of points per flank; (b), number of iterations as a function of points per flank. 96

Figure 5.9: Computational performance on simulated three types of points distributions: (a), computational time (by the 2D DCT method) as a function of points per flank; (b), number of iterations as a function of points per flank. 97

Figure 5.10: Randomly distributed points (2^{10} points per flank) with simulated modifications: (a), points on a flank; (b), points on a complete gear view (only right flanks are shown). 97

Figure 5.11: Relationship between number of iterations for convergence of the three algorithms as a function of the number of points per flank (random spatial points distribution). 98

Figure 5.12: Computational performance on simulated randomly distributed points on flank: (a), computing time (by the three algorithms) as a function of the number of points; (b), a zoomed in view of (a). 99

Figure 5.13: The relative errors of the calculated 2D Chebyshev coefficients with respect to the nominal values in Table 5.1. 101

Figure 5.14: Flow chart for iterative improvement of areal parameters for single flank. 102

Figure 5.15: Illustration of sub-flank sampling: (a), schematic of a sub-flank of arbitrary shape on the full flank; (b), schematic of a rectangular sub-flank of the full flank. 103

Figure 5.16: Design of sub-flank for simulation: (a), full flank and the locations of six sub-flank zones on a gear flank in u-v domain; (b), locations of sub flank zones on the right flank of a gear in Cartesian coordinate system; (c), evaluation and modification parameters. 104

Figure 5.17: Relative errors of obtained sub-flank areal parameters with respect to full flank areal parameters (2D Emprical edge method). 107

Figure 5.18: Relative errors of obtained sub-flank areal parameters with respect to full flank areal parameters (2D Cosine variable method)..... 107

Figure 5.19: Relative errors of obtained sub-flank areal parameters with respect to full flank areal parameters (2D DCT method)..... 108

Figure 5.20: Computation time for each sub-flank: (a), computation time for each sub-flank zone by three algorithms; (b), number of points percentage for each sub-flank zones with respect to the full flank..... 108

Figure 5.21: Schematic of global coordinate system and workpiece coordinate systems..... 110

Figure 5.22: Simulated translational errors of the origin of the new CSY, relative to the nominal origin of the gear sample in the X directions: (a), -5 μm; (b),+5 μm. 113

Figure 5.23: Change of areal gear parameters under a HTM of simulated translational error by +5 μm in the X axis, according to Figure 5.22 (a)..... 114

Figure 5.24: Change of areal gear parameters under a HTM of simulated translational error by -5 μm in the X axis, according to Figure 5.22 (b)..... 115

Figure 5.25: Simulated translational error of the origin of the CSY, relative to the nominal origin of the gear in the Y directions: (a), +5 μm; (b), -5 μm. 116

Figure 5.26: Change of areal gear parameters under a HTM of simulated translational error by -5 μm in the Y axis, according to Figure 5.25 (a)..... 116

Figure 5.27: Change of areal gear parameters under a HTM of simulated translational error by +5 μm in the Y axis, according to Figure 5.25 (b)..... 117

Figure 5.28: Simulated translational error of the origin of the new CSY, relative to the nominal origin of the gear in both the X direction and the Y direction: (a), -5 μm; (b), +5 μm..... 118

Figure 5.29: Change of areal gear parameters under a HTM of simulated translational error by +5 μm in both the X axis and the Y axis according to Figure 5.28 (a)..... 118

Figure 5.30: Change of areal gear parameters under a HTM of simulated translational error by -5 μm in both the X axis and the Y axis according to Figure 5.28 (b)..... 119

Figure 5.31: Change of areal gear parameters under a HTM of simulated rotational error by -0.01 degree with respect to the X axis..... 121

Figure 5.32: Change of areal gear parameters under a HTM of simulated rotational error by -0.01 degree with respect to the Y axis..... 122

Figure 6.1: Calibrated gear modification artifact: (a), measurement setup of the artifact “M” on Leitz PMMF; (b), basic geometry information of the artifact “M” [71]. 125

Figure 6.2: Specifications of slope and crowning modifications on artifact “M” (selected tooth and amount of modifications in yellow box) [71]..... 125

Figure 6.3: Measurement of datum features on the gear artifact using 8-star-probe: (a), measurement of datum reference plane; (b), locations of the probed points..... 127

Figure 6.4: Measurement setup for mechanical alignment of artifact “M”: (a), probing datum circle C and D on artifact “M”; (b), locations of the probed points. 128

Figure 6.5: Illustration of the workpiece CSY of artifact “M” and the locations of multiple lines on flanks..... 130

Figure 6.6: Raw data on artifact “M”: (a), point cloud of 36 measured left flanks; (b), point cloud of 36 measured right flanks. 132

Figure 6.7: Approximation of areal measurement data of L#10 flank; (a), the original (blue), reconstructed (red), and the residual (green) areal maps; (b), the residual map (green) and reconstructed residual map (red)..... 133

Figure 6.8: Approximation of areal measurement data of L#19 flank; (a), the original (blue), reconstructed (red), and the residual (green) areal maps; (b), the residual map (green) and reconstructed residual map (red)..... 134

Figure 6.9: Approximation of areal measurement data of L#20 flank; (a), the original (blue), reconspectued (red), and residual (green) areal maps; (b), the residual map (green) and reconstructed residual map (red)..... 134

Figure 6.10: Approximation of areal measurement data of L#30 flank; (a), the original (blue), reconstructed (red), and residual areal maps (green); (b), the residual map (green) and the reconstructed residual map (red)..... 135

Figure 6.11: Intended pitch modications of artifact “M”: (a), location of

modifications on the right flanks of tooth #30, #31 and #32; (b), graphical representation of nominal individual cumulative pitch deviation; (c), graphical representation of nominal individual single pitch deviation [71]. 137

Figure 6.12: Conventional pitch deviations from certificate issued by FRENCO [71]: individual cumulative pitch deviation (top); individual single pitch deviation (bottom). 138

Figure 6.13: Conventional pitch deviations measured by Leitz PMMF302012: individual cumulative pitch deviation (top); individual single pitch deviation (bottom). 139

Figure 6.14: Areal pitch deviations calculated by the 2D Chebyshev method from areal measurement point clouds: areal individual cumulative pitch deviation (top); areal individual single pitch deviation (bottom). 139

Figure 6.15: First order areal parameters of 36 right flanks: areal profile slope deviations (top); areal helix slope deviations (bottom). 142

Figure 6.16: Second order areal parameters of 36 right flanks: areal profile crowning (top); areal flank twist (middle); areal helix crowning (bottom). 142

LIST OF TABLES

Table 2.1 Nominal gear parameters for generating gear flanks in Figure 2.5. 24

Table 3.1: Interpretation of mathematical properties and applications of Chebyshev polynomials on areal gear flanks. 52

Table 4.1: Conventional line oriented evaluation parameters [18] and proposed areal evaluation parameters. 65

Table 4.2: First six low order 2D Chebyshev terms and areal gear features. 76

Table 4.3: Simulated nominal and approximated areal flank parameters. 81

Table 4.4: Higher order 2D Chebyshev terms and balancing terms n = 6,7,8,…,15. 82

Table 5.1: The nominal and calculated values of the first five 2D Chebyshev coefficients from a simulated flank with different grid size (unit: μm)..... 100

Table 5.2: Information of rectangular sub-flank zones. 105

Table 5.3: Areal gear parameters calculated from sub-flank data on a simulated gear flank using empirical edge method (5 iterations, unit: μm)..... 106

Table 5.4: Areal gear parameters calculated from sub-flank data on a simulated gear flank using change of cosine variable method (5 iterations, unit: μm). 106

Table 5.5: Areal gear parameters calculated from sub-flank data on simulated gear using 2D DCT method (5 iterations, unit: μm)..... 106

Table 6.1: Certificated line oriented evaluation results of four modifications on “M” [71] (unit: μm). 126

Table 6.2: Typical qualification results (stylus sphericity deviation) of an eight-star probe with eight 1.5 mm diameter styli (unit: μm). 127

Table 6.3. Standard measurements of modification on artifact “M” measured by the CMM (3 repetitions). 129

Table 6.4: Summary of the conventional evaluation of 23 helix lines by Quindos 7 (3 repetitions). 131

Table 6.5: Summary of the conventional evaluation of 99 profile lines by Quindos 7 (3 repetitions). 131

Table 6.6: Comparison of the areal evaluation and the conventional evaluation of the four flank modifications on artifact M. 135

Table 6.7: Comparison of the areal evaluation the conventional evaluation of form deviation of the four flank modifications on artifact M. 136

Table 6.8: Pitch deviations from certificate issued by FRENCO [71] (unit: μm). 138

Table 6.9: Comparison of conventional pitch deviations and areal pitch deviations measured by Leitz PMMF302016 from 3 repetitions (unit: μm). 140

Table 6.10: Areal individual cumulative pitch deviations (F_{pi}^{A}) of the 36 right flanks (tooth #1 to #36) of "M" (unit: μm; value rounded to two digits after the decimal point). 140

Table 6.11: Areal individual single pitch deviations (f_{pi}^{A}) of the 36 right flanks (tooth #1 to #36) of "M" (unit: μm; value rounded to two digits after the decimal point). 141

NONMENCLATURE

P	a mathematical point
X	X-axis of a Cartesian coordinate system
Y	Y-axis of a Cartesian coordinate system
Z	Z-axis of a Cartesian coordinate system
(x, y, z)	3D coordinates of point P in Cartesian coordinate system
x	x coordinate of point P
y	y coordinate of point P
z	z coordinate of point P
(ρ, ϕ, z)	3D coordinate of point P in cylindrical coordinate system
ρ	radial distance from origin to the projection of point P on the X-Y plane
ϕ	azimuth angle between the X-axis and the line connecting the origin and the projection of the point P on the X-Y plane, Counter-Clock-Wise
z	height of point P to the X-Y plane in cylindrical coordinate system
P_{m}	measured point of a gear feature
x_{m}	x coordinate of P_{m} in Cartesian coordinate system
y_{m}	y coordinate of P_{m} in Cartesian coordinate system
z_{m}	z coordinate of P_{m} in Cartesian coordinate system
ρ_{m}	ρ coordinate of P_{m} in cylindrical coordinate system
ϕ_m	ϕ coordinate of P_{m} in cylindrical coordinate system
z_m	z coordinate of P_{m} in cylindrical coordinate system
P_{nom}	a nominal point on a gear feature
x_{nom}	x coordinate of P_{nom} in Cartesian coordinate system
y_{nom}	y coordinate of P_{nom} in Cartesian coordinate system

z_{nom}	z coordinate of P_{nom} in Cartesian coordinate system
ρ_{nom}	ρ coordinate of P_{nom} in cylindrical coordinate system
ϕ_{nom}	ϕ coordinate of P_{nom} in cylindrical coordinate system
z_{nom}	z coordinate of P_{nom} in cylindrical coordinate system
$\vec{p}_{\mathrm{m}}$	spatial vector pointing from the origin to P_{m}
$\vec{p}_{\mathrm{nom}}$	spatial vector pointing from the origin to P_{nom}
$\vec{d}$	deviation vector pointing from nominal point P_{nom} measured point P_{m}
d_{Euc}	the Euclidean distance between two points
$\vec{N}$	surface normal vector
$\lvert\vec{N}\rvert$	magnitude of the surface normal vector
$\vec{n}$	unit surface normal vector
n_{x}	x component of $\vec{n}$
n_{y}	y component of $\vec{n}$
n_{z}	z component of $\vec{n}$
$\vec{d}_{\mathrm{proj}}$	deviation vector projected to the surface normal direction, $\vec{N}$
$\lvert\vec{d}_{\mathrm{proj}}\rvert$	magnitude of the deviation vector $\vec{d}_{\mathrm{proj}}$
$\vec{d}_{\mathrm{lot}}$	deviation vector in the surface normal direction
$\lvert\vec{d}_{\mathrm{lot}}\rvert$	magnitude of the $\vec{d}_{\mathrm{lot}}$ (i.e. plumb line distance)
ξ	roll angle of the involute
ξ_{st}	roll angle corresponding to the start of the profile evaluation range
ξ_{end}	roll angle corresponding to the end of the profile evaluation range
n_{ξ}	number of points for simulated roll angle between ξ_{st} and ξ_{end}
L_{AE}	value of the length of roll (i.e. roll length)

ξ_{AE}	value of roll angle of the points for evenly spaced roll length
L_{inv}	value of the arc length of an involute
ξ_{inv}	value of roll angle of the points for evenly spaced arc length of involute
L_{rad}	value of the radial distance between the origin of base circle to a nominal point on the inovlute
ξ_{rad}	value of roll angle of the points for evenly spaced radial distance
z_{st}	z coordinate corresponding to the start of helix evaluation range
z_{end}	z coordinate corresponding to the end of helix evaluation range
Λ	angle from the X-axis to the start of an involute on the base circle
r_{b}	radius of base circle
r	radius of reference circle
r_{st}	radius corresponding to the starting value of roll angle
r	radius corresponding to the end value of roll engle
d_{a}	tip diameter
d_{f}	root diameter
d_{Fa}	tip form diameter
d_{Ff}	root form diameter
d_{M}	measurement diameter
β_{b}	helical angle at base circle
η_{b}	space width half angle at base circle
α_{t}	transverse pressure angle at reference circle
α_{n}	normal pressure angle
β	helical angle at reference circle
η	space width half angle at reference circle

η_{y}	space width half angle at arbitrary circle
η_{b}	space width half angle of base circle
ψ_{y}	tooth thickness half angle on arbitrary circle
ψ	tooth thickness half angle on the reference circle
m_{n}	normal module
m_{t}	transverse module
τ	angular pitch
p_{t}	transverse pitch on reference cylinder
L_{α}	profile evaluation length
L_{β}	profile evaluation length
$C_{\mathrm{H}\alpha}$	profile slope modification
C_{α}	profile crowning modification
$C_{\mathrm{H}\beta}$	helix slope modification
C_{β}	helix crowning modification
$f_{\mathrm{H}\alpha}$	profile slope deviation
$f_{\mathrm{f}\alpha}$	profile form deviation
F_{α}	total profile deviation
$f_{\mathrm{H}\beta}$	helix slope deviation
$f_{\mathrm{f}\beta}$	helix form deviation
F_{β}	helix deviation
f_{pi}	individual single pitch deviation
F_{pi}	individual cumulative pitch deviation
$C_{\mathrm{H}\alpha}^{\mathrm{A}}$	areal profile slope modification
C_{α}^{A}	areal profile crowning modification

$C_{\mathrm{H}\beta}^{\mathrm{A}}$	areal helix slope modification
C_{β}^{A}	areal helix crowning modification
$S_{\alpha\beta}^{\mathrm{A}}$	areal flank twist coefficient
$f_{\mathrm{H}\alpha}^{\mathrm{A}}$	areal profile slope deviation
$f_{\mathrm{H}\beta}^{\mathrm{A}}$	areal helix slope deviation
$f_{\mathrm{f}}^{\mathrm{A}}$	areal form deviation
$F_{\mathrm{f}}^{\mathrm{A}}$	total areal deviation
$f_{\mathrm{pi}}^{\mathrm{A}}$	areal individual single pitch deviation
$F_{\mathrm{pi}}^{\mathrm{A}}$	areal individual cumulative pitch deviation
c_{t}	tooth countering direction
t_{ind}	tooth index number (t_{ind} = 1, 2, 3, …, z)
f	flank direction
U	U axis of a curvilinear coordinate system
V	V axis of a curvilinear coordinate system
D	D axis of a curvilinear coordinate system
u	surface parametric coordinate of point P of the U axis
v	surface parametric coordinate of point P of the V axis
u_{s}	surface parameter of the start of the profile evaluation range
v_{s}	surface parameter of the start of the helix evaluation range
u_{e}	surface parameter of the end of the profile evaluation range
v_{e}	surface parameter of the end of the helix evaluation range
N_{data}	number of points within an areal distance map for evaluation
u'	mapped u coordinates in the square domain $[-1, 1]^2$
v'	mapped v coordinates in the square domain $[-1, 1]^2$

ε'	numerical edge of the square domain $[-\varepsilon', \varepsilon']^2$
$\theta_{u'}$	angular variable as the arccosine function of u'
$\theta_{v'}$	angular variable as the arccosine function of v'
$A(u)$	profile modification function in 1D
$B(v)$	helix modification function in 1D
$M_{\mathrm{nom}}^{\mathrm{A}}(u, v)$	nominal flank modification function in 2D
$T^{\mathrm{A}}(u, v)$	flank twist function in 2D
$f(x)$	single variable function
$p_N(x)$	single variable function approximated by truncated power series
$p_N^*(x)$	best approximation by power series at the hightest degree of *N*
$E_N(x)$	Residue error after the degree of *N* truncated power series
$f(x_i)$	function value at the abscissa x_i
a_n	coefficient of 1D power series for the term x^n
$f(x, y)$	bivirate function
$f_N(x, y)$	truncated 2D Chebyshev series to the highest degree of *N*
$G_{\mathrm{P}}(x, y)$	bivirate function expanded by 2D power series
$a_{2,n}$	coefficient for the terms in $G_{\mathrm{P}}(x, y)$ series
$a_{2,n}^*$	approximated value for $a_{2,n}$
$T_k(x)$	1D Chebyshev polynomial at the order of *k*
c_k	coefficient of 1D Chebyshev polynomial for the term $T_k(x)$
C	vector of 1D Chebyshev coefficients listed in ascending order
A	vector of 1D power coefficients listed in ascending order
M	square matrix of mapping 1D power coefficients (**C**) to 1D Chebyshev coefficients (**A**)
$C_n(x, y)$	2D Chebyshev polynomial at term *n*

$G_{\mathrm{C}}(x, y)$	bivirate function expanded by 2D Chebyshev series
$c_{2,n}$	coefficient for the 2D Chebyshev term $C_n(x, y)$ in $G_{\mathrm{C}}(x, y)$ series
$c_{2,n}^{*}$	approximated value for $c_{2,n}$
$\mathbf{C_2}$	vector of 2D Chebyshev coefficients listed in ascending order
$\mathbf{A_2}$	vector of 2D power coefficients listed in ascending order
$\mathbf{M_2}$	square matrix of mapping 2D power coefficients ($\mathbf{C_2}$) to 2D Chebyshev coefficients ($\mathbf{A_2}$)
$x_{1\mathrm{D}}(j)$	the j^{th} Chebyshev points on the interval of $[-1, 1]$ defined in X axis
K	1D normalization factor for 1D Chebyshev coefficient
$f_{\mathrm{P}}(x)$	single variable function approximated by truncated power series
$f_{\mathrm{T}}(x)$	single variable function approximated by truncated 1D Chebyshev series
$T_p(x)$	pth 1D Chebyshev polynomial of variable x
p	term index of 1D Chebyshev polynomial of variable x
a_p	p^{th} Chebyshev coefficient for the $T_p(x)$
$T_q(y)$	q^{th} Chebyshev polynomial of variable y
q	term index of 1D Chebyshev polynomial of variable y
a_q	q^{th} Chebyshev coefficient for the $T_q(y)$
(m, n)	element index of a matrix with size of (M, N) in 2D DCT calculation
$f(m, n)$	input matrix for 2D DCT operation
$F_{\mathrm{dct2}}(p, q)$	output matrix of 2D DCT of input $f(m, n)$
α_p	scaling factor for 2D DCT of the column index in $f(m, n)$
α_q	scaling factor for 2D DCT of the row index in $f(m, n)$
$D'(u', v')$	mapped areal distance map in $[-1, 1]^2$ or $[-\varepsilon', \varepsilon']^2$
$C_i'(u', v')$	i^{th} 2D Chebyshev polynomials $[-1, 1]^2$ or $[-\varepsilon', \varepsilon']^2$

A_i	i^{th} 2D Chebyshev coefficient for $C_i(x, y)$ or $C_i'(u', v')$
K_2	2D normalization factor for 2D Chebyshev coefficients
$F(\ldots) = 0$	implicit function of a nominal surface or a complete involute gear teeth
ΔX	Translational error in the X axis
ΔY	Translational error in the Y axis
ΔZ	Translational error in the Z axis
ϵ_{X}	Rotational error with respect to the X axis
ϵ_{Y}	Rotational error with respect to the Y axis
ϵ_{Z}	Rotational error with respect to the Z axis
$\mathbf{T}_{\text{X}}$	HTM for the translational error in X axis
$\mathbf{T}_{\text{Y}}$	HTM for the translational error in Y axis
$\mathbf{T}_{\text{Z}}$	HTM for the translational error in Z axis
$\mathbf{T}_{\epsilon_{\text{x}}}$	HTM for the rotational error with respect to X axis
$\mathbf{T}_{\epsilon_{\text{Y}}}$	HTM for the rotational error with respect to Y axis
$\mathbf{T}_{\epsilon_{\text{Z}}}$	HTM for the rotational error with respect to Z axis
$\delta^{\text{A}}_{f_{\text{pi}}}$	summation of individual areal single pitch deviation normalized to the nnumber of teeth

LIST OF ABBREVIATIONS

1D	One dimension
2D	Two dimension
3D	Three dimension
CW	Clock-wise
CCW	Counter-clock-wise
NMI	National Metrology Institute
PTB	Physikalisch -Technische Bundesanstalt
CSY	Coordinate System
CMM	Coordinate Measuring Machine
GMI	Gear Measuring Instrument
DCT	Discrete Cosine Transform
HTM	Homogenous Transformation Matrix
ISO	International Organization for Standardization
VDI	Verein Deutscher Ingenieure

CHAPTER 1 : INTRODUCTION AND LITERATURES REVIEW

1.1 Motivation and background

Gears are decisive components in power transmission system across automobile, machine tool, aviation and renewable energy industries. The types of gears can be classified by the geometry, namely spur gears, helical gears, bevel gears and worm gears [1]. The cylindrical gear (spur and helical) is one of the most widely used types of gear. Gear designers are confronted with the functional requirements of the gear system such as longer life time, higher power density, lower noise emission and less failure rate [2]. Much research has been performed on gear manufacturing technologies from cutting to finishing, aiming at more efficient, reliable and effective methods to produce gears of high quality [3] [4] [5] [6]. Challenges from the design and manufacturing of gears gradually push the advancement of gear metrology towards the goals of faster, more reliable and more flexible measurement with better accuracy.

Production metrology aims to close the loops between function, design and production by generating quantitative information and knowledge (see Figure 1.1) [7]. Undoubtedly, gear metrology [8] [9] must benefit the whole gear production life cycle economically. Before the introduction of CNC technology in the 1970s, gears were measured by electro-mechanical devices and manual gauging tools. CNC based tactile measuring methods dominate today's industrial solution for gear inspection, which is facing the challenge of micrometer level accuracy grade required by the gear designers and manufacturers.

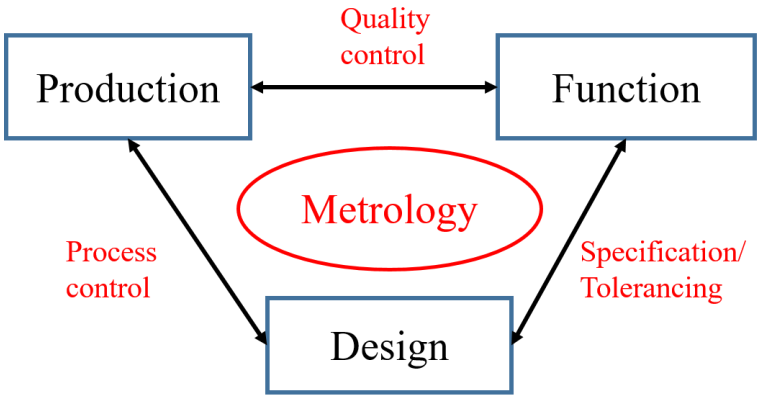

Figure 1.1: Role of metrology in production engineering (after [7]).

To integrate the capability of measuring gears to Coordinate Measuring Machines (CMM), Lotze [10] proposed a mathematical model of 3D helical gear geometry, separating the gear reference elements (center bore, gear axis) from the substitute gear flanks. The pressure angle and the axial position were selected by Lotze as a pair of Gaussian surface parameters to model the nominal flank geometry [10], shown in Figure 1.2. This work established the foundation of using CMMs to measure gears and evaluate gear deviation parameters, since spatial coordinates can be captured on the flanks of a gear.

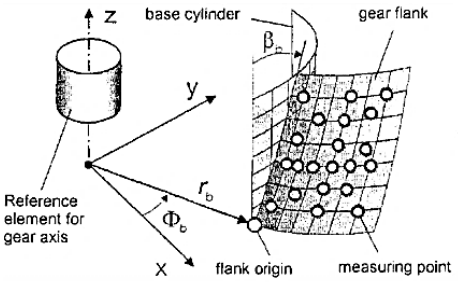

(a)

$$F(\alpha,\zeta)=\begin{pmatrix}x\\y\\z\end{pmatrix}=\begin{pmatrix}r_b\sec\alpha\cos[\varphi_{b0}+C\,\zeta-h\,Ev\alpha]\\r_b\sec\alpha\sin[\varphi_{b0}+C\,\zeta-h\,Ev\alpha]\\\zeta\end{pmatrix} \quad (1)$$

with

$C=\tan(\beta_b)/r_b$	helix coefficient
$Ev(\alpha)=\tan(\alpha)-\alpha$	involute function
r_b	base radius
α,ζ	Gaussian surface parameters (pressure angle, axis co-ordinate)
h	flank direction ($h=\pm1$ for left- and right-hand flank)

(b)

Figure 1.2: 3D nominal gear model: (a), geomeric illustration of a nominal flank; (b), mathematical formation of geometric parameters for 3D nominal flank model [10].

However, mathematical methods for obtaining the gear deviations, namely by conventional optimization methods [11], can only be applied to the chosen parameters in the 3D model.

Pfeifer et al. introduced a series of function oriented quality parameter aiming to characterize different global form deviations from 3D surface measurement data on bevel gears [12]. As shown in Figure 1.3 (a), the separation of topography data measured by a CMM is illustrated. However, the mathematical tool used for this purpose is based on typical second order surfaces (e.g. elliptic paraboloid, hyperbolic paraboloid, ellipsoid) in Figure 1.3 (b), which is not intuitive. In addition, those entities do not resemble the real geometry of the involute gear flank and the implementation algorithm did not offer the calculation of standardized gear parameters.

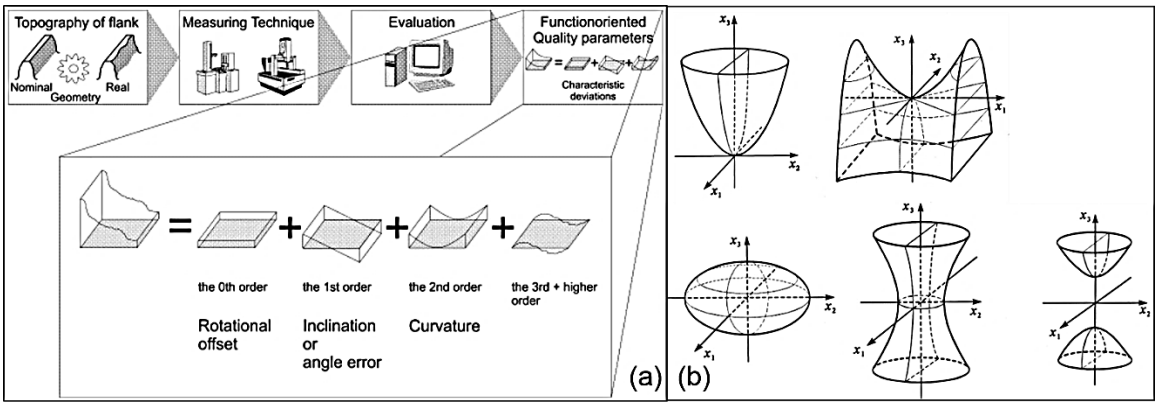

Figure 1.3: Separation of geometric deviation for function-oriented evaluations (after [12]).

Dantan et al. proposed a new way to categorize gear metrology into two types: one is geometrical metrology and the other one is kinematic metrology [13], with an impact on gear specification and tolerancing theories [14]. To meet the specified geometrical tolerances of a gear, the deviations of an individual flank, the deviations between flanks

and the deviations of flanks with respect to the center bore must be measured to meet the conformance requirement of a gear.

As the functional performance (noise emission, transmission error, life time etc.) of a gearing system has become more demanding over the past decades, gear flank modifications were introduced in gear design and application [15]. However, the three geometric modeling methods of gear flank and topography mentioned did not include the analytic description of flank modifications, which have become ubiquitous in today's gear manufacturing practice. Guenther et al. introduced a set of explicit equations for the nominal gear flank modifications in the 2D domain, including profile slope deviation, profile crowning, helix slope deviation and helix crowning [16]. The typical amplitude of a flank modification varies from 1 micrometer to 100 micrometers, depending on the size of a gear and the types of modification. Modified tooth geometry in early stages of a manufacturing process can be used to compensate form deviations, caused by subsequent processes such as hardening or continuous generation grinding [4]. A finished gear with modified tooth geometry can provide smooth and quiet meshing conditions under varying loading circumstances. For example in wind energy system [17], the concentration of contact area near the transverse edges of the tooth caused by misalignment and misplacement can be mitigated by modifications, which leads to an increased lifetime and reduced failure rate. To obtain reliable information of the quality of a gear and to understand the process footprint of a gear manufacturing process, it is essential to quantitatively check the desired flank modifications as well as to assess undesired flank deviations in gear inspection.

1.2 Conventional measurement and evaluation principles

1.2.1 Measurement and evaluation of flank deviations

To measure the deviation of a gear profile, one translational motion (denoted by "Y" in Figure 1.4 (a) and a rotational motion (denoted by "C") are required. The nominal path of the tactile probe forms a straight line, tangent to the base circle and synchronized with the angular motion of the rotary axis. Therefore, deviations in the surface normal direction of an involute profile are detected by one dimensional (1D) displacements (magnitude and sign) of the tactile sensor. This movement is known as "Tangential scanning" or "rolling method". Similarly, a linear motion with another two axes is used for measuring the helical deviation of a gear flank, as shown in Figure 1.4 (b), where the translational motion is in vertical direction (denoted by "Z"). These two mechanical motions serve as the fundamental principle of conventional gear inspection by tactile sensor. They were applied even before the emergence of CNC technology [2].

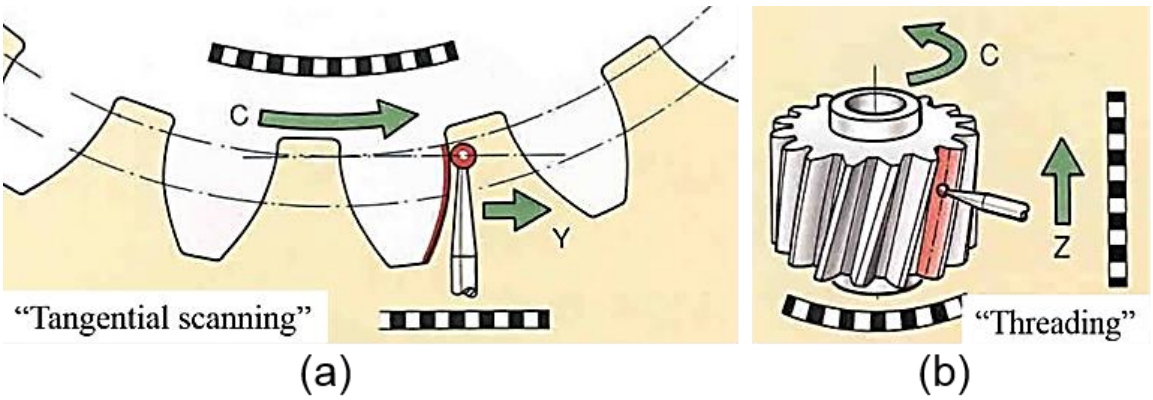

Figure 1.4: Basic kinematic pricniples for conventional gear measurement, (a) profile measurement in transverse plane; (b), al helix/lead measurement (source: Mahr).

Numerous parameters were developed to assess deviation characteristics in conventional measurement. Figure 1.5 and Figure 1.6 show the graphical representations

of geometric features and the associated deviation parameters for a measured profile and a helix respectively. In Figure 1.5, L_α is the profile evaluation length, and g_α is the length of path of contact. In Figure 1.6, the Roman numerals I and II indicate the datum and non-datum faces of a gear, respectively. The helix evaluation length and face width are denoted by L_β and b, respectively. These evaluations are referred to as "line oriented evaluation", since an ideal profile or helix should be represented by a constant zero line in those evaluation charts.

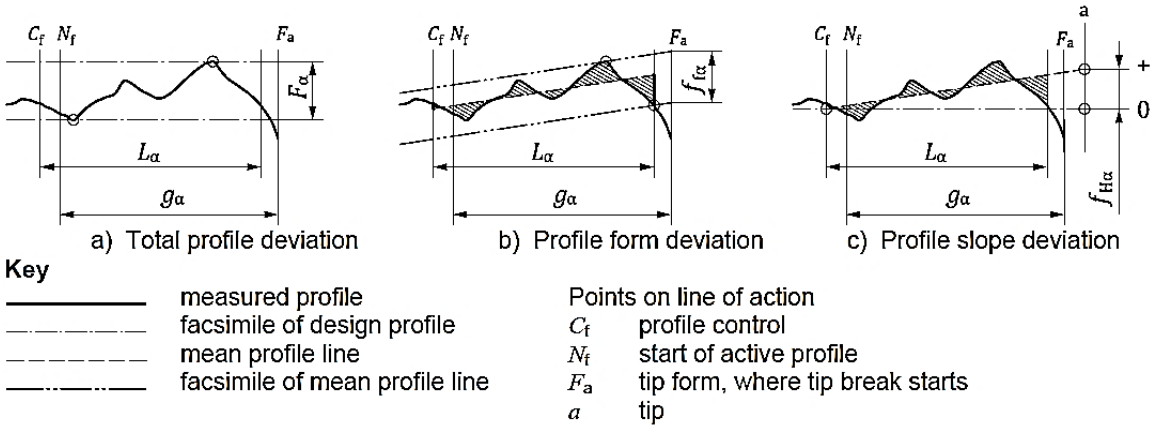

Figure 1.5: Evaluation of profile deviation with unmodified involute [18].

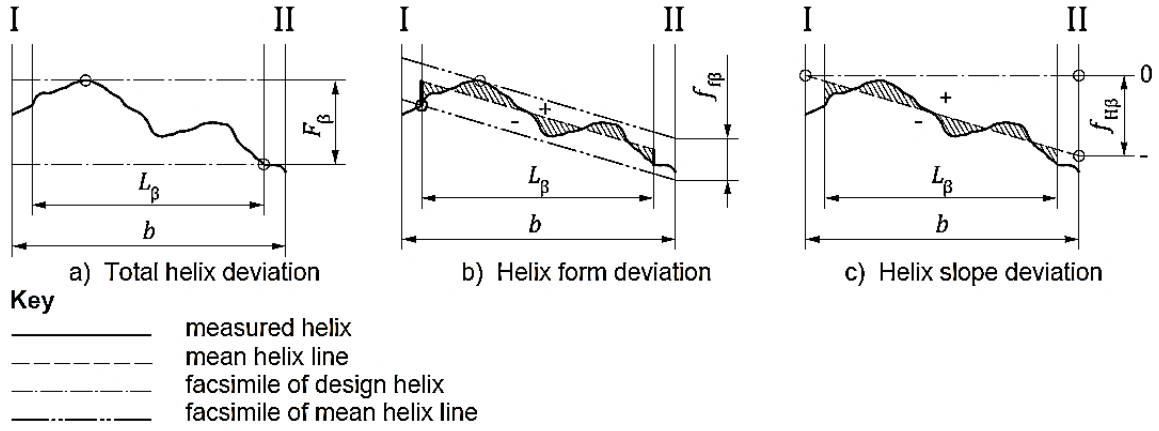

Figure 1.6: Evaluation of helix deviation with unmodified helix [18].

1.2.2 Measurement and evaluation of tooth-to-tooth deviations

One tooth is arbitrarily selected as the reference tooth (e.g. tooth #1) with a defined counting direction (clock wise or counter clock wise) due to the rotational symmetry of the gear. The relative position of a certain tooth (either right or left flank) with respect to other teeth (corresponding right or left flank) is characterized by the pitch deviation [18]. Figure 1.7 shows three typical mechanical methods of measuring the pitch deviations by tactile instruments, depending on the mechanical configuration of the measuring device and the probing stylus [19]. The arrows show the motion engaged during a probing procedure of the pitch points on certain flanks.

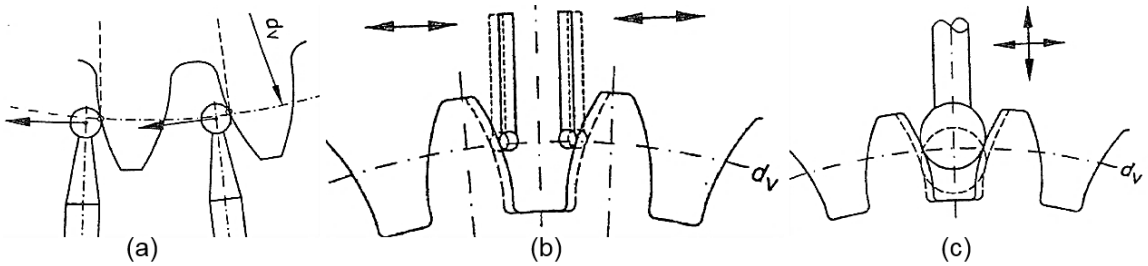

Figure 1.7: Pitch measurement by tactile sensors: (a), direct measurement of single pitch by relative linear measurment; (b), pitch measurement with single flank contact; (c), pitch measurement with two flank contact [20].

Specific pitch deviations such as single pitch deviation (f_{pi}) and cumulative pitch deviation (F_{pi}) are evaluated by a set of points probed on each left and right flanks. Thus, a diameter on the gear body must be specified as the measurement diameter (denoted by d_{M}) to guide the data collection by a tactile probe, as shown in Figure 1.8.

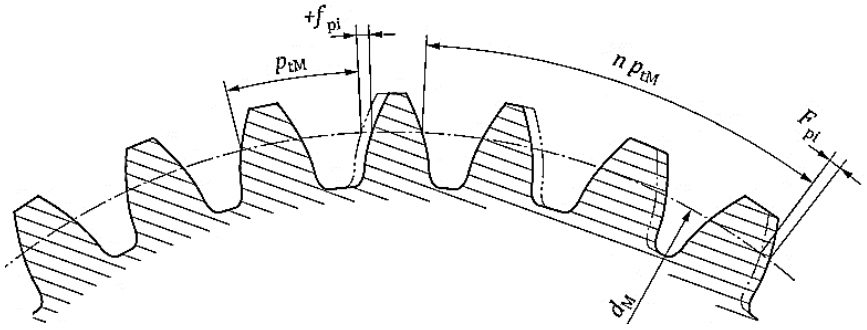

Figure 1.8: Individual single pitch deviation and cumulative pitch deviations [18].

Clearly, the measured feature for evaluating the pitch deviation is a point (1D) on a 2D plane (typically a transverse plane in the middle of the facewidth) for a 3D gear tooth. This requires a different motion control method for the measurement strategy and a unique evaluation strategy, making the pitch measurement an independent measurement task, compared to the profile and helix measurements. Recently, new measurement systems based on tactile technology including double flank rack probe [21], surface profiling sensor [22] and articulated arm CMM [23] have been developed in academia and national metrology institutes (NMIs), offering new opportunity for more robust and user-friendly solutions in the gear industry.

Figure 1.9 (a) shows a CMM based gear measurement without using a rotary table. Instead a tactile sensor composed of eight styli is configured to measure all teeth of the gear sample as well as the pitch and runout deviations. The scanning motions are realized directly by the three linear axes of the CMM. Figure 1.9 (b) shows how a combination of one single stylus and one rotary table is utilized to measure both the flank deviations and the pitch deviations of the gear sample by a CMM. Figure 1.9 (c) shows a Gear Measuring Instrument (GMI) with similar mechanical configuration as the CMM with rotary table.

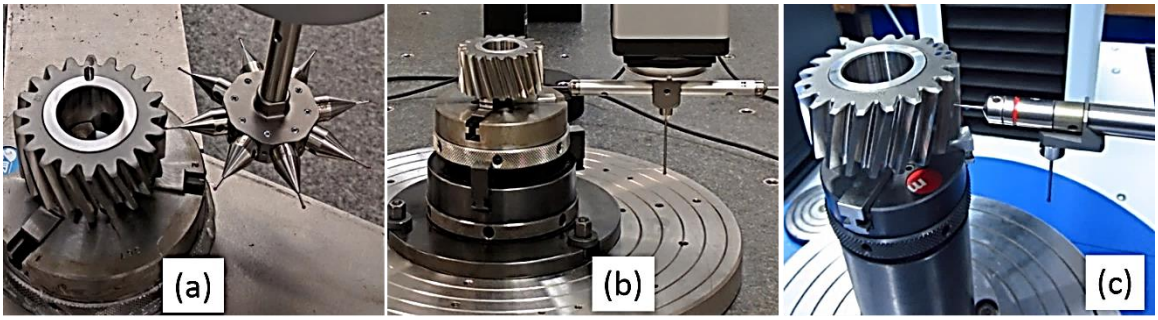

Figure 1.9: Three typical measurement configuration of industrial gear measurement: (a), CMM without rotary table (Leitz PMMF302016); (b), CMM with rotary table (Zeiss Prismo); (c), GMI with rotary table (Klingelnberg P26).

1.3 Traceability, gear artifact and calibration of gear measuring instruments

To calibrate a gear measuring device, physical standards (i.e. artifacts) are needed to realize the unit (meter) of the measurand for specific geometric features of a gear [2]. Figure 1.10 illustrates the traceability chain of gear measurement from a NMI to a produced gear. It is kept unbroken via certified gear artifacts and calibrated instruments. The choice of artifact for a specific measurement task is based on the similarity principle: the geometry of the artifacts should be similar to the geometrical and mechanical properties of the product gear in terms of size, number of teeth, material, weight etc. [24].

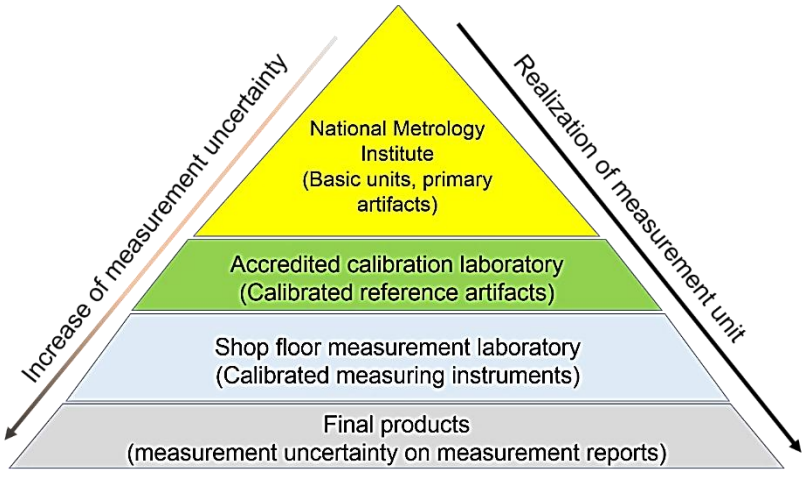

Figure 1.10: Hierarchy chain for maintaing traceability of artifacts based gear metrology.

Figure 1.11 (a) to (c) show the profile, helix and pitch artifact used in the intercomparison of gear measurement among major NMIs [25]. If the size of a gear sample is significantly larger or smaller than an available artifact, the artifact must be replaced due to the similarity principle. For example, the gear segment artifact shown in Figure 1.11 (d) is developed to calibrate measuring instruments used for the inspection of wind energy gears with a diameter of larger than 1 meter [17].

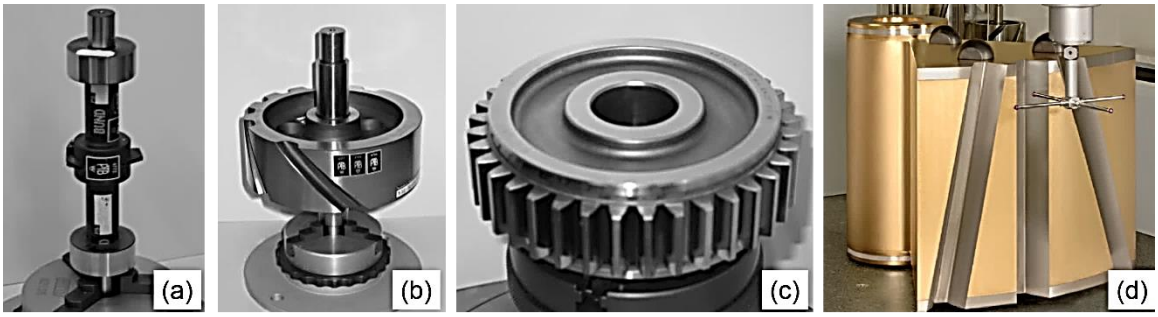

Figure 1.11: Feature oriented gear artifacts: (a), involute artifact; (b), helix artifact; (c), pitch artifact; (d), gear segement artifact.

The trend of using gear-like artifacts and simple geometry artifacts to calibrate gear measurement system have gained awareness in both academia and industry since the 1990s. This concept was first realized by Pfeifer [26], who used cylinders with gridded coordinates as a nominal bevel gear flank geometry to calibrate a bevel gear measurement instrument with quantifiable metrological characteristics. Komori et al. used a wedge artifact and a ball plate to represent helix and pitch, respectively, for calibrating tactile instruments [27] [28] [29], as shown in Figure 1.12 (a) and (b). Moreover, Guenther et al. applied a ball plate to represent the geometry of bevel gear flanks [30], as shown in Figure 1.12 (c). Lanza et al. developed a cylindrical standard for involute profile and pitch calibration of micro gears [31], as shown in Figure 1.12 (d).

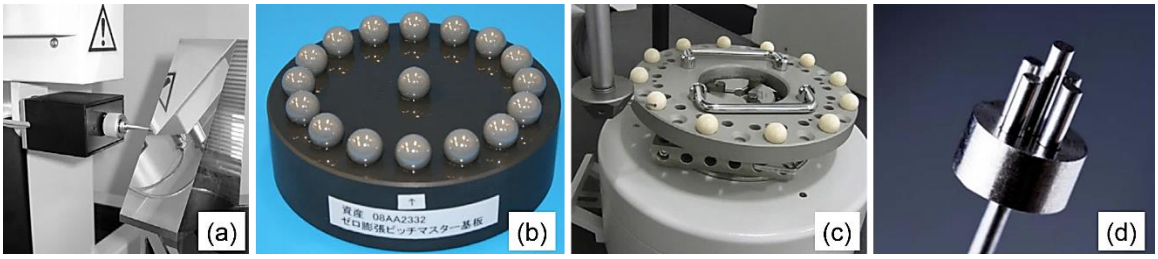

Figure 1.12: Geometry oriented artifacts: (a), wedge artifact for helix calibration [27] ; (b), ball plate artifact for pitch calibration [29]; (c), ball plate for bevel gear flank measurement [30]; (d), cylinder artifact for involute measurement [31].

However, none of those developed artifacts have been applied in area oriented gear measurement, let alone areal evaluation of areal measurement data. Thus, new artifacts should be developed to close the gap for measuring principles other than tactile probing, namely optical [32] and computed tomography based systems [33].

1.4 Areal measurement of gear flanks

1.4.1 Mechanical methods

A mechanical flank measurement system developed by FRENCO [34] is able to capture an areal map of a helical gear sample through the measurement of a flank at multiple sets of transverse planes. As shown in the left side of Figure 1.13 (a), the roll master is equipped with several “insert teeth” distributed along the axial direction such that the gear sample (right side) can be measured at various transverse planes driven by the rotational motion. The corresponding evaluation method is called “Reality Analysis” (REANY in short), aiming to visualize all the measured teeth with topography data (see Figure 1.13 (b)). However, limited areal parameters (except total deviation) are given by the evaluation software, even the areal topographical information of all flanks is available.

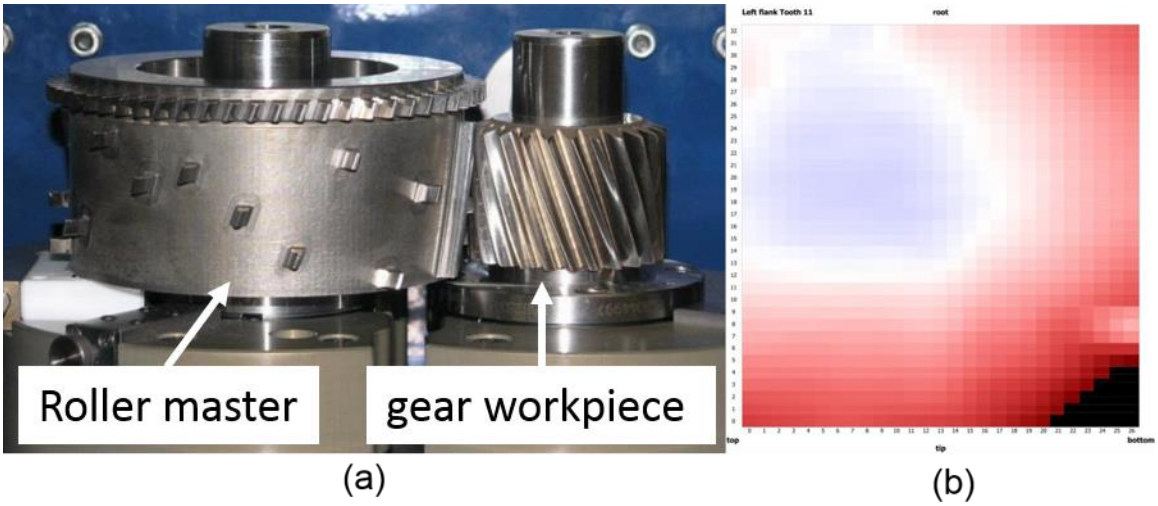

Figure 1.13: Areal flank measurement and evaluation by mechanical rolling test [34]: (a), measurement setup; (b), a measured areal flank map.

1.4.2 Optical methods

Compared to tactile based measurement methods, optical measuring systems offer non-contact, fast and high-density data acquisition capability for production metrology [35]. To measure the geometry of gear flanks, several instrumentation efforts have been developed aiming at collecting surface data on gear flanks. Takeoka et al. developed a laser interferometer system (beam spot diameter 6 μm) to measure the profile form deviation of an involute artifact [36].

To measure a complete flank surface of gear, Lu et al. proposed the optical measurement of gear flanks based on the principle of phase shift optical triangulation. A surface topography at micrometer level resolution was obtained by a phase unwrapping algorithm. However, the system did not provide any characteristic parameters used in gear industry [37]. Peters et al. developed a fringe projection system to measure the entire flank (several square centimeter) of a helical gear [38].

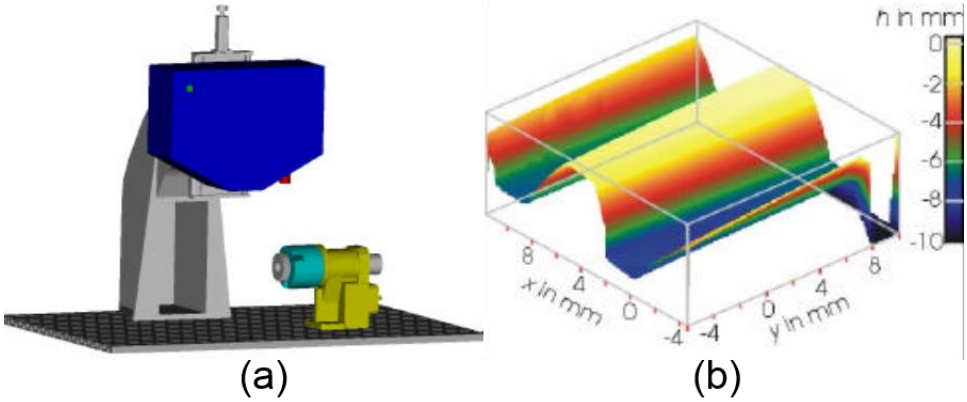

Figure 1.14. Optical gear flank measurement system: (a), configuration of the fringe projection system and gear sample; (b), a tooth with areal flank measurement (after [38]).

S. Fang et al. developed a laser interferometric system to measure the flank surface of a spur gear and a helical gear [39], as shown in Figure 1.15. The oblique-incidence based method has evolved from measuring spur gears to helical gear flanks by using improved instrumentation [40] [41].

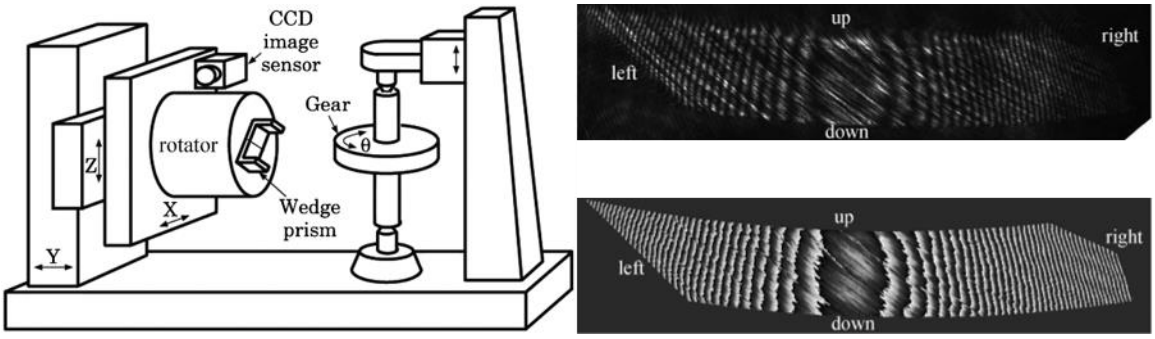

Figure 1.15: Instrument configuration of gear measurement systrem and image of measured flank by laser interferometry (after [39]).

However, no gear deviation parameters were reported in the mentioned optical techniques. Instead, with the improved performance of laser triangulation technology, several commercial instruments have been developed with different opto-mechanical

configurations since 2015. For example, instruments developed by MS3D [42], Nikon [43] and Gleason [44] offer the capability to capture data on the entire flank surface of all teeth.

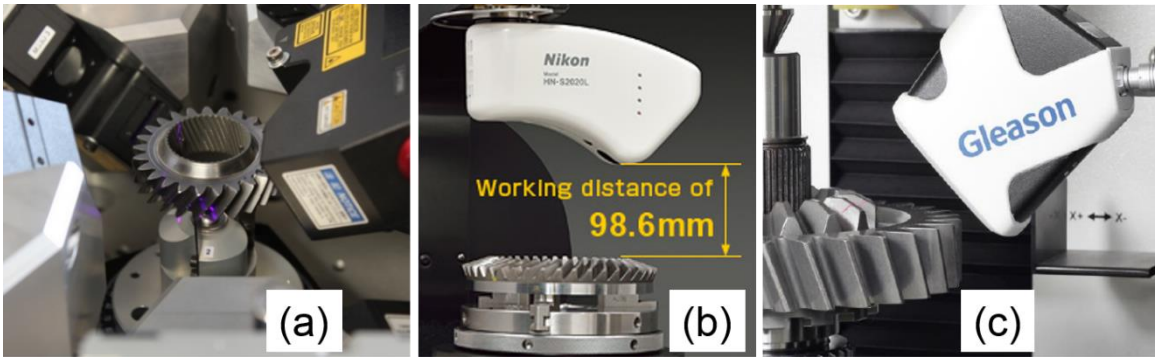

Figure 1.16: Commercial non-contact gear measuring instruments: (a) MS3D [42]; (b) Nikon HN-C3030 [43]; (c) Gleason 300GMSL [44].

For example, Figure 1.17 shows the measurement setup and captured point clouds of a helical gear, realized with a Nikon HN-C3030 instrument.

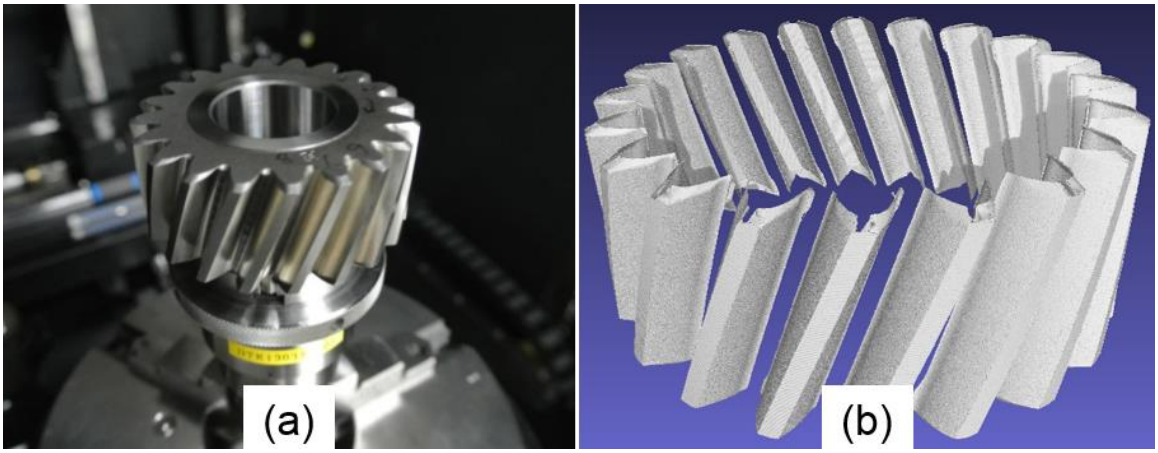

Figure 1.17: Measurement of a gear sample by Nikon HN-C3030: (a), measurement setup; (b), measured point clouds of the gear sample, covering both flanks of all teeth.

However, line oriented evaluation parameters are still used for those instruments, even with hundreds of thousands of spatial points that are captured across an entire gear.

There is an urgent need to provide areal gear parameters for optical gear instrument manufactures to fully exploit the advantages of optical gear measuring systems.

Moreover, the standard measurement strategy has a severe limitation, when applied to characterize the geometric information of large gears e.g. in wind energy system, compared to their counterparts in the automobile industry, if only several line oriented features are measured and evaluated. Firstly, because of the longer time used for machining a large gear, environmental conditions such as room temperature and vibration, machine tool thermal load and tool wear are most likely to leave different geometric deviations on different locations of a flank. Secondly, distortion caused by residual stress can be released during heat treatment, leading to local deformation of flanks of the whole gear [45], which might not be noticeable on three or four teeth of the gear. Lastly, deformation caused by gravitational load at different mounting conditions for the measuring object can also influence quantitatively the inspection results, carried out by standard measurement [46].

Areal measurement of gear flanks is more suitable to offer point cloud data that cover the entire flank and all teeth of a gear. Those type of data offer the possibility to extract areal characteristics from the point cloud representing the shape, form and location information of a flank and a whole gear. It is necessary to develop corresponding evaluation methods and areal gear parameters to assess the geometric information of the measured gear, taking advantage of high density point clouds.

1.5 Contributions of this dissertation

Because of the mentioned limitations and deficiencies of conventional gear inspection methods, a paradigm shift of gear metrology is necessary concerning both the applied measuring strategies and the evaluation procedures. This shift can enable a holistic

gear evaluation for improving gear manufacturing processes and predicting gear performances, based on the area oriented metrology of a complete gear. This dissertation investigates and implements a novel computational method based on a 3D geometric model of a complete gear, aiming at a paradigm shift towards areal cylindrical gear metrology. This method is concerning with the following aspects:

- a 3D geometric model for cylindrical gears with flank modifications, including an implicit analytical equation describing the nominal cylindrical gear (individual flank and complete gear), based on the plumb line distance [16];
- a newly proposed set of areal evaluation parameters, aiming at the extension of current line oriented gear parameters to characterize the 3D geometry of entire gear flanks; and
- an orthogonal decomposition method for calculating the proposed areal gear deviation and modification parameters, based on 2D Chebyshev polynomials and their numerical implementation.

The proposed 2D Chebyshev method is explained in detail in Chapter 4 and verified by simulated gear data throughout this dissertation. Experimental validation by the measurement of a calibrated precision gear artifact show the effectiveness of this novel method, which demonstrates the applicability for industrial gear inspections.

1.6 Dissertation layout

Chapter 1 has introduced the background, motivation and significance of this work. The state-of-the-art in gear metrology technologies are reviewed from the perspectives of both measurement and evaluation. As complex flank modifications become prevalent on gears, line oriented measurement and evaluation methods lead to potential ambiguity, and

even deficiencies in characterizing the geometry of a gear flank. Thus, areal gear measurements applying optical measuring principles have shown an increasing importance as an alternative for future gear inspection. But the lack of an evaluation method, namely the missing capability to extract areal flank information from areal spatial point clouds, imposes a severe technical gap for further adaption of optical areal measurement systems in industry.

Chapter 2 describes the 3D modeling of a helical gear flank based on fundamental gear design parameters. To evaluate the measured 3D gear data, Euclidean distance, projected distance and plumb line distance are introduced and compared in terms of mathematical definitions and metrological meanings. Afterwards, a new interpretation of the zero-valued, plumb line distance is presented, which can provide an implicit equation describing the nominal involute gear geometry. This equation defines the "pure involute" surface that is referred to in this dissertation. Several simulated data sets are used to verify the interpretation at the end of this chapter. Nominal information of an individual flank, an individual tooth and all teeth of a gear is included in the implicit equation. This equation forms the foundation for the development of a new evaluation strategy for a complete gear, including individual tooth and tooth to tooth deviations.

Chapter 3 focuses on the approximation of discrete datasets by Chebyshev series. Main mathematical properties of the Chebyshev polynomials are reviewed with engineering interpretations for gear metrology. Simulations by using 2D Chebyshev series to approximate the coefficients of a power series describing a surface have shown the advantages of orthogonal decomposition in a square domain of $[-1,1]^2$. This method is

referred to as the 2D Chebyshev method for approximating the areal gear parameters in the following chapters.

Chapter 4 studies the relationship between low order flank geometries and the first six terms of 2D Chebyshev polynomials. They are analyzed in terms of geometric similarity and analytic connection. A new set of areal parameters is proposed as an extension of their counterparts in standardized line oriented parameters. Lastly, a procedure is presented showing the steps to obtain those areal gear parameters by the 2D Chebyshev polynomials, defined in a square domain of $[-1,1]^2$.

Chapter 5 introduces at the beginning three computational methods for calculating 2D Chebyshev coefficients. Three types of nominal point distributions on helical gear flanks are tested by the three methods. Afterwards, numerical influences such as data density and non-orthogonality are studied in terms of computational performances based on simulations. Misalignment of the workpiece coordinate system of a gear with respect to its nominal are simulated. The correlation between the change of areal gear parameters to the simulated misalignment are observed.

Chapter 6 gives the experimental verification of using the 2D Chebyshev method to obtain areal gear modification parameters on a calibrated gear modification artifact. Four flank modifications and two pitch modifications have been successfully determined with an agreement of no more than 2 μm between the calibrated line oriented parameters and the areal parameters.

Chapter 7 presents the conclusion of this dissertation and suggests several future works.

CHAPTER 2 : COMPLETE 3D MODLES OF CYLINDRICAL GEARS

In this chapter, the basic mathematics of a 2D involute geometry is introduced, before the development of a 3D helicoid surface for a cylindrical gear flank. Based on the nominal gear design parameters such as number of teeth (z), base radius (r_b), pressure angle (α_t) and helix angle (β), a complete 3D nominal geometry of a cylindrical gear is established. Afterwards, based on the model in [16], a refined mathematical expression for typical low order flank modifications (i.e. profile slope, helix slope, profile crowning, helix crowning and flank twist) is presented, aiming to replace the original equation by the simplicity of mathematical treatment shown in later chapters.

Three types of distances between a nominal and a measured point are presented as the common practice for calculating the deviations of measured points for the nominal geometric features of the measured object (i.e. gear flank surface). Those distances are namely the Euclidean distance, the projected distance and the plumb line distance, which are commonly used in gear metrology and several areas of geometry measurements. An implicit equation that represents the “shape” or “form” of a nominal gear flank is obtained by rearranging the variables in the plumb line distance formula. Further interpretation and applications of this implicit equation characterizing a helical gear flank will be discussed in detail at the end of this chapter.

2.1 Mathematical description of pure involute geometry

2.1.1 2D involute curve as a gear profile

The definition of an involute traces back to 1673, given by Christiaan Huygens in his analysis of the motion of a pendulum. An involute is a curve generated on geometries

such as circles and ellipse. The involute curve generated on a circle is most widely used for gear profiles because of a unique property. It has been proven that an involute curve keeps a constant ratio of angular speeds between two meshing gears with two different pitch diameters.

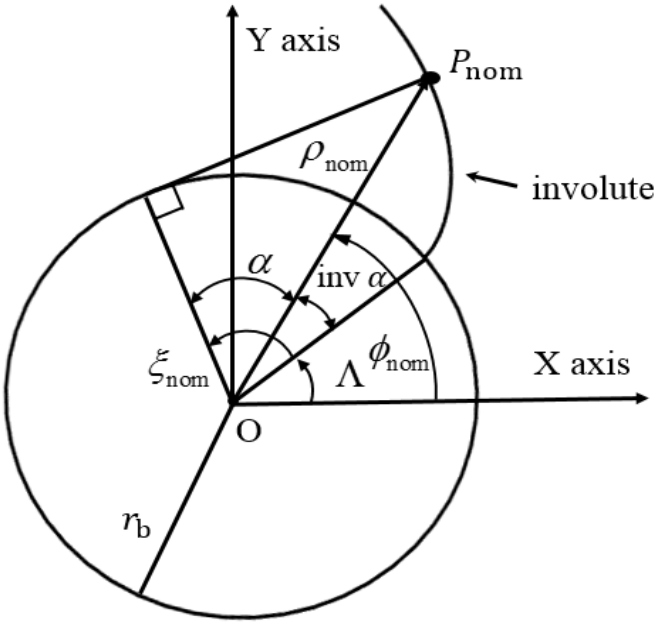

Figure 2.1: Basic geometry of a 2D involute curve.

In a 2D Cartesian coordinate system, the coordinates of a nominal point $P_{nom} = (x_{nom}, y_{nom})$ on the involute curve, starting from the base circle with the radius r_b, is given by:

$$\begin{cases} x_{nom} = r_b[\cos(\xi_{nom} + \Lambda) + \xi_{nom} \sin(\xi_{nom} + \Lambda)] \\ y_{nom} = r_b[\sin(\xi_{nom} + \Lambda) - \xi_{nom} \cos(\xi_{nom} + \Lambda)] \end{cases}, \tag{2.1}$$

in which Λ denotes the angular position of the starting point of the involute curve at the base circle and ξ_{nom} is the rolling angle assigned to P_{nom} shown in Figure 2.1.

The limit of the roll angle (i.e. ξ_{st} and ξ_{end}) are denoted by the subscripts "st" and "end" for the start and end, respectively. They determine the length of the involute curve, while the base radius r_b determines the shape of the involute curve. Equation (2.1) can be interpreted as the parametrized form of a 2D involute curve in Cartesian coordinates with ξ_{nom} as independent variable. Obviously, the base radius defines the general shape of the involute curve. It therefore determines the shape of the gear tooth.

In a cylindrical coordinate system, the position of the nominal point P_{nom} is:

$$\begin{cases} \rho_{nom} = \sqrt{x_{nom}^2 + y_{nom}^2} = r_b\sqrt{1+\xi_{nom}^2} \\ \phi_{nom} = \arctan\left(\dfrac{y_{nom}}{x_{nom}}\right) \end{cases} . \tag{2.2}$$

Figure 2.2 shows a segment of a gear with teeth that are numbered in the clockwise direction. The size of a tooth is determined by the root form radius and tip form radius, denoted by r_{Ff} and r_{Fa}, respectively.

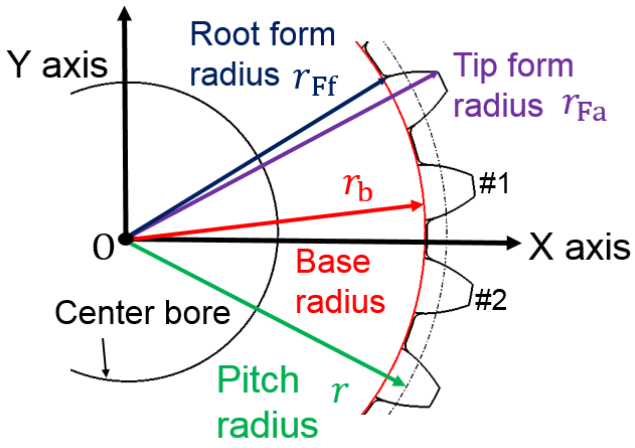

Figure 2.2: Basic geometric parameters of a nominal spur gear (viewed in transverse plane).

2.1.2 3D helical surface as gear flank

Based on the 2D involute curve in the transverse plane, the 3D geometry of a helical surface (see Figure 2.3) can be generated by a "threading" model in [10] [16] as an areal mathematical description of a helical gear flank. In this model, the origin (yellow dot) of each involute profile in a transverse plane is "threaded" along the base helix line (illustrated by the tilted black line with the base helix angle β_b) from the bottom to the top covering the entire gear facewidth. Therefore, the coordinate of a nominal point on the pure involute surface is mathematically realized by describing the nominal initial angle $\Lambda(z_{nom})$ of the 2D involute profile on each stacked transverse plane as a function of the third dimension:

$$\begin{cases} x_{nom} = r_b[\cos(\xi_{nom} + \Lambda(z_{nom}) + \xi_{nom}\sin(\xi_{nom} + \Lambda(z_{nom})] \\ y_{nom} = r_b[\sin(\xi_{nom} + \Lambda(z_{nom}) - \xi_{nom}\cos(\xi_{nom} + \Lambda(z_{nom})] \\ z_{nom} = z_{nom} \end{cases}, \tag{2.3}$$

where, the explicit expression of $\Lambda(z_{nom})$ is:

$$\Lambda(z_{nom}) = \eta_b + z_{nom}\frac{\tan\beta_b}{r_b}. \tag{2.4}$$

The size of a helical gear is determined by both the diameter range of the involute curve and its height in the Z direction:

$$\begin{cases} \xi_{st} \le \xi_{nom} \le \xi_{end} \\ 0 \le z_{nom} \le b \end{cases}, \tag{2.5}$$

where b is the gear's facewidth. Equation (2.3) can be interpreted as the parametrized form of a helical surface in a Cartesian coordinate system with ξ_{nom} and z_{nom} as parameters, whose values are constrained to Equation (2.5).

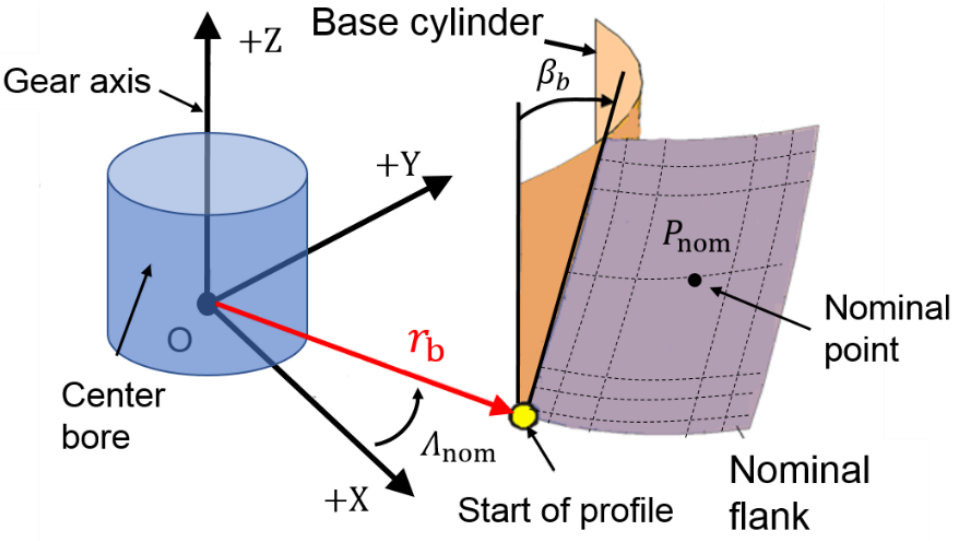

Figure 2.3: A right flank of a helical gear in 3D space, edited after [10].

For an individual tooth, the location of each involute is determined by the value of the base space width half angle η_b, which is defined in ISO 21771:

$$\eta_b = \frac{\pi - 4 \cdot x \cdot \tan \alpha_n}{2|z|} - \text{inv}\,\alpha_t, \tag{2.6}$$

where x is the profile shift coefficient, α_n is the normal pressure angle, $|z|$ is the absolute value of the number of teeth and $\text{inv}\alpha_t$ is the involute angle. In addition, throughout this dissertation, two assumptions are made: first, no profile shift is introduced (i.e. $x = 0$); second, all gears are external gears (i.e. $z > 0$, $|z| = z$). The base space half angle η_b is shown in Figure 2.4.

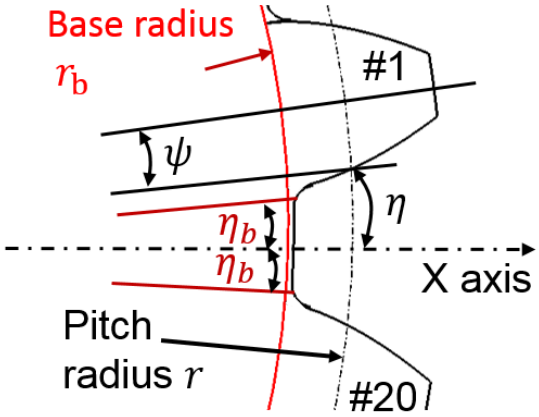

Figure 2.4: Definition of base space width half angle η_b on base circle, tooth thickness half angle ψ on pitch circle and space half angle η on pitch circle.

A set of nominal gear parameters are listed in Table 2.1 for simulating the nominal geometry of a gear in this dissertation. Figure 2.5 shows the complete gear with both right and left flanks, generated by the parameters in Table 2.1. Ten profile lines and five helix lines are highlighted in blue while the nominal gear flank is imaged in yellow.

Table 2.1 Nominal gear parameters for generating gear flanks in Figure 2.5.

Name	Symbol	Value	Unit
Number of teeth	z	20	Dimensionless
Normal module	m_n	3	mm
Normal pressure angle	α_n	20	degree
Facewidth	b	30	mm
Helix angle	β	20	degree
Helical direction	Right hand	1	Dimensionless

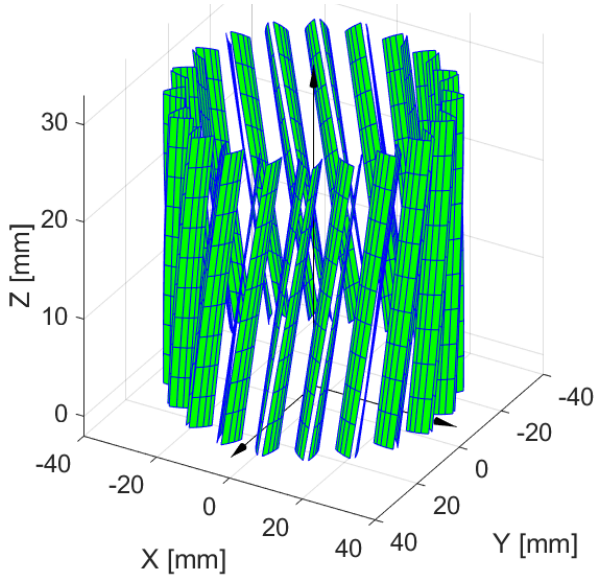

Figure 2.5: Generated teeth of a gear in 3D using parameters in Table 2.1.

The use of "pure involute" (or "pure helicoid" for helical gears) throughout this dissertation is to differentiate the intended modifications from the undesired deviations. Because both modification and deviation on a gear flank lead to a non-zero value calculated by the plumb line distance equation (see Section 2.3.3), it is mathematically impossible to distinguish them simply by the values in an areal distance map without a prior knowledge of basic gear parameters and the nominal amounts for modifications (see Section 2.2).

2.1.3 Surface normal vector and *u*-*v*-*d* system

Equations (2.3) to (2.5) represent the nominal surface of a helical gear in 3D space. However, flank modifications were not taken into consideration. According to ISO [18], a flank modification is an intended geometry alteration with respect to the pure involute surface, and it is usually defined as a function of a characteristic length in profile and/or helix direction. For example, in Figure 2.6, the conventional profile slope modification

$C_{H\alpha}$ is defined by the distance between the tip point of the intended profile and the tip point of the pure involute at a tooth.

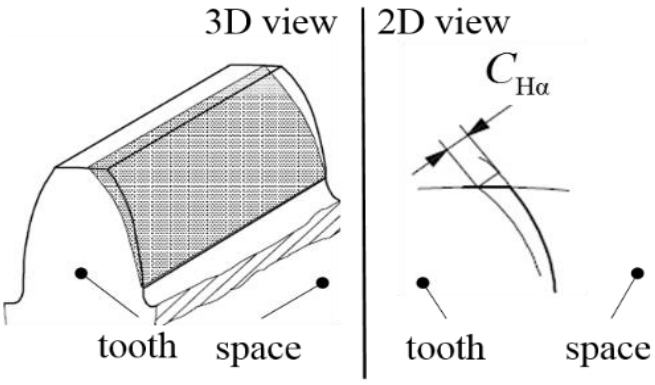

Figure 2.6: Definition of profile slope modification $C_{H\alpha}$ [15].

To extend the analytic description of the modifications on the flank of a helical gear from a 2D line oriented function to a 3D surface function, a pair of coordinates (u,v) is introduced. Moreover, a parametric representation of the modified flank can be established for an areal analysis, which will be discussed in Section 2.2. In Figure 2.7, the nominal point P_{nom} can be described by the surface coordinates u and v:

$$\begin{cases} u = r_b \xi_{nom} \\ v = z_{nom} \end{cases}. \tag{2.7}$$

This choice of this surface parametrization is suitable for two reasons: first, the u axis follows the mathematical foundation of the generation principle describing an involute curve; second, the combination of u and v axes accommodates the typical primary motion control system for generation cutting and conventional gear inspection.

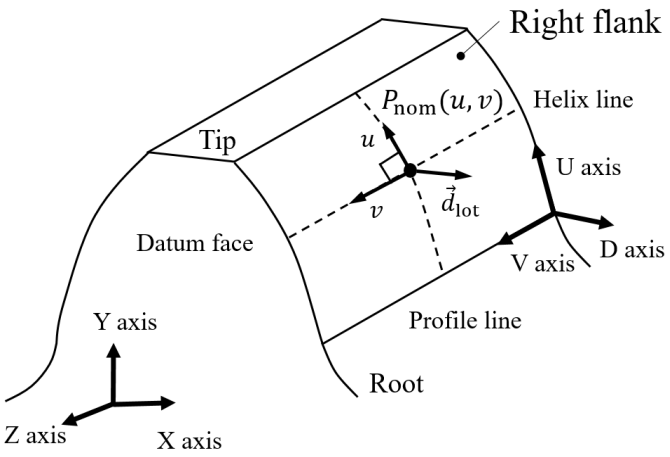

Figure 2.7: Illustration of curved coordinates (u,v) for the pure involute and surface normal vector of a spur gear's right flank.

In fact, from a mathematical point of view, the coordinates (e.g. *x*, *y* and *z*) of a nominal point can be given by continuous, bivariate, single-valued functions of the form: $x = x(u,v)$, $y = y(u,v)$ and $z = z(u,v)$. This formation based on *u* and *v* is thus referred to as a parametrization of a surface [47].

The analytic expression of the surface normal vector $\vec{N}$ on a helical flank surface is obtained by the cross product of two tangential vectors along U and V directions at any nominal point P_{nom} based on the Equation (2.3) and Equation (2.7):

$$\vec{N} = \begin{pmatrix} N_{\mathrm{x}} \\ N_{\mathrm{y}} \\ N_{\mathrm{z}} \end{pmatrix} = \frac{\partial \overrightarrow{P_{\mathrm{nom}}}}{\partial u} \times \frac{\partial \overrightarrow{P_{\mathrm{nom}}}}{\partial v} = \xi_{\mathrm{nom}} \begin{pmatrix} \sin(\xi_{\mathrm{nom}} + \Lambda_{\mathrm{nom}}) \\ -\cos(\xi_{\mathrm{nom}} + \Lambda_{\mathrm{nom}}) \\ \tan\beta_{\mathrm{b}} \end{pmatrix}, \tag{2.8}$$

where N_{x}, N_{y} and N_{z} are the x, y and z components of the vector $\vec{N}$ in the X, Y and Z directions, respectively. For a spur gear (i.e. β_{b} = 0), the surface normal vector has a constant zero N_{z} component at any point on the flank since the spur gear can be simply

treated as a vertical "stacking" of 2D involute curve in the Z direction. A detailed derivation of the surface normal vector can be found in APPENDIX A.

Dividing the vector $\vec{N}$ by its length gives the unit vector $\vec{n}$ in Cartesian coordinate system:

$$\vec{n} = \begin{pmatrix} n_x \\ n_y \\ n_z \end{pmatrix} = \frac{\vec{N}}{|\vec{N}|} = \frac{1}{\sqrt{1+\tan^2 \beta_b}} \begin{pmatrix} \sin(\xi_{nom} + \Lambda_{nom}) \\ -\cos(\xi_{nom} + \Lambda_{nom}) \\ \tan \beta_b \end{pmatrix}, \tag{2.9}$$

where n_x, n_y and n_z are the x, y and z components of the vector $\vec{n}$ in the X, Y and Z direction, respectively. Obviously, the z component of the unit vector only depends on the value of the helix angle, while the x and y components are determined by the angular location of a certain profile (i.e. Λ_{nom}) and the location of a certain nominal point on that profile (i.e. ξ_{nom}). The derivations of the analytic expression of the surface normal vector and its unit vector can also be found in APPENDIX A.

2.2 Analytic formation of flank modifications of cylindrical gears

Gear modifications can be given as functions of either the diameter (i.e. d_y), the roll angle ξ_y or the length of roll $L_y = r_b \xi_{nom}$, in which the subscript "y" indicates an arbitrary value of the variable. In [16], the length of an involute curve is used rather than the length of roll to describe the modification function in profile direction, which leads to a different analytic expression and geometrical meaning of the *u* parameter. Instead, in this dissertation the value of the length of roll is the independent variable, and the amount of a specific modification is the dependent variable.

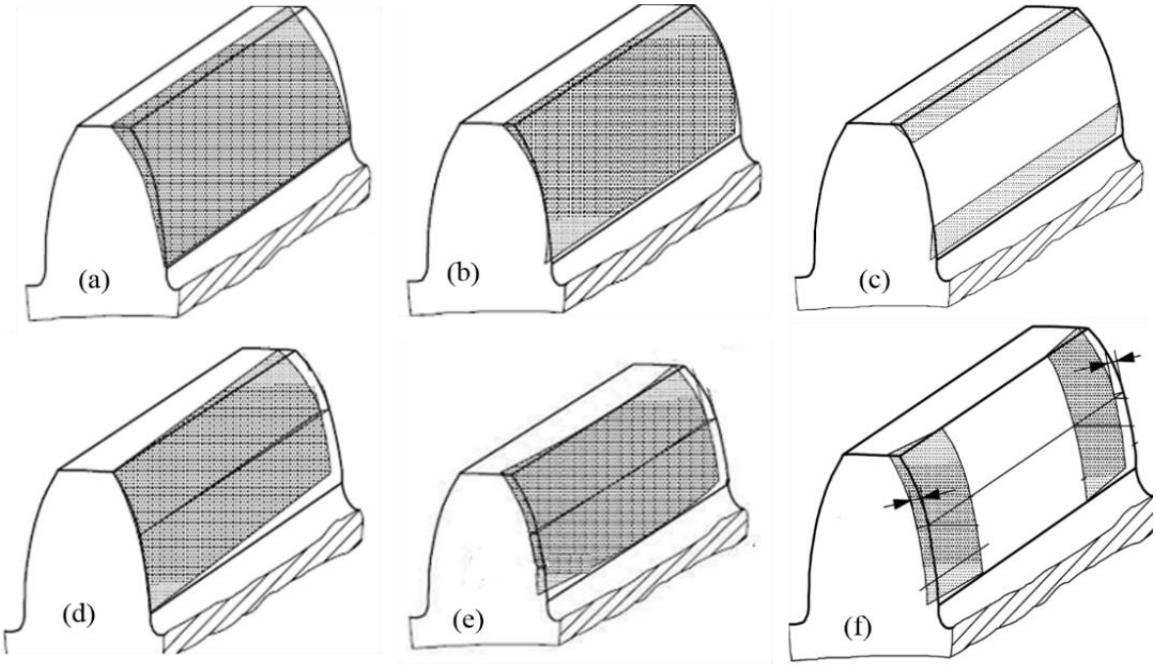

Figure 2.8: Typical flank modifications for cylindrical gears in 3D space [15]: (a) profile slope modification, (b) profile crowning modification, (c) tip and root relief, (d) helix slope modifications, (e) helix crowning modification, (f) end relief at top and bottom face.

Figure 2.8 shows six typical flank modifications for cylindrical gears in 3D space. Figure 2.9 and Figure 2.10 depict the definitions of four flank modifications as a function of *u* and *v* in the profile and helix directions respectively.

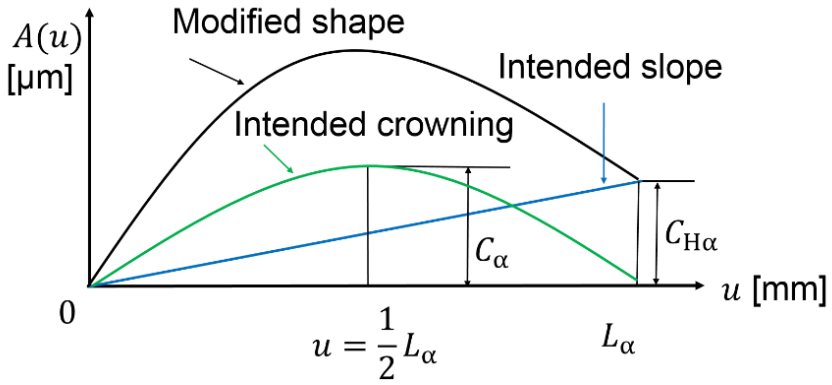

Figure 2.9: Slope and crowning modifications designed in profile direction.

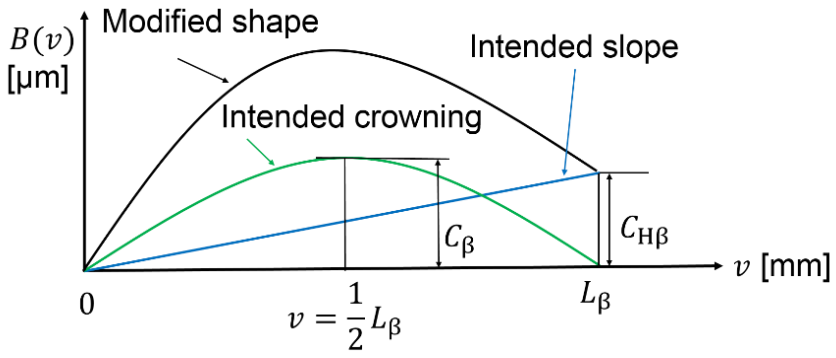

Figure 2.10: Slope and crowning modifications designed in helix directions.

The unit of flank modification is the micrometer, the amount of which can vary from a few micrometers to several ten micrometers. According to [16], the analytic expression for slope and crowning modifications in the profile direction is:

$$A(u) = -\frac{4C_\alpha}{L_\alpha^2}u^2 + \frac{4C_\alpha + C_{H\alpha}}{L_\alpha}u, \tag{2.10}$$

where C_α denotes the amount of profile crowning and $C_{H\alpha}$ the amount of profile slope; and the analytic expression for slope and crowning modifications in the helix direction is:

$$B(v) = -\frac{4C_\beta}{L_\beta^2}v^2 + \frac{4C_\beta + C_{H\beta}}{L_\beta}v, \tag{2.11}$$

where C_β denotes the amount of helix crowning modification and $C_{H\beta}$ the amount of helix slope modification.

$A(u)$ and $B(v)$ are referred to as the modification functions. The sign conventions of modifications for left and right flanks of left-handed or right-handed gears are determined according to standards such as [15].

The coordinates of point P_{mod} on a modified gear flank (x_{mod}, y_{mod}, z_{mod}) can be generated by adding the modification functions vectorially in the surface normal direction to the coordinates of a nominal point, as:

$$\begin{cases} x_{\text{mod}} = x_{\text{nom}} + \left[A(u) + B(v)\right] \cdot n_{\text{x}} \\ y_{\text{mod}} = y_{\text{nom}} + \left[A(u) + B(v)\right] \cdot n_{\text{y}} \\ z_{\text{mod}} = z_{\text{nom}} + \left[A(u) + B(v)\right] \cdot n_{\text{z}} \end{cases} . \tag{2.12}$$

2.3 Distances for characterizing spatial deviations of gear flanks

To assess the "closeness" of a workpiece with respect to its design intent in terms of size, form, orientation and position of features, a quantity must be assigned accordingly. This assessment usually involves calculating the distance from a measured point P_{m} to a nominal geometry, represented by various mathematical formations [48] [49]. Various distances are used in production metrology for evaluating geometric deviations (size, form and surface topography) as well the orientation and position of a measured feature with respect to other entities. The distances discussed in this section are obtained under the assumption that at least a fine alignment (numerical alignment) of the workpiece has been established. Therefore, the deviation manifested by the calculated quantity (usually by a vector, with magnitude and direction according to sign convention) is not used for determining the orientation and/or position of the measured object in a given workpiece coordinate system. The first two types of distances include the Euclidean distance and the projected distance, requiring the coordinates of both nominal and measured points to be available. The second type of distance is the plumb line distance, representing the shortest distance from a measured point to the nominal geometry entity. The derived plumb line distance equation for cylindrical gears in [16] offers unique advantages when applied to evaluate geometric deviations of cylindrical gears.

2.3.1 Euclidean distance

To determine the Euclidean distance, each point in the cloud of measured points requires a corresponding point in the cloud of nominal points. This correspondence relationship is straightforward for most CMM based measurement, in which tactile probing is carried out to obtain a measured point according to its nominal location. In this case, the coordinates of the nominal points are generated by the measuring software. The distance of a measured point to its corresponding nominal point is shown in Figure 2.11. The Euclidean distance in the Cartesian coordinate system is:

$$|\vec{d}_{\text{Euc}}| = |\vec{p}_{\text{m}} - \vec{p}_{\text{nom}}| = \sqrt{(x_{\text{nom}} - x_{\text{m}})^2 + (y_{\text{nom}} - y_{\text{m}})^2 + (z_{\text{nom}} - z_{\text{m}})^2}\ . \qquad (2.13)$$

Obviously, the Euclidean distance can only be a non-negative value, defined as the magnitude of a vector pointing from a nominal point to a measured point.

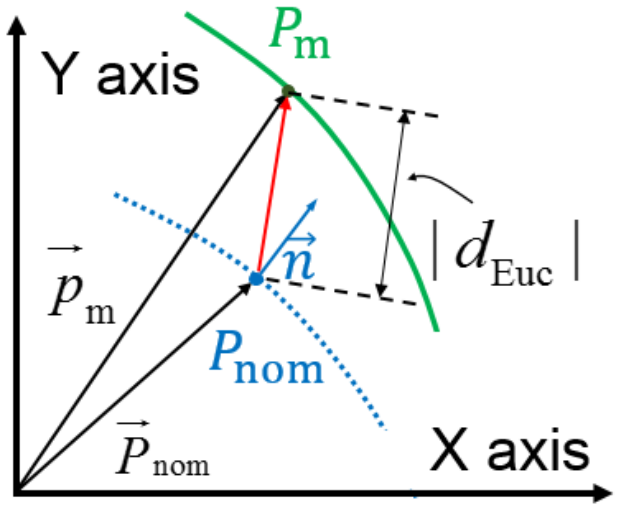

Figure 2.11: Euclidean distance between nominal point and measured point in a 2D Cartesian coordinate system.

2.3.2 Projected distance

When the surface normal vector is available, the projected distance can be found as the scalar product of the deviation vector and the unit normal vector at the nominal point as:

$$d_{\text{proj}} = (\vec{p}_{\text{m}} - \vec{p}_{\text{nom}}) \cdot \vec{n} = (x_{\text{m}} - x_{\text{nom}}) \cdot n_x + (x_{\text{m}} - x_{\text{nom}}) \cdot n_y + (z_{\text{m}} - z_{\text{nom}}) \cdot n_z . \qquad (2.14)$$

The relationship between the projected distance and the Euclidean distance is depicted in Figure 2.12. The projected distance is a signed quantity as determined by the vector scalar product.

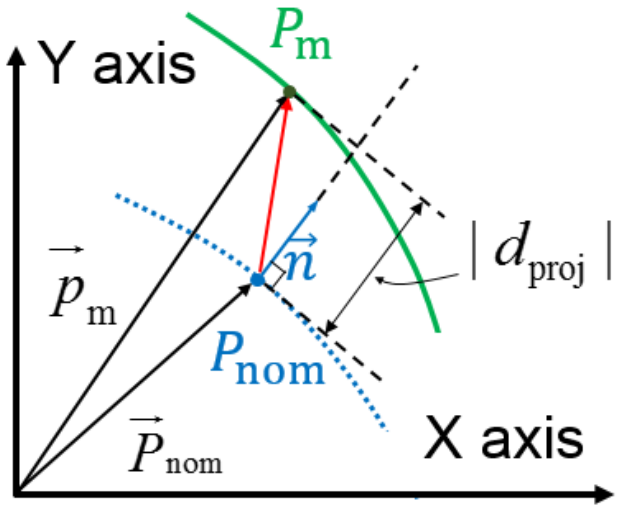

Figure 2.12: Projected distance between nominal point and measured point in a 2D Cartesian coordinate system.

Obviously, the coordinates of the nominal points are required to calculate those two types of distances, defined by Equation (2.13) and Equation (2.14). This imposes a major disadvantage of evaluating deviations in a point cloud based on those equations, because:

- a searching algorithm must be carried out to match a measured point to its corresponding nominal point before a distance calculation is possible;
- the surface normal vector must be available for the calculation of a projected distance, which could be obtained by three different methods: first, it is explicitly given as a type of nominal parameter (e.g. bevel gear flank); second, it is evaluated according to analytic formula (e.g. Equation (2.9)); third, it is estimated by the output signals of the probing system sensors (e.g. tactile probing head displacement vector);
- the nominal data is usually generated by software algorithms after the workpiece coordinate system is established. This step, as a key part of measurement software, is prone to numerous sources of intrinsic errors during the alignment procedure of the workpiece; thus, it represents an unavoidable source of uncertainty contribution.

2.3.3 Plumb line distance

The definition and derivation of the plumb line distance for a measured point of the cylindrical gear was first given in [16]. For a flank surface of an involute gear (spur and helical), the vectorial deviation from a measured point to its corresponding nominal geometry (not nominal point) in the nominal surface normal direction can be modeled by:

$$\vec{p}_{\mathrm{m}} = \vec{p}_{\mathrm{nom}} + \vec{d}_{\mathrm{lot}} = \vec{p}_{\mathrm{nom}} + \left|\vec{d}_{\mathrm{lot}}\right| \vec{n}, \tag{2.15}$$

where $\left|\vec{d}_{\mathrm{lot}}\right|$ denotes the magnitude plumb line distance. It is the magnitude of the vector pointing from the nominal point to the measured point. However, in the context of the plumb line distance of a cylindrical gear, this nominal point has a different meaning compared to the one mentioned in Section 2.3.1 and Section 2.3.2. As depicted in Figure

2.13, the nominal point is a “footprint” point, formed by a virtual “intersection” from a line connecting the measured point to the pure involute surface in the nominal surface normal direction.

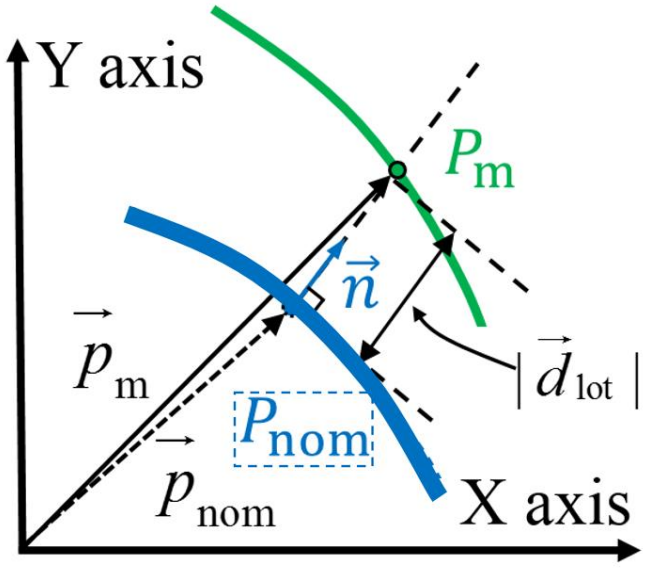

Figure 2.13: Plumb line distance between measured point and the nominal geometry in a 2D Cartesian coordinate system (nominal point with dashed line box).

The explicit expression of the plumb line distance is:

$$\left|\vec{d}_{\mathrm{lot}}\right| = \frac{r_{\mathrm{b}}}{\sqrt{1+(\tan\beta_{\mathrm{b}})^2}}\left\{\sqrt{\frac{\rho_{\mathrm{m}}^2}{r_{\mathrm{b}}^2}-1}-\arctan\sqrt{\frac{\rho_{\mathrm{m}}^2}{r_{\mathrm{b}}^2}-1}-\phi_{\mathrm{m}}+\eta_{\mathrm{b}}+z_{\mathrm{m}}\frac{\tan\beta_{\mathrm{b}}}{r_{\mathrm{b}}}\right\}, \qquad (2.16)$$

where $(\rho_{\mathrm{m}}, \phi_{\mathrm{m}}, z_{\mathrm{m}})$ is the coordinate of the measured point in a cylindrical coordinate system. The derivation of the analytic expression for the plumb line distance can be found in Appendix B.

The number of nominal points can be given by the number of measured points used in the evaluation of gear deviations. The two unique properties of the plumb line distance for cylindrical gears are:

- The plumb line distance is the shortest distance from a measured point to the nominal geometry (i.e. pure involute flank);
- The plumb line distance can be directly evaluated by the coordinates of a measured point.

Figure 2.14 depicts the relationship between a measured point, plumb line distance and a nominal point on the gear flank. Compared to Figure 2.3, the starting angle (Λ_{nom}) of a nominal profile in transverse plane is replaced by the base space width half angle η_b. This is because the X axis of a coordinate system can be arbitrarily chosen due to the rotational symmetry of the complete gear. In addition, by introducing the base space width half angle to the plumb line distance equation, the pressure angle and the number of teeth of a gear can be incorporated to an implicit equation, which will be discussed in the next section.

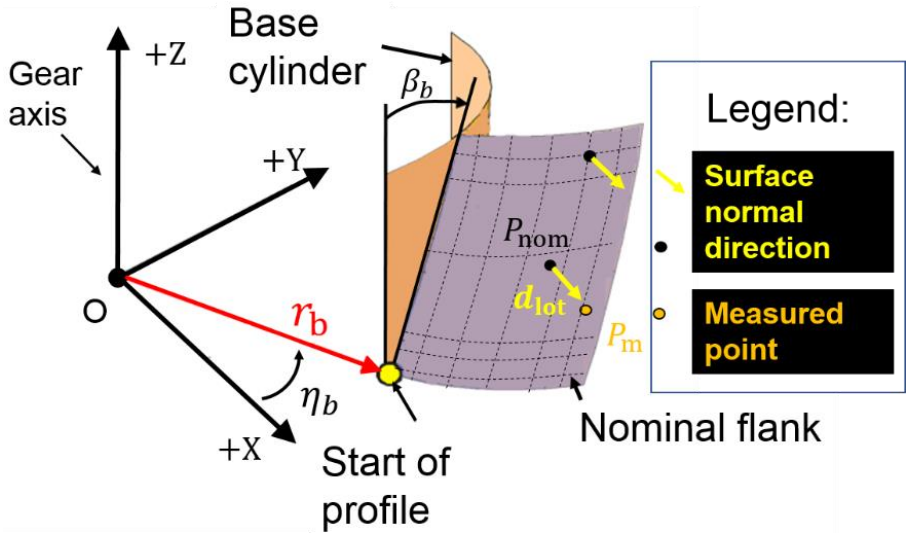

Figure 2.14: Schematic of the plumb line distance of a measured point P_m in a 3D Cartesian coordinate system.

Using the coordinates (in a cylindrical coordinate system) of a measured point

$$\begin{cases} \rho_{\mathrm{m}} = \sqrt{x_{\mathrm{m}}^2 + y_{\mathrm{m}}^2} = r_{\mathrm{b}} \sqrt{1 + \left(\xi_{\mathrm{nom}} + \dfrac{\left| \vec{d}_{\mathrm{lot}} \right|}{r_{\mathrm{b}} \sqrt{1 + (\tan \beta_{\mathrm{b}})^2}} \right)^2} \\ \phi_{\mathrm{m}} = \arctan\left(\dfrac{y_{\mathrm{m}}}{x_{\mathrm{m}}} \right) = \xi_{\mathrm{nom}} + \Lambda_{\mathrm{nom}} - \arctan\left(\xi_{\mathrm{nom}} + \dfrac{\left| \vec{d}_{\mathrm{lot}} \right|}{r_{\mathrm{b}} \sqrt{1 + (\tan \beta_{\mathrm{b}})^2}} \right), \\ z_{\mathrm{m}} = z_{\mathrm{nom}} + \dfrac{\tan \beta_{\mathrm{b}} \left| \vec{d}_{\mathrm{lot}} \right|}{r_{\mathrm{b}} \sqrt{1 + (\tan \beta_{\mathrm{b}})^2}} \end{cases} \quad (2.17)$$

the nominal values of $(\xi_{\mathrm{nom}}, \Lambda_{\mathrm{nom}}, z_{\mathrm{nom}})$ can also be determined, corresponding to a measured point by:

$$\begin{cases} \xi_{\mathrm{nom}} = \sqrt{\dfrac{\rho_{\mathrm{m}}^2}{r_{\mathrm{b}}^2} - 1} - \dfrac{\left| \vec{d}_{\mathrm{lot}} \right|}{r_{\mathrm{b}} \sqrt{1 + (\tan \beta_{\mathrm{b}})^2}} \\ \Lambda_{\mathrm{nom}} = \phi_{\mathrm{m}} - \sqrt{\dfrac{\rho_{\mathrm{m}}^2}{r_{\mathrm{m}}^2} - 1} + \arctan\left(\sqrt{\dfrac{\rho_{\mathrm{m}}^2}{r_{\mathrm{m}}^2} - 1} \right) + \dfrac{\left| \vec{d}_{\mathrm{lot}} \right|}{r_{\mathrm{b}} \sqrt{1 + (\tan \beta_{\mathrm{b}})^2}}. \\ z_{\mathrm{nom}} = z_{\mathrm{m}} - \dfrac{\tan \beta_{\mathrm{b}} \left| \vec{d}_{\mathrm{lot}} \right|}{\sqrt{1 + (\tan \beta_{\mathrm{b}})^2}} \end{cases} \quad (2.18)$$

The triplet $(\xi_{\mathrm{nom}}, \Lambda_{\mathrm{nom}}, z_{\mathrm{nom}})$ forms the coordinates of a "footprint" point on the nominal geometry (i.e. "pure" involute flank) corresponding to the measured point given by $(\rho_{\mathrm{m}}, \phi_{\mathrm{m}}, z_{\mathrm{m}})$. This one-to-one matching relationship marks the unique advantage of using the plumb line distance to characterize the actual distances from point cloud to the nominal flank geometry.

2.4 Implicit equation for cylindrical gear

By substituting the base space half angle η_{b} in Equation (2.16) by Equation (2.4), the plumb line distance is rewritten in terms of pressure angle α_{t} and helical angle β:

$$\left|\vec{d}_{\text{lot}}\right| = \frac{r_{\text{b}}}{\sqrt{1+(\cos\alpha_{\text{t}}\tan\beta)^2}} \cdot\left\{\sqrt{\frac{\rho_{\text{m}}^2}{r_{\text{b}}^2}-1}-\arctan\sqrt{\frac{\rho_{\text{m}}^2}{r_{\text{b}}^2}-1}-\phi_{\text{m}}+\frac{\pi}{2\text{z}}-\tan\alpha_{\text{t}}+\alpha_{\text{t}}+\text{z}_{\text{m}}\frac{\cos\alpha_{\text{t}}\tan\beta}{r_{\text{b}}}\right\}. \quad (2.19)$$

Setting the Equation (2.19) to zero leads to an implicit expression of the pure involute gear geometry. In other words, if $\left|d_{\text{lot}}\right| = 0$, the coordinate $(\rho_{\text{m}}, \phi_{\text{m}}, \text{z}_{\text{m}})$ is equal to the corresponding nominal point $(\rho_{\text{nom}}, \phi_{\text{nom}}, z_{\text{nom}})$. The zero-valued Equation (2.19) contains all information about the geometry of the entire flank and the nominal coordinate $(\rho_{\text{nom}}, \phi_{\text{nom}}, z_{\text{nom}})$ on the flank, for the following reasons:

- the basic shape of the involute is determined by base radius r_{b} of the base circle;
- the size of the gear (e.g. reference radius) is determined by base radius r_{b} and the transverse pressure angle (α_{t}) at the pitch diameter: $r = r_{\text{b}} / \cos\alpha_{\text{t}}$;
- the shape of the flank surface is determined by the helix angle β;
- the volume of the size is determined by the face width of the gear, as the maximum value of z_{nom} (i.e. *b*); and
- the relative angular position of each tooth (including its left and right flank) is determined by the integer (indexed from 1 to the number of teeth z).

Writing Equation (2.19) to an implicit form:

$$F(\rho_{\text{nom}}, \phi_{\text{nom}}, z_{\text{nom}}; r_{\text{b}}, \alpha_{\text{t}}, \beta, \text{z}) = 0 \quad (2.20)$$

leads to three significant implications:

- first, it proves the advantage of direct calculation of the distance from a measured point to the nominal gear flank without using the nominal coordinates,

which is analogeous to the implicit equations describing simple geometries such as circles, cylinders and spheres in CMM technologies;

- second, it provides a theoretical guide to determine, which fundamental gear parameters could be selected as the degrees of freedom, if an approximation method is used to obtain the deviation of them from measured point clouds;
- third, if $F(\rho_{\mathrm{nom}}, \phi_{\mathrm{nom}}, z_{\mathrm{nom}}; r_{\mathrm{b}}, \alpha_{\mathrm{t}}, \beta, \mathrm{z}) = a \neq 0$, the measured point cloud forms an equidistant surface shifted from the nominal flank in the surface normal direction, which can be practically interpreted as a pitch deviation and can be used for rotational alignment within areal evaluation (see Section 4.2.1).

Throughout this dissertation, both $F(\rho, \phi, z; r_{\mathrm{b}}, \alpha_{\mathrm{t}}, \beta, \mathrm{z})$ and $F(x, y, z; r_{\mathrm{b}}, \alpha_{\mathrm{t}}, \beta, \mathrm{z})$ can be equally interpreted as the implicit representation of a flank, regardless of the choice of coordinate systems.

Figure 2.15 (a) summarizes the relationship between the pure involute flank and the actual flank from a geometric perspective, while Figure 2.15 (b) illustrates the numerical consequence of calculating the deviation based on the plumb line distance equation.

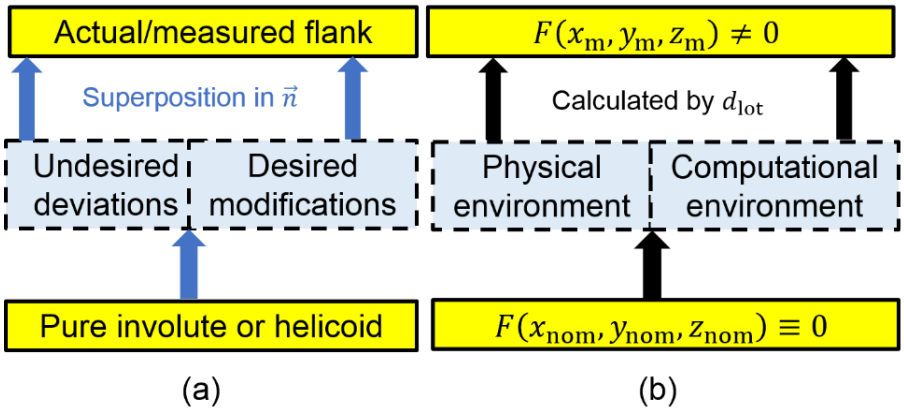

Figure 2.15: Relationship between nominal geometry and measured areal distance map: (a), superimposed deviation and/or modification to a nominal cylindrical gear flank; (b), mathematical conequences of (a) towards the implicit equation of cylindrical gear flank.

2.4.1 Implicit equation of individual flank

A set of nominal points with coordinates $(x_{nom}, y_{nom}, z_{nom})$ on a gear flank are generated by Equation (2.3) based on the gear parameters in Table 2.1. As shown in Figure 2.16 (a), those points constitute a right flank of the gear in 3D space. Afterwards, these coordinates are evaluated by the plumb line distance equation, which leads to an areal distance map shown in Figure 2.16 (b). This result verifies the prediction of zero-valued output (10^{-14} mm, machine precision of MATLAB®) of all the plumb line distances calculated from the coordinates of those nominal points.

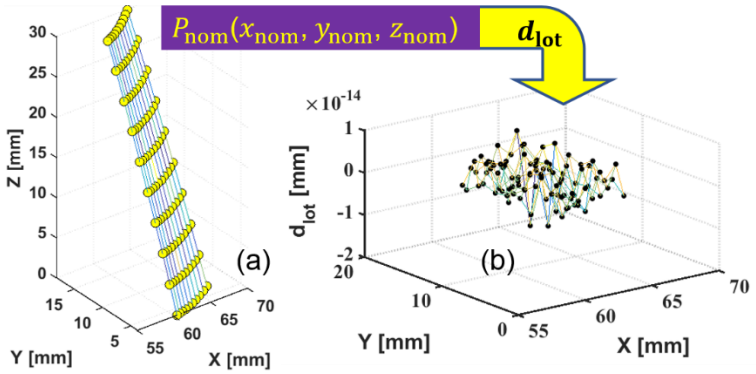

Figure 2.16: Simulated nominal points on a flank: (a), in 3D Cartesian coordinate system; (b), the plumb line distance plotted as a function of spatial location in the X-Y plane.

2.4.2 Implicit equation for a complete gear teeth system

To evaluate the tooth-to-tooth features of a gear, an analytic model of the complete gear (including both flanks of all teeth) is essential. Extending the implicit individual flank equation for a complete gear, extra parameters are needed, such as: the flank direction (left or right), the tooth number index (tooth #1, #2, …, #z) and the tooth counting direction (clock wise, CW or counter-clock wise, CCW). The tooth index number is defined as t_{ind}, an integer varying from 1 to the number of teeth z. The flank direction is denoted as *f*,

taking the values of 1 and -1 for right and left flank, respectively. The gear tooth counting direction, denoted as c_t, is defined as the direction of counting from the first to the second tooth, when the gear datum surface is facing out of the paper. The choice of c_t is 1 and -1 for counter-clock-wise (CCW) and clock-wise (CW), respectively.

Due to the rotational symmetry of a gear body, the nominal location of an individual tooth is uniquely determined by the value of its nominal starting angle. The choice of using base space half width angle of the first gear tooth (indicated as #1) can be extended for the succeeding teeth. For an arbitrary tooth-gap pair, confined in an arbitrary circle with diameter d_y, an invariant quantity exists as:

$$2(\psi_y + \eta_y) = \frac{2\pi}{z}, \tag{2.21}$$

where ψ_y and η_y are the tooth thickness half angle and the space width half angle, respectively. A specific case is shown in Figure 2.17 for the corresponding angles on the pitch diameter.

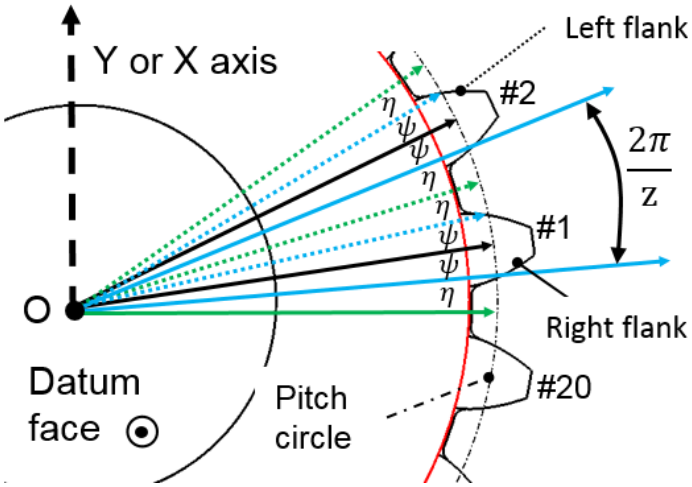

Figure 2.17: The half space angle (η) and the tooth thickness half angle (ψ) on the pitch circle of a counter-clock-wise indexed gear: left flank (dotted line) and right flank (solid line).

In nominal gear geometry, the start and end values of the roll angle determine the range of all profiles of right flanks of each tooth. The location of each profile is uniquely determined by the nominal starting angle $\Lambda_{\text{nom}}(t_{\text{ind}}, f, c_{\text{t}})$.

For simplicity, it is assumed that the workpiece coordinate system's X axis is located in the middle of the space between the first and last tooth of the gear, as shown in Figure 2.18. The analytic equation of the nominal starting angle of the right flank on the tooth #1 in CCW direction is:

$$\Lambda_{\text{nom}}(1,\text{R},\text{CCW})=\Lambda_{\text{nom}}(1,1,1)=\eta_{\text{b}}+z_{\text{nom}}\frac{\tan\beta\cos\alpha_{\text{t}}}{r_{\text{b}}}. \tag{2.22}$$

Apparently, by substituting the invariant quantity on the right side of Equation-(2.21), Equation (2.22) can be extended to any right flanks on all teeth, as:

$$\Lambda_{\text{nom}}(t_{\text{ind}},\text{R},\text{CCW})=\eta_{\text{b}}+z_{\text{nom}}\frac{\tan\beta\cos\alpha_{\text{t}}}{r_{\text{b}}}+(t_{\text{ind}}-1)\frac{2\pi}{z}, \tag{2.23}$$

where $t_{\text{ind}}=2,3,...,z$ is the tooth index number.

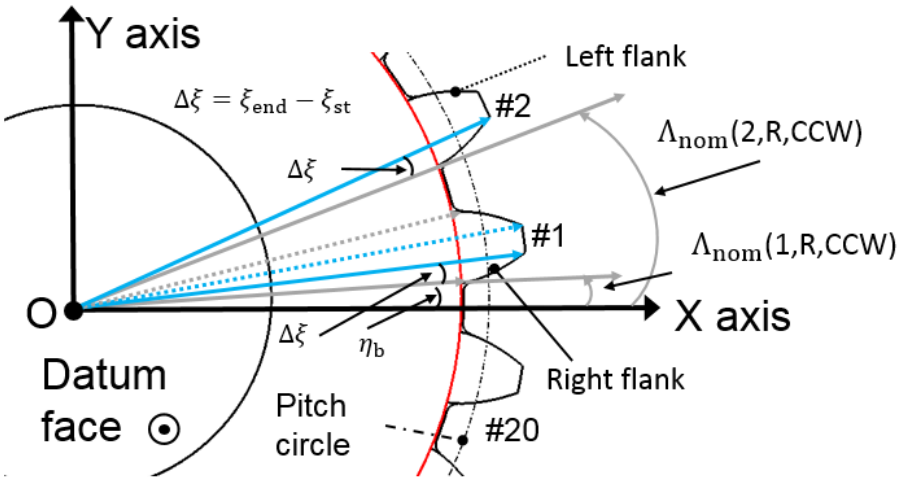

Figure 2.18: Schematic of the nominal starting angles on right flanks of tooth #1 and #2.

For the left flank, as shown in Figure 2.19, the nominal starting angle of tooth #1 is shifted in counter-clock-wise direction by the angular amount of $2\pi / \mathrm{z} - 2\eta_{\mathrm{b}}$ as:

$$\Lambda_{\mathrm{nom}}(1,\mathrm{L},\mathrm{CCW}) = \Lambda_{\mathrm{nom}}(1,-1,1) = \eta_{\mathrm{b}} + z_{\mathrm{nom}} \frac{\tan\beta\cos\alpha_{\mathrm{t}}}{r_{\mathrm{b}}} + \frac{2\pi}{\mathrm{z}} - 2\eta_{\mathrm{b}}\,. \qquad (2.24)$$

Similarly, Equation (2.24) can be extended to a general form for all the left flanks of all teeth as:

$$\Lambda_{\mathrm{nom}}(t_{\mathrm{ind}},\mathrm{L},\mathrm{CCW}) = \eta_{\mathrm{b}} + z_{\mathrm{nom}} \frac{\tan\beta\cos\alpha_{\mathrm{t}}}{r_{\mathrm{b}}} + \frac{2\pi}{\mathrm{z}} - 2\eta_{\mathrm{b}} + (t_{\mathrm{ind}} - 1)\frac{2\pi}{\mathrm{z}}\,. \qquad (2.25)$$

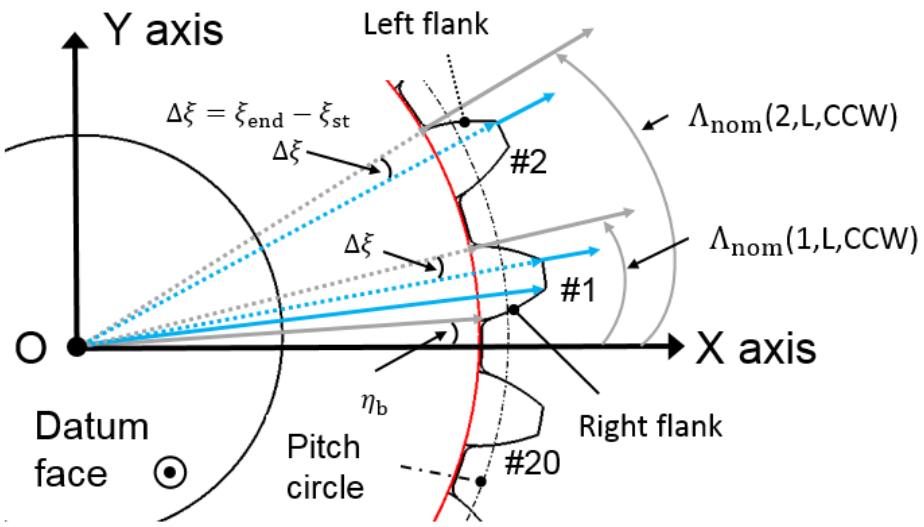

Figure 2.19: Schematic of the nominal starting angles on left flanks of tooth #1 and #2.

Combining Equation (2.23) and Equation (2.25) the analytic form of the nominal starting angle $\Lambda_{\mathrm{nom}}(t_{\mathrm{ind}}, f, c_{\mathrm{t}})$ for both left and right flanks can be written as:

$$\Lambda_{\mathrm{nom}}(t_{\mathrm{ind}}, f, c_{\mathrm{t}}) = \eta_{\mathrm{b}} + z_{\mathrm{nom}} \frac{\tan\beta\cos\alpha_{\mathrm{t}}}{r_{\mathrm{b}}} + (1-f)\left(\frac{\pi}{\mathrm{z}} - \eta_{\mathrm{b}}\right) + c_{\mathrm{t}}(t_{\mathrm{ind}} - 1)\frac{2\pi}{\mathrm{z}}\,. \qquad (2.26)$$

Substituting Equation (2.26) to the plumb line distance equation in Section 2.3.3, the whole gear teeth system can be written as:

$$\frac{r_{\mathrm{b}}}{\sqrt{1+(\cos\alpha_{\mathrm{t}}\tan\beta)^2}}\left\{\begin{array}{l}\sqrt{\frac{\rho_{\mathrm{m}}^2}{r_{\mathrm{b}}^2}-1}-\arctan\sqrt{\frac{\rho_{\mathrm{m}}^2}{r_{\mathrm{b}}^2}-1}-\phi_{\mathrm{m}}+\eta_{\mathrm{b}}+\\ z_{\mathrm{m}}\dfrac{\cos\alpha_{\mathrm{t}}\tan\beta}{r_{\mathrm{b}}}+(1-f)\left(\dfrac{\pi}{\mathrm{z}}-\eta_{\mathrm{b}}\right)+c_{\mathrm{t}}(t_{\mathrm{ind}}-1)\dfrac{2\pi}{\mathrm{z}}\end{array}\right\}=0\,, \quad (2.27)$$

where, $\eta_{\mathrm{b}}=\pi/\mathrm{z}-\tan\alpha_{\mathrm{t}}+\alpha_{\mathrm{t}}$.

Equation (2.27) leads to the following implicit representation of the whole gear teeth system is:

$$F(x_{\mathrm{nom}},y_{\mathrm{nom}},z_{\mathrm{nom}};\alpha_{\mathrm{t}},\beta,r_{\mathrm{b}},\mathrm{z},t_{\mathrm{ind}},f,c_{\mathrm{t}})=0\,, \quad (2.28)$$

which contains all nominal geometric information of every flank of a complete gear.

Moreover, the formation of equation (2.28) fulfills the geometric angular closure principle, as analogous to the conservation laws in physics. As mentioned, if the function equals a non-zero valued constant, $F(x_{\mathrm{m}},y_{\mathrm{m}},z_{\mathrm{m}};t_{\mathrm{ind}},...)=a_{t_{\mathrm{ind}}}$, for an individual flank, then the summation of each value $a_{t_{\mathrm{ind}}}$ should always be zero:

$$\sum_{t_{\mathrm{ind}}=1}^{\mathrm{z}}F(x_{\mathrm{m}},y_{\mathrm{m}},z_{\mathrm{m}};t_{\mathrm{ind}},...)=\sum_{t_{\mathrm{ind}}=1}^{\mathrm{z}}a_{t_{\mathrm{ind}}}=0 \quad (2.29)$$

In fact, this relationship is readily reasonable, when each individual constant value $a_{t_{\mathrm{ind}}}$ is interpreted as the individual single pitch deviation for the corresponding flank. More detailed discussion of single pitch deviation will be presented in Chapter 4.

CHAPTER 3 : APPROXIMATION BY CHEBYSHEV SERIES

3.1 Introduction and basic concepts

Similar to the prevalent application of Fourier series to approximate periodic functions in harmonic analysis, Chebyshev series play a vital role in approximating nonperiodic functions in numerical analysis [50]. In computational metrology, the concept of Chebyshev approximation is applied to obtain the minimum zone fit of geometric features (such as planes, circles, cylinders, etc.) from a measured data set [51]. One reason for its popularity in dimensional metrology is that the Chebyshev approximation keeps the maximum error to a minimum. This is of particular importance in the study of Geometric Dimensioning and Tolerancing (GD&T), when a measured feature on a workpiece must be compared to its designed intent [52] with a quantitative value of deviation. Another advantageous property of using the Chebyshev polynomials to approximate arbitrary functions is its orthogonality, which uniquely facilities the calculation of Chebyshev coefficients. A comparison of the properties of Chebyshev polynomials with other orthogonal polynomials was investigated in [53]. However, the rigorous mathematical discussion of the popularity of Chebyshev polynomials is beyond the scope of this dissertation.

The first sub-section of this chapter is focused on basic definitions and key properties related to the Chebyshev approximation of functions with a single independent variable (referred to as 1D Chebyshev polynomials). Afterwards, interpretations of applying 1D Chebyshev series and their mathematical properties to approximate gear flank surfaces are presented. Lastly, the analytic expressions of the 2D Chebyshev polynomials

are introduced. Simulation results for approximating an arbitrary bivariate function by 2D Chebyshev series are studied.

3.1.1 Chebyshev norm and Chebyshev approximation

In physics and engineering, the concept of distance is ubiquitous. From a rigorous mathematical perspective, the definition of a distance in dimensional metrology is of critical importance. One commonly used quantity is the point-to-point distance in a 3D Euclidean space. Alternatively, the concept "norm" can be used to extend the interpretation of a distance from its geometrical meaning to an algebraic abstraction. A norm is defined on a space that consists of points, vectors or even functions, attributed with a list of properties. It is a function that assigns a positive value of length to the mathematical objects of interest. How the norm is calculated depends on the way it is defined. For example, the L_p norm used in functional analysis is defined by:

$$\|\mathbf{x}\|_p = \left(\sum_{i=1}^{n} |x_i|^p \right)^{1/p}, \text{ with } p \geq 1, \mathbf{x} = (x_1, x_2, ..., x_n), \tag{3.1}$$

where x_1, x_2 and x_n can be coordinates, points, vectors or functions. In practice, the most common values for the parameter p are 1, 2 and ∞, which are known as the "absolute norm", the "Euclidean norm" or "Gaussian norm" and the "infinity norm" respectively. The Chebyshev norm ($p = \infty$) can also be referred to as supremum norm, uniform norm and infinity norm.

In geometry measurement, Chebyshev approximation is the approximation that minimizes the maximum distance (i.e. Chebyshev norm) between the measured data and the approximated function that characterizes the measured object. Various searching methods and optimization algorithms were developed to implement the Chebyshev

approximation with reasonable computational efforts [54]. The implementation of a Chebyshev approximation according to its definition is a challenging optimization problem, raising numerical difficulties in dimensional metrology practice [55]. An alternative solution to this challenge is based on an iterative algorithm and a reasonably large value of p (e.g. $50 \leq p \leq 100$) [56].

In this chapter, the Chebyshev series in 1D and 2D are used as an implementation method for Chebyshev approximation on measured discrete dataset in gear inspection.

3.1.2 Chebyshev polynomials (1D)

Chebyshev polynomials form a family of orthogonal polynomials in numerical analysis and scientific computing. For an integer $k \geq 0$, the Chebyshev polynomial of degree k is denoted as $T_k(x)$ and is given by:

$$T_k(x) = \cos[k \cdot \arccos(x)], k = 0, 1, 2, \ldots, \infty. \quad x \in [-1,1] \tag{3.2}$$

This integer k also refers to a corresponding "term", which is a member of the Chebyshev polynomials. Each Chebyshev term satisfies a three-term recurrence relation:

$$T_{k+1}(x) = 2xT_k(x) - T_{k-1}(x), \quad k \geq 1, \tag{3.3}$$

with $T_0(x) = 1$ and $T_1(x) = x$ as the first and second term respectively.

The first six terms of the 1D Chebyshev polynomials are:

$$\begin{aligned} T_0(x) &= 1 \\ T_1(x) &= x \\ T_2(x) &= 2x^2 - 1 \\ T_3(x) &= 4x^3 - 3x \\ T_4(x) &= 8x^4 - 8x^2 + 1 \\ T_5(x) &= 16x^5 - 20x^3 + 5x \end{aligned} \quad . \tag{3.4}$$

The term index k is equal to the number of zeros of the polynomial $T_k(x)$ as shown graphically in Figure 3.1.

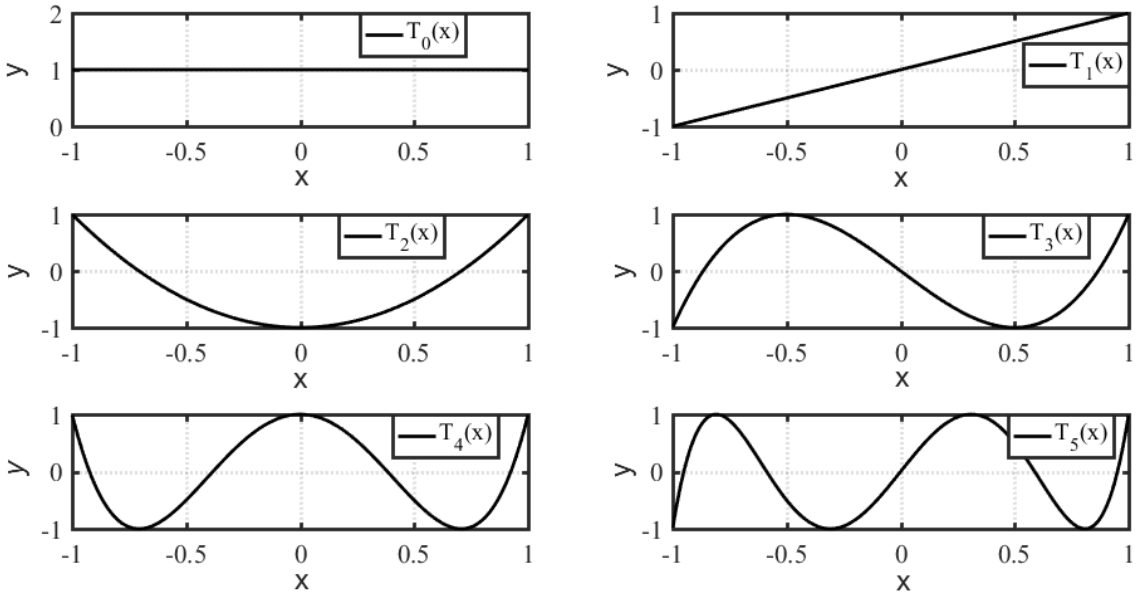

Figure 3.1 The first six terms $T_k(x)$ ($k = 0, 1, 2, \ldots, 5$) of 1D Chebyshev polynomials.

3.1.3 1D Chebyshev points

1D Chebyshev points are the extreme points of 1D Chebyshev polynomials [57]. For a 1D Chebyshev polynomial of maximum degree of *N*, there are *N*+1 1D Chebyshev points given by:

$$x_{1D}(j) = \cos(j\pi / N),\ 0 \le j \le N\ , \tag{3.5}$$

where j is an integer varying from 0 to *N*. In Figure 3.2, 17 Chebyshev points are generated and represented by red dots on the interval of [-1,1]. Obviously, the Chebyshev points cluster near the edge of -1 and 1. The black dots represent the 17 points, which are equispaced on the unit circle, corresponding to the Chebyshev points.

In numerical analysis, it is well known that polynomial interpolation by 1D Chebyshev points by the barycentric interpolation formula has an advantage over the equispaced points interpolation [50]. However, in this dissertation another form of approximation by Chebyshev series is used rather than an interpolation at Chebyshev points.

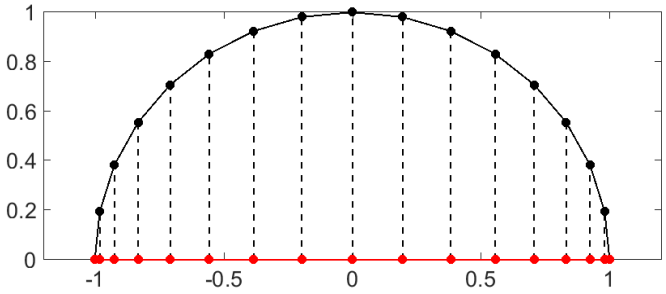

Figure 3.2: Location of 17 Chebyshev points (red dots) on the interval [-1,1].

3.1.4 Chebyshev series and 1D Chebyshev expansion

Trigonometric functions (sine and cosine) are the default choices as base functions to approximate a periodic function in harmonic analysis. Similarly, the Chebyshev polynomials can serve as base functions to approximate any non-periodic function on an interval in numerical analysis. Mason et al. provided a rigorous presentation of the mathematical properties of Chebyshev polynomials in [58].

If a function $f(x)$ is Lipschitz continuous on the interval [-1,1], it has a unique representation as a series, summed by infinite terms of Chebyshev polynomials:

$$f(x) = \sum_{k=0}^{\infty} c_k T_k(x), \tag{3.6}$$

which is absolutely and uniformly convergent [50]. The coefficient c_k associated with each term of the Chebyshev polynomial is called the Chebyshev coefficient of term *k*. The series

given by Equation (3.6) is known as Chebyshev series or Chebyshev expansion, which can be an alternative to the Chebyshev approximation of the function $f(x)$ [58].

However, truncation of an infinite series in Equation (3.6) after a certain number of terms *N*, is of more practical importance, particularly when a uniform tolerance band is predefined for the approximation problem. This truncation, denoted by $f_N(x)$ is given by:

$$f(x) \approx f_N(x) = \sum_{k=0}^{N} c_k T_k(x). \tag{3.7}$$

In addition, the truncation after the N^{th} term of a Chebyshev polynomial $T_N(x)$ approximately satisfies the equioscillation property of the best approximation [57] as:

$$E_N(x) = \sum_{k=N+1}^{\infty} c_k T_k(x) \approx c_{k+1} T_{k+1}(x), \tag{3.8}$$

in which $E_N(x)$ is the residual error due to truncation.

The value of the k^{th} Chebyshev coefficient in Equation (3.7) is explicitly given by the integral:

$$c_k = \frac{2}{\pi} \int_{-1}^{1} \frac{f(x) T_k(x)}{\sqrt{1-x^2}} dx, \tag{3.9}$$

where, $k \geq 1$. For *k*=0, the factor changes from $2/\pi$ to $1/\pi$.

3.2 Properties of 1D Chebyshev series and physical interpretation

3.2.1 Orthogonality

The orthogonality of the Chebyshev polynomials is given by the integral:

$$\int_{-1}^{1} \frac{T_i(x) T_j(x)}{\sqrt{1-x^2}} dx = K = \begin{cases} \pi, i = j = 0 \\ 0, i \neq j \\ \dfrac{\pi}{2}, i = j \geq 1 \end{cases}, \tag{3.10}$$

where K is known as the normalization factor for the 1D Chebyshev polynomials.

This property leads to the fact that, the value of each coefficient c_k corresponding to each base function $T_k(x)$ can be calculated independently, which offers two practical advantages:

- The value of an invidiual coefficient c_k does not depend on the total number of terms (N in Equation (3.7)) used for the approximation;
- The removal of certain compnoents (e.g. $c_k T_k(x)$) from the mesasured data set does not affect the values of other coefficeints (i.e. $c_{j\neq k}$) calcuated from the data set after removing $c_k T_k(x)$.

3.2.2 Near best approximation

The definition of a near best approximation is given in [50], which states that the norm of an approximation based on the truncated 1D Chebyshev series is no larger than a bounded factor of the best approximation:

$$\left\| f(x) - f_N(x) \right\|_\infty \leq \left(4 + \frac{4}{\pi^2} \log(N+1) \right) \left\| f(x) - p_N^* \right\|_\infty , \tag{3.11}$$

where $f(x)$ is the function to be approximated, $f_N(x)$ is the truncation of a 1D Chebyshev series to degree N as in Equation (3.7), and p_N^* is the theoretical best approximation by a polynomial with the maximum degree of N, respectively.

3.2.3 Parseval's theorem

In harmonic analysis, the summability property of an infinite Fourier series expansion of a function is given by Parseval's theorem, which asserts that the sum of the

squares of the Fourier coefficients of a function is equal to the integral of the square of the function. The counterpart theorem for the infinite Chebyshev series holds [57]:

$$2c_0^2 + \sum_{k=1}^{\infty} c_k^2 = \frac{2}{\pi}\int_{-1}^{1} \frac{f(x)^2}{\sqrt{1-x^2}}\,dx, \tag{3.12}$$

where the scaling factor 2 on c_0^2 is used, when each coefficient is evaluated by an integral:

$$c_k = \frac{2}{\pi}\int_{-1}^{1} \frac{f(x)T_k(x)}{\sqrt{1-x^2}}\,dx. \tag{3.13}$$

The Parseval's theorem is a direct consequence of the completeness nature of using Chebyshev polynomials as the base functions [58] [59]. Parseval's theorem can be used as a tool to quantify the "energy" contribution of each Chebyshev term, represented by its corresponding coefficient.

Beyond the mathematical properties of using Chebyshev polynomials to approximate a function in an interval, several advantages from an engineering perspective are summarized in Table 3.1.

Table 3.1: Interpretation of mathematical properties and applications of Chebyshev polynomials on areal gear flanks.

Mathematical property	**Geometric interpretation**	**Engineering application**
Near best approximation	Minimized max errors	Reconstruction of form
Equal ripple residue	Symmetric deviation band	Uniform tolerance zone
Base functions and orthogonality	Independent surface spatial components	Low order flank modifications/deviations
Coefficient for each base function	Contribution of a surface component	Magnitude of each flank modification/deviation
Parseval's theorem	Conservation of energy of all surface components	Percentage of certain modification/deviation

3.3 Approximation of discrete data by power series

The fundamental theorem, proven by Weierstrass in 1885, states that any continuous function defined on a closed interval can always be approximated to any degree of accuracy by power polynomials. However, it is not guaranteed that an approximating polynomial can be obtained based on equidistant data, a widely met practical case when analyzing engineering measurement data. A phenomenon discovered by Runge in 1901, signifies the divergence issue, even when a simple analytic function is approximated on equidistant points within a real interval.

$$f(x) \approx p_N(x) = \sum_{k=0}^{N} a_k x^k \tag{3.14}$$

As shown in Equation (3.14), the power series $p_N(x)$ at the highest order of N is defined as a finite sum of monomial x^k at the order of k, associated with a corresponding coefficient a_k.

The coefficient a_k is usually determined by interpolation, based on a set of M equally spaced sampling values x_i and the corresponding observation values $f(x_i)$, with $i = 1, 2, ..., M$. Equation (3.15) shows the formation of the interpolation problem to calculate the N+1 coefficients with values a_k:

$$\begin{cases} f(x_1) = a_0 + a_1 x_1 + a_2 x_1^2 + \cdots + a_N x_1^N \\ f(x_2) = a_0 + a_1 x_2 + a_2 x_2^2 + \cdots + a_N x_2^N \\ \vdots \\ f(x_M) = a_0 + a_1 x_M + a_2 x_M^2 + \cdots + a_N x_M^N \end{cases} . \tag{3.15}$$

3.3.1 Least squares solution of normal equation

The Least squares method is often used to solve the overdetermined system of Equation- (3.15), since the number of measured points *M* is usually much larger than the highest order *N* of the polynomial $p_N(x)$:

$$\begin{bmatrix} 1 & x_1 & x_1^2 & \cdots & x_1^N \\ 1 & x_2 & x_2^2 & \cdots & x_2^N \\ & & \cdots & & \\ 1 & x_M & x_M^2 & \cdots & x_M^N \end{bmatrix} \cdot \begin{bmatrix} a_1 \\ a_2 \\ \vdots \\ a_N \end{bmatrix} = \begin{bmatrix} f(x_1) \\ f(x_2) \\ \vdots \\ f(x_M) \end{bmatrix}. \tag{3.16}$$

Severe issues arise, when a set of discrete data is approximated by power series to arbitrary orders, formulated to the least square problem and solved by a normal equation:

- the choice of the highest order *N* is subjectively decided, if no prior information such as the allowable maximum residue errors is given;
- the coefficients for the individual mononic power terms (i.e. base functions) can not be obtained independently since they are not orthogonal with respect to each other;
- the widely used algorithm “polyval/polyfit” in MATLAB for solving a Vandermonde linear system determining the coefficeint of a vector normal equation is unstable in the presence of rounding errors [50]; and,
- even though the equidistant abscissa of x_i is ubiquitous (preferred from a data acquisition perspective), an interpolation on equidistant points is numerically ill-conditioned, when a high order power function is used [50].

3.3.2 Coefficients of 1D Chebyshev series and 1D power series

For instance, a non-periodic function $f_{\mathrm{P}}(x)$ is defined in a finite interval by a power series with a maximum order of 5 as:

$$f_{\mathrm{P}}(x) = a_0 + a_1 x + a_2 x^2 + a_3 x^3 + a_4 x^4 + a_5 x^5 . \tag{3.17}$$

It is straightforward that a Chebyshev series $f_{\mathrm{T}}(x)$ with the same order of 5 can be used to describe the same function $f_{\mathrm{P}}(x)$ by:

$$f_{\mathrm{T}}(x) = c_0 T_0(x) + c_1 T_1(x) + c_2 T_2(x) + c_3 T_3(x) + c_4 T_4(x) + c_5 T_5(x) . \tag{3.18}$$

By setting $f_{\mathrm{P}}(x) = f_{\mathrm{T}}(x)$, the relationship between the coefficients of the 1D power series and the 1D Chebyshev coefficients can be uniquely determined by comparing the order of each monomial term in Equation (3.17) and Equation (3.18):

$$\begin{cases} c_0 = a_0 + \dfrac{a_2}{2} + \dfrac{3a_4}{8} \\ c_1 = a_1 + \dfrac{3a_3}{4} + \dfrac{5a_5}{8} \\ c_2 = \dfrac{a_2}{2} + \dfrac{a_4}{2} \\ c_3 = \dfrac{a_3}{4} + \dfrac{5a_5}{16} \\ c_4 = \dfrac{a_4}{8} \\ c_5 = \dfrac{a_5}{16} \end{cases} . \tag{3.19}$$

Equation (3.19) can be written in a matrix form:

$$\begin{bmatrix} c_0 \\ c_1 \\ c_2 \\ c_3 \\ c_4 \\ c_5 \end{bmatrix} = \begin{bmatrix} 1 & 0 & 1/2 & 0 & 3/8 & 0 \\ 0 & 1 & 0 & 3/4 & 0 & 5/8 \\ 0 & 0 & 1/2 & 0 & 1/2 & 0 \\ 0 & 0 & 0 & 1/4 & 0 & 5/16 \\ 0 & 0 & 0 & 0 & 1/8 & 0 \\ 0 & 0 & 0 & 0 & 0 & 1/16 \end{bmatrix} \begin{bmatrix} a_0 \\ a_1 \\ a_2 \\ a_3 \\ a_4 \\ a_5 \end{bmatrix}, \tag{3.20}$$

which can be expressed as:

$$\mathbf{C} = \mathbf{M}\mathbf{A}, \tag{3.21}$$

where **C** is the vector of 1D Chebyshev coefficients, **A** is the vector of 1D power coefficients and **M** is the square matrix with a size of 5 by 5. This relationship can be generalized to any arbitrary order of *N*, and the matrix **M** is an upper-triangular matrix with a size of *N* by *N*.

In addition, for the highest order (i.e. $k = N$), the coefficients obtained by approximating an unknown function by both a power series and a Chebyshev series, satisfy the following relationship:

$$c_N = \frac{a_N}{2^{N-1}}, \tag{3.22}$$

which indicates that the Chebyshev series converges more rapidly than the power series. In fact, the speed of convergence when an analytic function is approximated by Chebyshev series is geometric [50], thus less terms are needed to approach a given approximation criteria such as a given band of truncation error.

As a unique type of a family of orthogonal polynomials (i.e. the Jacobi polynomials), the Chebyshev polynomials distinguish themselves by several advantages as summarized by Boyd [53]. From a mathematical perspective, the two most important advantages of choosing Chebyshev polynomials over other types of polynomials (e.g.

Legendre polynomials) in this dissertation are the "Minimal L_∞ error for a general function" and the "convertible to Fourier Cosine" property as stated in Figure 3.3

Criterion of merit	Winner	Remarks
Minimal L_∞ error for general $f(x)$	Chebyshev	Exceptions noted below
Minimal $E_N^{\alpha,\beta}$ error	Jacobi $P_n^{\alpha,\beta}$	By definition
FFT-applicability	Chebyshev	Reduces interpolation cost $O(N^2) \rightarrow O(N \log_2(N))$
Unweighted integration-by-parts (finite/spectral elements)	Legendre	Simplifies programming & variational formulation
Convertible to Fourier cosine	Chebyshev	Simplifies programming and theory
Endpoint singularities: minimize interior error	Gegenbauer	Heart of "Gibbs reprojection"
Minimize error for $f_m(\theta) = \sin^m(\theta) P(\cos(\theta))$ where $f(\lambda, \theta) = \sum_m f_m(\theta) \cos(m\lambda)$	Gegenbauer	Spherical geometry
Minimize error for $f_m(r) = r^m P(r)$ where $f(r, \theta) = \sum_m f_m(r) \cos(m\theta)$	Jacobi	Cylindrical geometry

Figure 3.3: Comparisons of Chebyshev, Legendre, Jacobi and Gegenbauer polynoimals [53].

3.4 Chebyshev polynomials defined on 2D domain

3.4.1 Generation of 2D Chebyshev polynomials

The 2D Chebyshev polynomials can be generated by the multiplication of two 1D Chebyshev polynomials in two perpendicular directions by:

$$C_n(x, y) = T_p(x) \cdot T_q(y), \tag{3.23}$$

where $T_p(x)$ and $T_q(x)$ are the 1D Chebyshev polynomials in the X direction and the Y direction, respectively. This leads to the bivariate representation $C_n(x, y)$, defined on the square domain $[-1,1]^2$, where both x and y vary in the interval $[-1,1]$.

The subscript n of $C_n(x, y)$ represents the term number of the 2D Chebyshev polynomials ascendingly. The expressions of the first nine terms (n = 0, 1, 2, …, 8) of 2D Chebyshev polynomials are given in Equation (3.24):

$$\begin{aligned}
&C_0(x,y) = T_0(x)T_0(y) = 1 \\
&C_1(x,y) = T_1(x)T_0(y) = x \\
&C_2(x,y) = T_0(x)T_1(y) = y \\
&C_3(x,y) = T_2(x)T_0(y) = 2x^2 - 1 \\
&C_4(x,y) = T_1(x)T_1(y) = xy \\
&C_5(x,y) = T_0(x)T_2(y) = 2y^2 - 1 \\
&C_6(x,y) = T_3(x)T_0(y) = 4x^3 - 3x \\
&C_7(x,y) = T_2(x)T_1(y) = (2x^2 - 1)y \\
&C_8(x,y) = T_1(x)T_2(y) = (2y^2 - 1)x \\
&\ldots
\end{aligned} \quad . \tag{3.24}$$

The graphical representation of the first nine terms of 2D Chebyshev polynomials are shown in Figure 3.4.

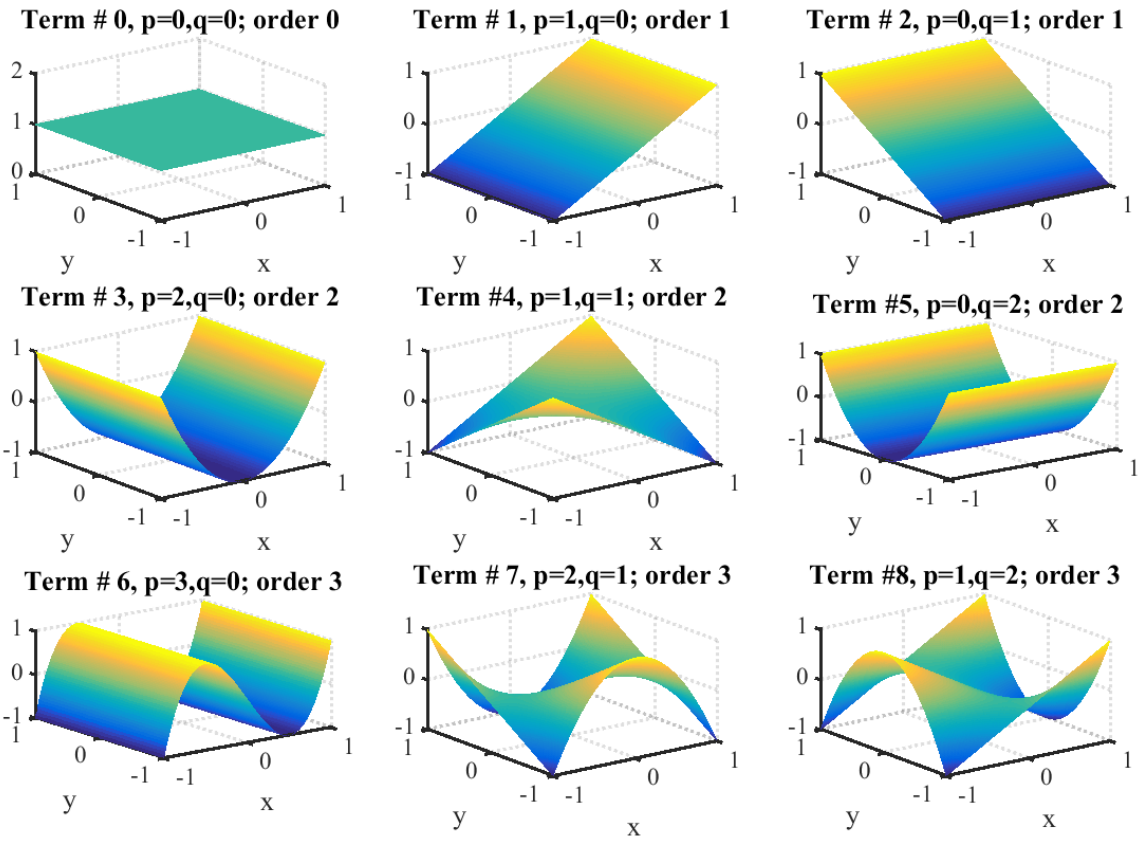

Figure 3.4: First nine terms of low order 2D Chebyshev polynomials.

The orthogonality of 2D Chebyshev polynomials are defined by the interval:

$$\int_{-1}^{1}\int_{-1}^{1}\frac{C_i(x,y)C_j(x,y)}{\sqrt{1-x^2}\sqrt{1-y^2}}dxdy=\begin{cases}0, i\neq j\\ K_2, i=j\end{cases}, \tag{3.25}$$

where the normalization constant for 2D Chebyshev polynomials K_2 is determined by the chosen values of *p* and *q* in Equation (3.23):

$$K_2=\begin{cases}\pi^2, p=q=0\\ \dfrac{\pi^2}{4}, p\neq 0 \text{ and } q\neq 0\\ \dfrac{\pi^2}{2}, \text{elsewhere}\end{cases}. \tag{3.26}$$

3.4.2 Approximation of a bivariate function by 2D Chebyshev series

The properties of using 1D Chebyshev series to approximate 1D non-periodic functions can be extended to its bivariate counterparts. The truncated 2D Chebyshev series $f_N(x, y)$, consistent with a one term index (i.e. n) in Equation (3.23), is used to approximate bivariate function $f(x, y)$:

$$f(x, y) \approx f_N(x, y) = \sum_{n=0}^{N} c_{2,n} C_n(x, y), \tag{3.27}$$

where each coefficient $c_{2,n}$ is calculated by:

$$c_{2,n} = \frac{1}{K_2} \int_{-1}^{1} \int_{-1}^{1} \frac{f(x, y) C_n(x, y)}{\sqrt{1-x^2}\sqrt{1-y^2}} dxdy. \tag{3.28}$$

3.4.3 Coefficients of 2D Chebyshev series and 2D power series

The relation between the coefficients of a bivariate function approximated by a 2D Chebyshev series, and 2D power series is also uniquely determined. For example, a surface defined on a square domain in the $-1 \le x \le 1$ and $-1 \le y \le 1$ directions with a height of z can be represented by:

$$z = G_{\mathrm{P}}(x, y), \tag{3.29}$$

where the subscript "P" represents the power series. The same function can also be represented by:

$$z = G_{\mathrm{C}}(x, y), \tag{3.30}$$

where the subscript "C" indicates the base function is 2D Chebyshev polynomials.

For instance, assuming a surface is given as:

$$G_{\mathrm{P}}(x, y) = a_{2,0} + a_{2,1}x + a_{2,2}y + a_{2,3}x^2 + a_{2,4}xy + a_{2,5}y^2, \tag{3.31}$$

where the six terms of 2D power base functions are linearly summed and weighted by six coefficients $a_{2,n}$ for $n = 0,1,2,...,5$.

$G_{\mathrm{P}}(x, y)$ represents a surface with highest order of two. The same surface can also be represented by a set of 2D Chebyshev base functions with six terms and weighted by six 2D Chebyshev coefficients $c_{2,n}$, for $n = 0,1,2,...,5$:

$$\begin{aligned} G_{\mathrm{C}}(x, y) &= c_{2,0}C_0(x, y) + c_{2,1}C_1(x, y) + c_{2,2}C_2(x, y) + c_{2,3}C_3(x, y) \\ &+ c_{2,4}C_4(x, y) + c_{2,5}C_5(x, y) \end{aligned} . \tag{3.32}$$

Setting $G_{\mathrm{P}}(x, y) = G_{\mathrm{C}}(x, y)$, the relation between the values of the 2D power coefficients in Equation (3.31) and the 2D Chebyshev coefficients in Equation (3.32) can be uniquely determined by the matrix equation:

$$\begin{bmatrix} c_{2,0} \\ c_{2,1} \\ c_{2,2} \\ c_{2,3} \\ c_{2,4} \\ c_{2,5} \end{bmatrix} = \begin{bmatrix} 1 & 0 & 0 & 1/2 & 0 & 1/2 \\ 0 & 1 & 0 & 0 & 0 & 0 \\ 0 & 0 & 1 & 0 & 0 & 0 \\ 0 & 0 & 0 & 1/2 & 0 & 0 \\ 0 & 0 & 0 & 0 & 1 & 0 \\ 0 & 0 & 0 & 0 & 0 & 1/2 \end{bmatrix} \begin{bmatrix} a_{2,0} \\ a_{2,1} \\ a_{2,2} \\ a_{2,3} \\ a_{2,4} \\ a_{2,5} \end{bmatrix}, \tag{3.33}$$

which can be written as:

$$\mathbf{C}_2 = \mathbf{M}_2\mathbf{A}_2, \tag{3.34}$$

where $\mathbf{C}_2$ is the vector of the first six 2D Chebyshev coefficients, $\mathbf{M}_2$ is the matrix mapping the 2D power coefficients to the 2D Chebyshev coefficients and $\mathbf{A}_2$ is the vector of the first six 2D power coefficients respectively.

Inversely, a set of 2D Chebyshev coefficients can be used to calculate the corresponding 2D power coefficients by matrix inversion:

$$\mathbf{A}_2 = (\mathbf{M}_2)^{-1}\mathbf{C}_2 . \tag{3.35}$$

This relationship described by Equation (3.32) and Equation (3.35) between the 2D power coefficients and 2D Chebyshev coefficients still holds when more terms of base functions are used.

CHAPTER 4 : FLANK GEOMETRY AND 2D CHEBYSHEV POLYNOMIALS

Besides the aforementioned properties of the Chebyshev polynomials (1D and 2D), another important reason of using the 2D Chebyshev polynomials as the base functions for approximating areal gear distance map is the geometric resemblance between the 2D Chebyshev polynomials and the form of the gear flank modifications and (or) deviation. In this chapter, a new set of areal parameters is introduced as an extension of the current line oriented parameters, listed in the current ISO standards [18]. The relationship between the areal modification (and/or deviation) parameters and the first six terms of 2D Chebyshev polynomials are illustrated graphically. Afterwards, detailed steps of calculating the areal gear parameters based on 2D Chebyshev coefficients are explained. Lastly, the analytic linkage between the first six 2D Chebyshev coefficients and the low order areal flank parameters are established.

4.1 Areal distance map of gear flank

The areal distance map is a collection of the values of individual plumb line distance of each measured point in a point cloud. Figure 4.1 (a) shows the measured gear flank represented by a measured point cloud in 3D space. The plumb line distances form an areal distance map as shown Figure 4.1 (b). To extract quantitative information from the areal distance map, Stoebener et al. [45] reported a method to calculate the areal gear parameters suggested in ISO based on least square method.

However, as explained in Section 2.4, without prior information such as nominal flank modification parameters, it is impossible to mathematically distinguish the sources that lead to the areal distance map in Figure 4.1 (b).

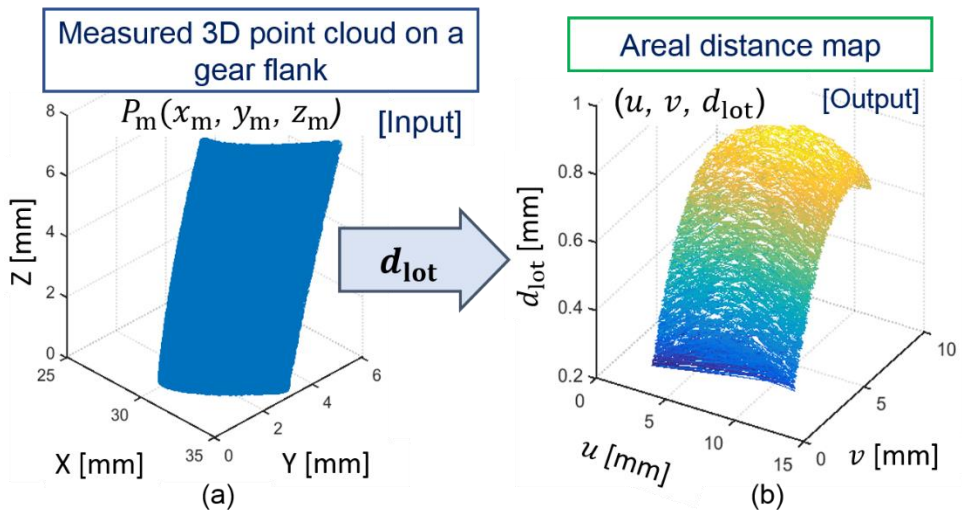

Figure 4.1: Cacluation of areal distance map: (a), raw measured point cloud on a flank; (b), obtained areal distance map, formed by the calculated plumb line distances from (a).

In the following section, a new set of areal gear parameters is defined to characterize:

- low order form information of individual flank, such as: slope, crowning, twist;
- relative location information from tooth to tooth: single pitch deviation, cumulative deviation.

4.2 Areal gear parameters

Conventional line oriented gear parameters are defined in standards such as [9]. To adapt area oriented evaluation methods, it is necessary to revise those parameters to areal ones, which retain the geometrical meanings of their conventional counterparts. This revision is analogous to the revision proposed by K. Stout [60], by changing conventional line oriented surface parameters to area oriented surface parameters in surface metrology.

Table 4.1 summarizes several conventional gear evaluation parameters and their revised areal gear parameters, which will be used for areal gear evaluation. Compared to the standardized conventional parameters, the revised areal parameters are indicated by the

superscript “A”, indicating the evaluation of those parameters is carried out on areal flank distance map.

Table 4.1: Conventional line oriented evaluation parameters [18] and proposed areal evaluation parameters.

Definition	Conventional parameter	Areal parameter
Intended profile slope modification	$C_{H\alpha}$	$C_{H\alpha}^{A}$
Profile slope deviation	$f_{H\alpha}$	$f_{H\alpha}^{A}$
Profile slope modification deviation	Not defined	$f_{CH\alpha}^{A}$
Intended profile crowning modification	C_{α}	C_{α}^{A}
Profile crowning modification deviation	Not defined	$f_{C\alpha}^{A}$
Helix slope modification	$C_{H\beta}$	$C_{H\beta}^{A}$
Helix slope deviation	$f_{H\beta}$	$f_{H\beta}^{A}$
Helix slope modification deviation	Not defined	$f_{CH\beta}^{A}$
Intended helix crowning modification	C_{β}	C_{β}^{A}
Helix crowning modification deviation	Not defined	$f_{C\beta}^{A}$
Profile form deviation	$f_{f\alpha}$	f_{f}^{A} areal form deviation
Helix form deviation	$f_{f\beta}$	
Total profile deviation	F_{α}	F_{f}^{A} total areal deviation
Total helix deviation	F_{β}	
Individual single pitch deviation	f_{pi}	f_{pi}^{A}
Individual cumulative pitch deviation	F_{pi}	F_{pi}^{A}

In addition, when a flank surface is measured by areal methods, it is unnecessary to characterize the form deviation of the whole surface by two types of form deviation, namely the profile form deviation $f_{f\alpha}$ and helix form deviation $f_{f\beta}$. Thus, a replacement parameter, defined as areal form deviation (denoted by f_f^A) is introduced to unify the areal form deviation. Similarly, this revision can be applied to unify the total profile deviation (F_α) and total helix deviation (F_β) by a new areal parameter, defined as total areal deviation (denoted by F_f^A). The areal individual single pitch deviation and the areal cumulative pitch deviation are also introduced at the end of Table 4.1, denoted by f_{pi}^A and F_{pi}^A, respectively.

4.2.1 Areal pitch deviations and zero order 2D Chebyshev polynomial

In a transverse plane, pitch is defined as the arc length between two virtual intersection points of the pitch circle with two consecutive right flanks (or right flanks). The nominal pitch can be calculated by different basic gear parameters, such as:

$$p_t = \frac{\pi m_n}{\cos\beta} = r\tau = \frac{2\pi r}{|z|}, \tag{4.1}$$

where p_t, r and τ are the transverse pitch, reference radius and the angular pitch respectively.

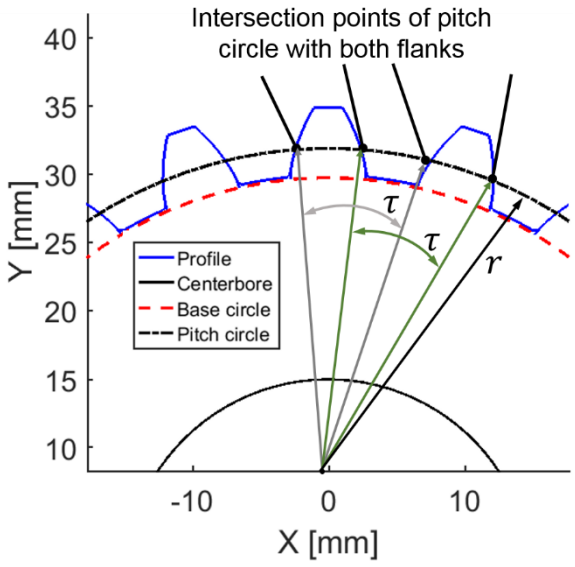

Figure 4.2: Schematic of the pitch circle (black dashed) and the pitch points on consecutive flanks (left and right) in transverse plane.

As pointed out in Section 2.4, a constant non-zero plumb line distance for an entire gear flank can be mathematically treated as a constant planar offset with respect to the pure involute flank. Geometrically, this constant offset plane is caused by a rotational offset with respect to the axis of gearing. The rotational offset has two applications: the first one is to use the offset as an alignment quantity for all teeth; the other one is to treat the calculated offset as angular pitch deviation, when the angular position of an arbitrary tooth is compared with respect to a reference tooth. Therefore, the areal cumulative pitch deviation of an arbitrary tooth can be established based on the latter application.

In Figure 4.3 (a), two nominal involute profiles (black solid curve) are shown, starting at different circumferential locations (i.e. different initial angles on the base circle). A 5 mm shift of the plumb line distance is converted to the angular offset and added to simulate the measured points (blue dot, connected by dashed curve). The calculated plumb line distance for the two sets of simulated measured points are shown in Figure 4.3 (b).

Clearly, the calculated plumb line distances for both sets of simulation are nearly 5 mm. As shown in the figure, the last digit of the calculation is to the machine precision (i.e. 5 $\pm 10^{-13}$).

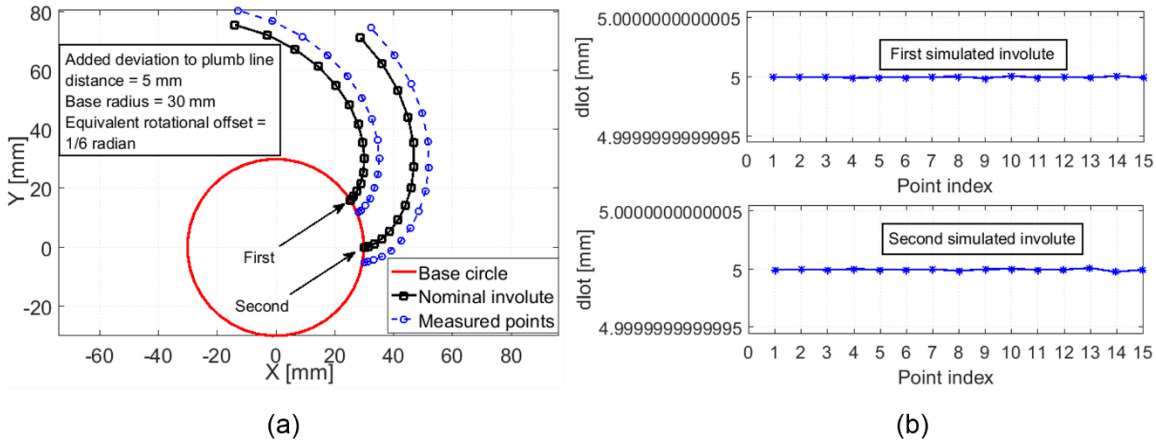

Figure 4.3: Angular offset and constant plumb line distance: (a), nominal and measured points of two involute profiles; (b), calculated plumb line distances for the two sets of simulated involute profiles.

Figure 4.4 depicts the geometrical similarity between the first term of 2D Chebyshev polynomial, $C_0(x, y)$ and the areal single pitch deviation of a flank in 3D space. The quantitative relationship of the areal single pitch deviation between the coefficients of 2D Chebyshev polynomials will be presented in the next section.

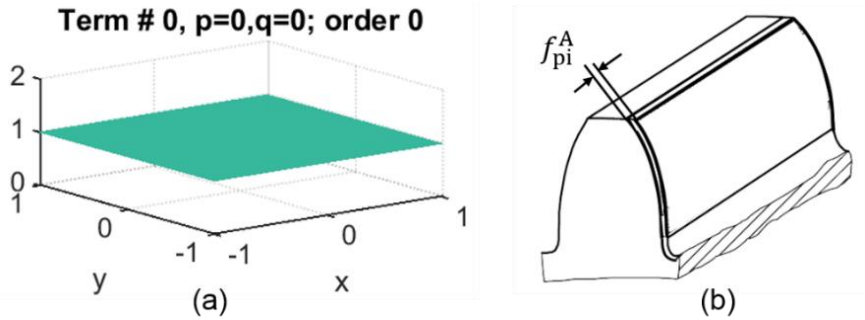

Figure 4.4: Geometric similarity between 2D Chebyshev polynomial and flank modification: (a), the 2D Chebyshev term #0; (b), 3D schematic of the individual cumulative pitch of a right flank, edited after [15].

4.2.2 Linkage between 2D Chebyshev terms and 1st order flank features

The 2D Chebyshev polynomial term #1, $C_1(x,y)$ defined on $[-1,1]^2$ is shown in Figure 4.5 (a) and the first order areal profile deviation and/or modification in a 3D solid model is given in Figure 4.5 (b). The 2D Chebyshev polynomial term # 2, $C_2(x,y)$ defined on $[-1,1]^2$ is shown in Figure 4.6 (a) and the first order areal helix deviation/modification in a 3D solid model is shown in Figure 4.6 (b). Because $C_1(x,y)$ and $C_2(x,y)$ are the only two first order 2D Chebyshev terms based on its definition, it is appropriate to use them to represent the first order flank deviation/modification on gear flanks.

The quantitative relationship between the amount of the areal gear parameters and the value of the corresponding 2D Chebyshev coefficients (i.e. A_1 and A_2) will be presented in next section.

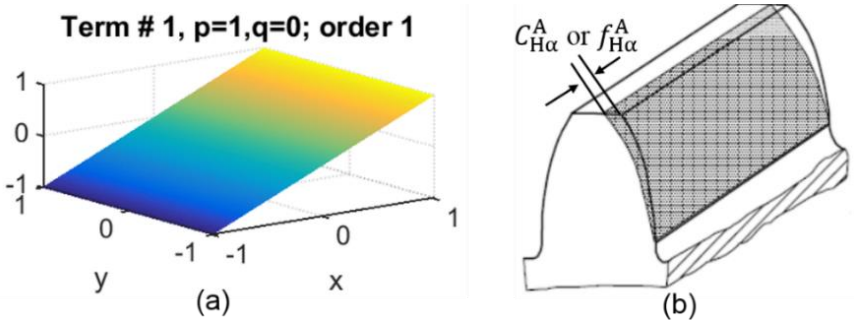

Figure 4.5: Geometric similarity between 2D Chebyshev polynomial and flank modification: (a), The 2D Chebyshev term #1; (b), 3D schematic of a modified flank with only profile slope modification, edited after [15].

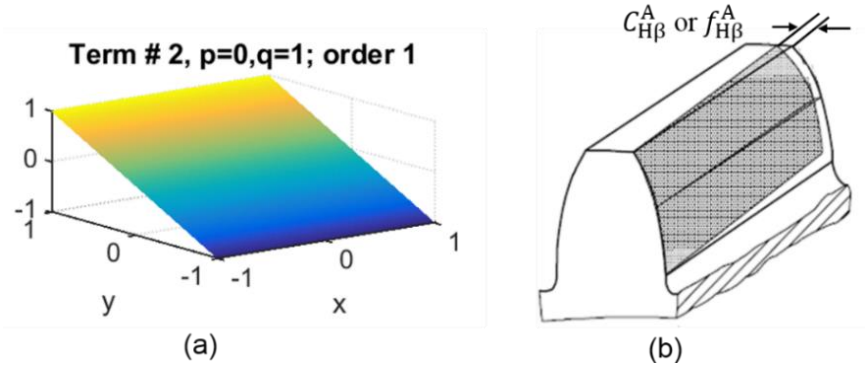

Figure 4.6: Geometric similarity between 2D Chebyshev polynomial and flank modification: (a), The 2D Chebyshev term #2; (b), 3D schematic of a modified flank with only helix slope modification , edited after [15].

4.2.3 Linkage between 2D Chebyshev terms and 2nd order flank features

The 2D Chebyshev polynomial term #3, $C_3(x, y)$ defined on $[-1,1]^2$ is shown in Figure 4.7 (a) and the second order areal profile deviation/modification in a 3D solid model is shown in Figure 4.7 (b).

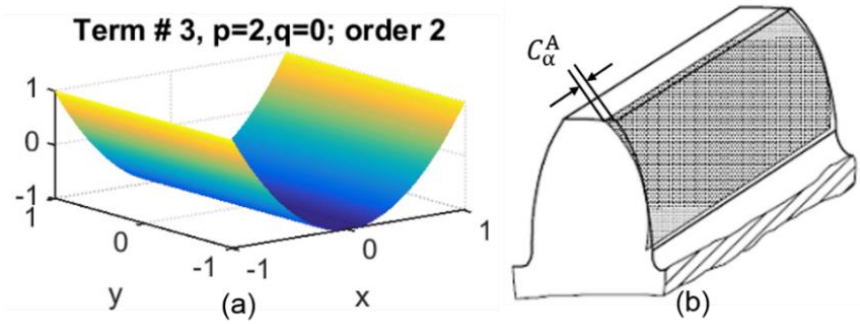

Figure 4.7: Geometric similarity between 2D Chebyshev polynomial and flank modification: (a), the 2D Chebyshev term #3; (b), 3D schematic of a modified flank with only profile crowning modification, edited after [15].

In addition, the geometric similarity of the 2D Chebyshev term $C_4(x, y)$ for areal flank twist, $C_5(x, y)$ for areal helix deviation/modification are shown in Figure 4.8 and

Figure 4.9 as well. The quantitative relationship between the amount of the areal gear parameters and the value of the corresponding 2D Chebyshev coefficients will be presented in the next section.

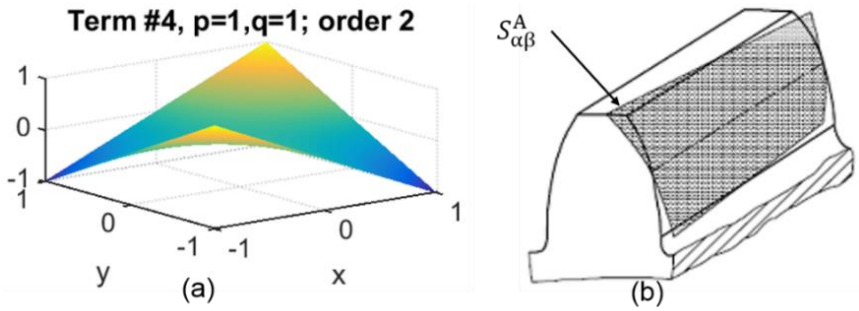

Figure 4.8: Geometric similarity between 2D Chebyshev polynomial and flank modification: (a), The 2D Chebyshev term #4; (b), 3D schematic of a modified flank with flank twist, edited after [15].

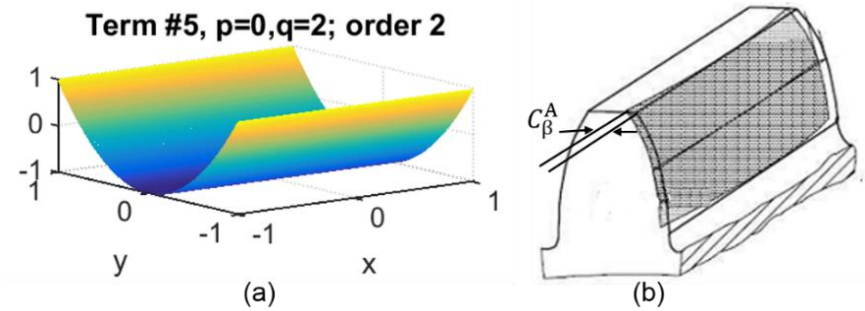

Figure 4.9: Geometric similarity between 2D Chebyshev polynomial and flank modification: (a), The 2D Chebyshev term #5; (b) 3D schematic of a modified flank with only helix crowning modification, edited after [15].

4.3 Orthogonal decomposition of areal distance map

Cylindrical flank modifications have several properties intrinsic to the way they are defined. Modifications are superimposed on the pure involute surface in the surface normal direction and are independently specified on a flank. Hereby, an areal distance map containing all modifications and/or deviations can be mathematically decomposed into

different surface components represented by different 2D Chebyshev terms. This ideal is graphically depicted in Figure 4.10.

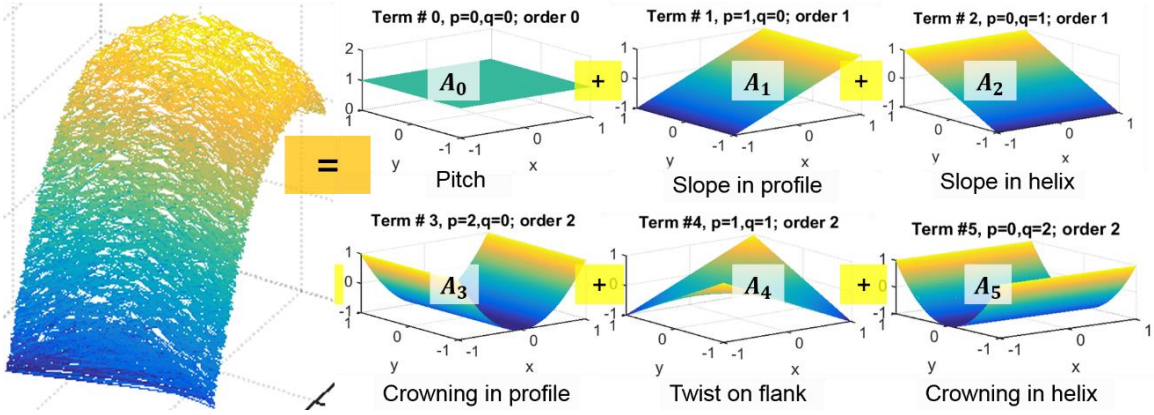

Figure 4.10: Decomposition areal distance map into the first six 2D Chebyshev terms.

4.3.1 Analytic description of flank modifications

The slope and crowning modifications of a flank $M_{\mathrm{nom}}^{\mathrm{A}}(u,v)$ can be collectively expressed based on Equation (2.10) and (2.11):

$$M_{\mathrm{nom}}^{\mathrm{A}}(u,v) = A(u) + B(v) = -\frac{4C_{\alpha}^{\mathrm{A}}}{L_{\alpha}^{2}}u^{2} + \frac{4C_{\alpha}^{\mathrm{A}} + C_{\mathrm{H}\alpha}^{\mathrm{A}}}{L_{\alpha}}u - \frac{4C_{\beta}^{\mathrm{A}}}{L_{\beta}^{2}}v^{2} + \frac{4C_{\beta}^{\mathrm{A}} + C_{\mathrm{H}\beta}^{\mathrm{A}}}{L_{\beta}}v\,. \quad (4.2)$$

The areal flank twist can be described by introducing a new parameter $S_{\alpha\beta}^{\mathrm{A}}$ [61]. $S_{\alpha\beta}^{\mathrm{A}}$ appears in the coefficients of a bivariate function $T^{\mathrm{A}}(u,v)$, which is defined on the evaluation zone $[0,L_{\alpha}]\times[0,L_{\beta}]$:

$$T^{\mathrm{A}}(u,v) = -\frac{S_{\alpha\beta}^{\mathrm{A}}}{L_{\alpha}L_{\beta}}uv + \frac{S_{\alpha\beta}^{\mathrm{A}}}{2L_{\alpha}}u + \frac{S_{\alpha\beta}^{\mathrm{A}}}{2L_{\beta}}v\,, \quad (4.3)$$

such that the characteristic form of areal twist at four boundaries are:

$$\begin{cases} T^{\mathrm{A}}(u,0) = \dfrac{S^{\mathrm{A}}_{\alpha\beta}}{2L_{\alpha}} u \\ T^{\mathrm{A}}(0,v) = \dfrac{S^{\mathrm{A}}_{\alpha\beta}}{2L_{\beta}} v \\ T^{\mathrm{A}}(u,L_{\beta}) = -\dfrac{S^{\mathrm{A}}_{\alpha\beta}}{2L_{\alpha}} (u - L_{\alpha}) \\ T^{\mathrm{A}}(L_{\alpha},v) = -\dfrac{S^{\mathrm{A}}_{\alpha\beta}}{2L_{\beta}} (u - L_{\beta}) \end{cases} . \tag{4.4}$$

Combining Equation (4.2) and Equation (4.3), the low order form modification/deviation of a gear flank can be expressed as:

$$M^{\mathrm{A}}(u,v) = M^{\mathrm{A}}_{\mathrm{nom}}(u,v) + T^{\mathrm{A}}(u,v) . \tag{4.5}$$

$M^{\mathrm{A}}(u,v)$ can be expressed by the 2D power series $D_{\mathrm{P}}(u,v)$ defined on the domain of $u \in [0, L_{\alpha}]$ and $v \in [0, L_{\beta}]$:

$$M^{\mathrm{A}}(u,v) = D_{\mathrm{P}}(u,v) = p_0 + p_1 u + p_2 v + p_3 u^2 + p_4 uv + p_5 v^2 + H(u,v) , \tag{4.6}$$

where $p_0, p_1, ..., p_5$ are the first six coefficients and $H(u,v)$ denotes terms that have order higher than two. Derivation in the following section shows that, the first six coefficients of $D_{\mathrm{P}}(u,v)$ can be calculated by the 2D Chebyshev coefficients after mapping $D_{\mathrm{P}}(u,v)$ into $D_{\mathrm{P}}(u',v')$ in which $(u',v') \in [-1,1]^2$.

4.3.2 Conversion from evaluation zone to square zone

The decomposition of the measured point cloud into a 2D Chebyshev series requires a mapping of the surface coordinates (u,v), determined by the boundary of the evaluation range in the profile and helix direction ($[u_{\mathrm{s}}, u_{\mathrm{e}}] \times [v_{\mathrm{s}}, v_{\mathrm{e}}]$), to square coordinates (u',v'), which are the coordinates defined on the domain $[-1,1]^2$ as shown in Figure 4.11.

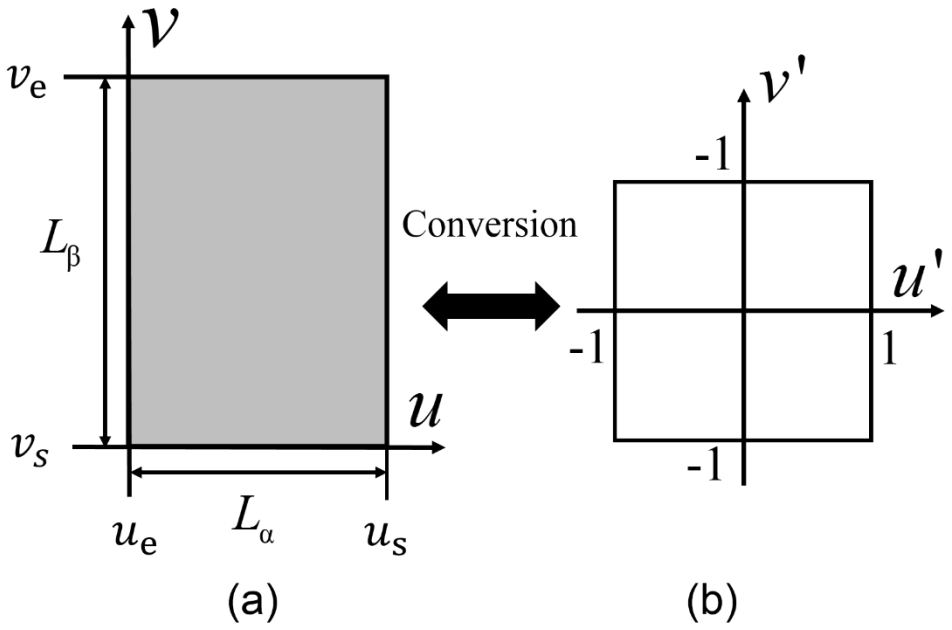

Figure 4.11: Converting from evaluation range domain: (a) areal flank evaluation range; (b) square domain for calculating the 2D Chebyshev coefficients.

The conversion between surface coordinates to the square coordinates can be modeled as a linear mapping:

$$\begin{cases} u' = \dfrac{2u - u_e - u_s}{u_e - u_s} \\ v' = \dfrac{2v - v_e - v_s}{v_e - v_s} \end{cases}, \tag{4.7}$$

and conversely:

$$\begin{cases} u = \dfrac{u_e - u_s}{2} u' + \dfrac{u_e + u_s}{2} \\ v = \dfrac{v_e - v_s}{2} v' + \dfrac{v_e + v_s}{2} \end{cases}. \tag{4.8}$$

For a full flank, the start and end values for profile and helix direction are set to:

$$\begin{cases} u_s = 0 \\ u_e = L_\alpha \end{cases} \text{and} \begin{cases} v_s = 0 \\ v_e = L_\beta \end{cases}, \tag{4.9}$$

such that the conversion relation in Equation (4.7) and Equation (4.8) are simplified to:

$$\begin{cases} u' = \dfrac{2}{L_\alpha} u - 1 \\ v' = \dfrac{2}{L_\beta} v - 1 \end{cases}, \tag{4.10}$$

and reversely,

$$\begin{cases} u = \dfrac{L_\alpha}{2} u' + \dfrac{L_\alpha}{2} \\ v = \dfrac{L_\beta}{2} v' + \dfrac{L_\beta}{2} \end{cases}. \tag{4.11}$$

4.3.3 Calculation of 2D Chebyshev coefficients

After the conversion, the 2D Chebyshev series is defined on (u', v') and truncated at order *N* to approximate the 2D distance map $D(u', v')$ on the square domain $[-1,1]^2$:

$$D(u', v') = \sum_{n=0}^{N} A_n C_n(u', v'), \tag{4.12}$$

where the coefficients A_n for each term $C_n(u', v')$ can be evaluated by the double integral:

$$A_n = \frac{1}{K_2} \int_{-1}^{1} \int_{-1}^{1} \frac{D'(u', v') C_n(u', v')}{\sqrt{1-(u')^2}\sqrt{1-(v')^2}} du' dv'. \tag{4.13}$$

In the following chapters, the first six terms (*n* = 0, 1, 2, …, 5) of 2D Chebyshev polynomials are used for approximating the areal distance map.

After converting the areal distance map from the areal evaluation domain to the squared domain $[-1,1]^2$, an interim bivariate function $D_{\mathrm{p}}(u', v')$ is introduced in the form of a power polynomial on the square domain $[-1,1]^2$ as:

$$D_{\mathrm{p}}(u', v') = a_0' + a_1' u' + a_2' v' + a_3' (u')^2 + a_4' u' v' + a_5' (v')^2. \tag{4.14}$$

By comparing the coefficients in Equation (4.12) and Equation (4.14), the relationship between the interim coefficients ($a_0', a_1', ..., a_5'$) and the first six 2D Chebyshev coefficients ($A_0, A_1, ..., A_5$) is established as:

$$\begin{cases} a_0' = A_0 - A_3 - A_5 \\ a_1' = A_1 \\ a_2' = A_2 \\ a_3' = 2A_3 \\ a_4' = A_4 \\ a_5' = 2A_5 \end{cases} . \tag{4.15}$$

Table 4.2 summarizes the relationship between the areal gear feature and the first six 2D Chebyshev terms and the corresponding 2D Chebyshev coefficients.

Table 4.2: First six low order 2D Chebyshev terms and areal gear features.

Term	Order	Coefficient	Analytic expression	Influenced areal gear features
$C_0(u',v')$	0	A_0	1	Pitch
$C_1(u',v')$	1	A_1	u'	Profile slope
$C_2(u',v')$	1	A_2	v'	Helix slope
$C_3(u',v')$	2	A_3	$2(u')^2 - 1$	Profile crowning, pitch
$C_4(u',v')$	2	A_4	$u'v'$	Flank twist
$C_5(u',v')$	2	A_5	$2(v')^2 - 1$	Helix crowning, pitch

4.3.4 Converting 2D Chebyshev coefficients to areal gear parameters

Substituting Equation (4.11) into Equation (4.6) and comparing the coefficients in Equation (4.6) and Equation (4.14) leads to the relationship between the two sets of coefficients of power series in two different domains:

$$\begin{cases} p_0 = a_0^{'} - a_1^{'} - a_2^{'} + a_3^{'} + a_4^{'} + a_5^{'} \\ p_1 = \dfrac{2}{L_\alpha} a_1^{'} - \dfrac{4}{L_\alpha} a_3^{'} - \dfrac{2}{L_\alpha} a_4^{'} \\ p_2 = \dfrac{2}{L_\beta} a_2^{'} - \dfrac{2}{L_\beta} a_4^{'} - \dfrac{4}{L_\beta} a_5^{'} \\ p_3 = \dfrac{4}{L_\alpha^2} a_3^{'} \\ p_4 = \dfrac{4}{L_\alpha L_\beta} a_4^{'} \\ p_5 = \dfrac{4}{L_\beta^2} a_5^{'} \end{cases} . \tag{4.16}$$

Afterwards, substituting the interim coefficients $a_n^{'}(n = 0,1,2,...,5)$ in Equation (4.15) into the power coefficients p_n $(n = 0,1,2,...,5)$ in Equation (4.16), the relationship between the first six 2D Chebyshev coefficients $A_n(n = 0,1,2,...,5)$ and the areal flank modification (and/or deviation) can be established as:

$$\begin{cases} C_{\mathrm{H}\alpha}^{\mathrm{A}} = L_\alpha p_1 + L_\alpha^2 p_3 + \dfrac{L_\alpha L_\beta}{2} p_4 = 2a_1^{'} = 2A_1 \\ C_{\mathrm{H}\beta}^{\mathrm{A}} = L_\beta p_2 + L_\beta^2 p_5 + \dfrac{L_\alpha L_\beta}{2} p_4 = 2a_2^{'} = 2A_2 \\ C_\alpha^{\mathrm{A}} = -\dfrac{L_\alpha^2}{4} p_3 = -a_3^{'} = -2A_3 \\ S_{\alpha\beta}^{\mathrm{A}} = -L_\alpha L_\beta p_4 = -4a_4^{'} = -4A_4 \\ C_\beta^{\mathrm{A}} = -\dfrac{L_\beta^2}{4} p_5 = -a_5^{'} = -2A_5 \end{cases} , \tag{4.17}$$

which can be written in a matrix form:

$$\begin{bmatrix} C_{\mathrm{H}\alpha}^{\mathrm{A}} \\ C_{\mathrm{H}\beta}^{\mathrm{A}} \\ C_{\alpha}^{\mathrm{A}} \\ S_{\alpha\beta}^{\mathrm{A}} \\ C_{\beta}^{\mathrm{A}} \end{bmatrix} = \begin{pmatrix} 2 & 0 & 0 & 0 & 0 \\ 0 & 2 & 0 & 0 & 0 \\ 0 & 0 & -2 & 0 & 0 \\ 0 & 0 & 0 & -4 & 0 \\ 0 & 0 & 0 & 0 & -2 \end{pmatrix} \begin{bmatrix} A_1 \\ A_2 \\ A_3 \\ A_4 \\ A_5 \end{bmatrix}. \tag{4.18}$$

The above derivations encapsulate the essential advantage of using the first six 2D Chebyshev coefficients to completely and uniquely describe the areal form information of a gear flank from its areal distance map.

The areal gear parameters on the left side of Equation (4.18) are defined on the domain formed by the gear evaluation range $[0, L_\alpha] \times [0, L_\beta]$; on the right side, the corresponding 2D Chebyshev coefficients are obtained in the domain $[-1,1]^2$.

In addition, the coefficients for the zero order component in Equation (4.16) can be calculated by the 2D Chebyshev coefficients as:

$$p_0 = a_0' - a_1' - a_2' + a_3' + a_4' + a_5' = A_0 - A_1 - A_2 + A_3 + A_4 + A_5. \tag{4.19}$$

which can be converted to the areal single pitch deviation $f_{\mathrm{pi}}^{\mathrm{A}}$ by:

$$f_{\mathrm{pi}}^{\mathrm{A}} = \frac{d_{\mathrm{M}} \sqrt{1 + (\cos\alpha_{\mathrm{t}} \tan\beta)^2}}{2 r_{\mathrm{b}}} \left(A_0 - A_1 - A_2 + A_3 + A_4 + A_5 \right), \tag{4.20}$$

where d_{M} is the measurement diameter for conventional pitch deviation. This equation can be directly used to compare the conventional point-oriented pitch evaluation and the areal pitch evaluation for three reasons:

- first, the conventional pitch deviation (f_{pi}) is measured on a certain diameter (i.e. d_{M});

- secondly, the conventional pitch deviation is usually expressed in the unit of arclength on the measured diameter;
- lastly, the conventional pitch deviation is given on a transverse plane for helical gears.

Obviously, the areal single pitch deviation is a linear combination of the first six 2D Chebyshev coefficients when the first six 2D Chebyshev terms are used for reconstructing the areal distance map. For a gear without any flank deviation/modification, the areal single pitch deviation is determined by the constant value A_0.

The relationship between different types of coefficients mentioned above and the low order areal flank modification are depicted Figure 4.12, which represents the internal mathematical links of the proposed 2D Chebyshev method.

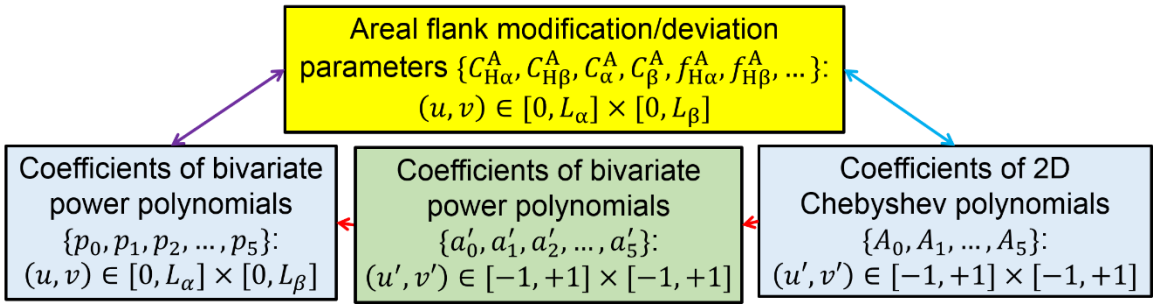

Figure 4.12: Relationship between the coefficients of bivariate power polynomials, 2D Chebyshev polynomials and the flank modification and deviation.

4.3.5 Numerical verification on a simulated flank

Figure 4.13 shows the simulated modifications in profile and helix directions as well as the simulated "noise" across the entire flank, on a matrix with grid size of 128 by 128. The relative error is defined as the difference between the approximated value of a parameter to its nominal value, divided by the nominal value.

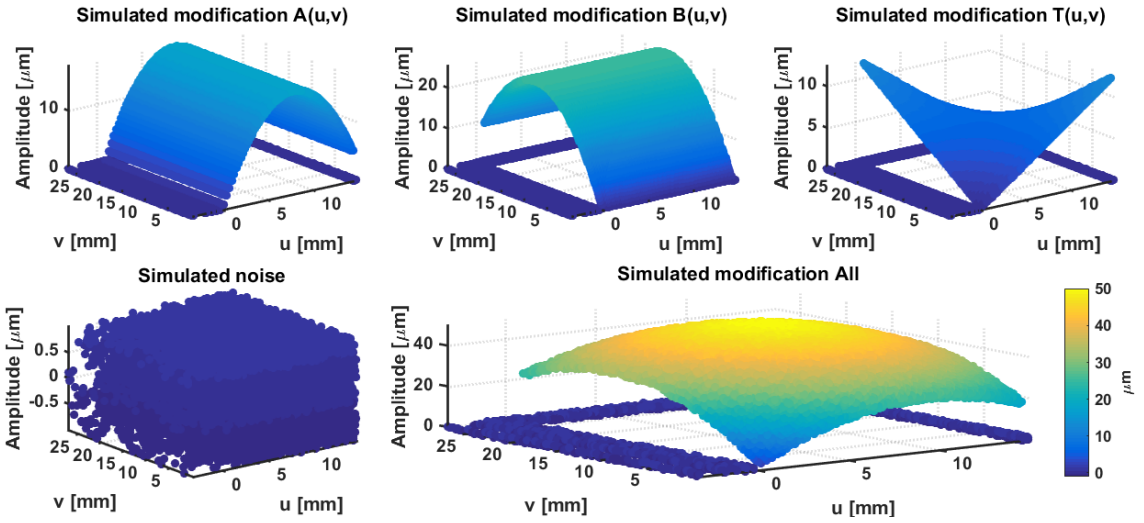

Figure 4.13: Simulated gear flank with profile slope modification, profile crowning modification, helix slope modification, helix crowing modification, twist and pointwise deviation.

Table 4.3 shows the simulated values of each modifications and their approximated values. A grid size of 128 by 128 is used for simulating an areal flank by five modifications. A deviation with amplitude of ±1 μm (uniform distribution) is added to the simulated flank in a pointwise manner in the sense of "noise".

The relative error is defined as:

$$R.E. = \frac{C_{\text{app}} - C_{\text{sim}}}{C_{\text{sim}}} \times 100\% , \tag{4.21}$$

where C_{app} and C_{sim} represent the approximated values and the simulated values for the five types of flank modifications in the third and fourth columns in Table 4.3.

More detailed investigation of the influential factors such as point density on the flank, numerical algorithm and spatial distribution of points on the flank will be investigated in the next chapter.

Table 4.3: Simulated nominal and approximated areal flank parameters.

Type of modification	Symbol	Simulated value [μm]	Approximated value [μm]	Relative Error (%)
Profile slope	$C_{H\alpha}^{A}$	5	5.042	0.84
Helix slope	C_{α}^{A}	10	9.963	-0.37
Profile crowning	$C_{H\beta}^{A}$	15	15.006	0.04
Flank twist	$S_{\alpha\beta}^{A}$	25	24.934	-0.26
Helix crowning	C_{β}^{A}	20	19.932	-0.34

4.4 High order 2D Chebyshev polynomials and balancing terms

In the earlier chapters, the first six terms (term #0 to #5) are used for reconstructing the areal distance map, and the corresponding 2D Chebyshev coefficients are used to calculate the areal flank parameters. However, higher order terms of 2D Chebyshev polynomials as listed in Table 4.4 can also have low order components known as the "balancing terms". Suppose that higher order 2D Chebyshev terms are used during the orthogonal decomposition of an areal distance map and the non-zero higher order 2D Chebyshev coefficients are used for reconstructing the approximated areal map, then the balancing terms will collectively contribute to the low order gear parameters.

For example, the $C_6(u',v') = 4(u')^3 - 3u'$ term has a balancing term of $-3u'$. Thus, if the C_6 term is included in the 2D Chebyshev series, then the coefficient A_6 will backwardly contribute the first order information represented by u' weighted by a factor of -3. Because no Chebyshev terms higher than C_5 are used during the decomposition, all remaining surface components between the reconstructed areal map and the input areal map is treated as a residual map.

Another reason not to apply higher order 2D Chebyshev polynomials to approximate higher order, periodic surface components on a gear flank is that there is neither a directly geometric nor an analytic connection between those components with the higher order 2D Chebyshev polynomials.

Alternatively, after removing the low order form components from the areal distance map, it is possible to apply analysis techniques in surface metrology [62] to assess the spatial frequency components on the gear flank.

Table 4.4: Higher order 2D Chebyshev terms and balancing terms n = 6,7,8,…,15.

Term	Order	Coefficient	Expression	Influenced areal gear parameters
C_6	3	A_6	$4(u')^3-3u'$	Profile slope
C_7	3	A_7	$2(u')^2v'-v'$	Helix slope
C_8	3	A_8	$2(v')^2u'-u'$	Profile slope
C_9	3	A_9	$4(v')^3-3v'$	Helix slope
C_{10}	4	A_{10}	$8(u')^4-8(u')^2+1$	Profile crowning, pitch
C_{11}	4	A_{11}	$4(u')^3-3u'v'$	Twist
C_{12}	4	A_{12}	$4(u'v')^4-2(u')^2-2(v')^2+1$	Profile and helix crowning, pitch
C_{13}	4	A_{13}	$4(v')^3u'-3u'v'$	Twist
C_{14}	4	A_{14}	$8(v')^4-8(v')^2+1$	Helix crowning, pitch
C_{15}	5	A_{15}	$16(u')^5-20(u')^3+5u'$	Profile slope
…	…	…	…	…

CHAPTER 5 : COMPUTATION OF 2D CHEBYSHEV COEFFICIENTS

Based on the fact that the 2D Chebyshev coefficients can be used to obtain low order modifications/deviations of a gear flank, it is important to study the calculation process of 2D Chebyshev coefficients. Firstly, the 2D Chebyshev coefficients are directly related to the measurands, namely the proposed areal gear parameters. Secondly, various factors could influence the results of evaluating the double integral of the 2D Chebyshev coefficients in a discretized dataset, as given by Equation (4.13).

From a computational perspective, this chapter first investigates several numerical factors that influence the values of coefficients evaluated by numerical integration, such as:

- grid size,
- choice of algorithm for numerical integration, and
- interpolation methods.

In addition, task specific issues in areal gear metrology are investigated, for example:

- spatial distribution of point clouds on a cylindrical gear flank,
- post-sampling strategy on areal distance map, and
- influence of misalignment of the nominal gear coordinate system (CSY) with respect to a simulated CSY.

5.1 Evaluation of double integral on discrete dataset

Three different algorithms for calculating 2D Chebyshev coefficient from a discrete set of data are used in this chapter. The investigation is focused on Equation (4.13).

5.1.1 2D Empirical edge method

The upper and lower integration limits (i.e. ±1) impose a numerical singularity for the evaluation of the double integral in the denominator of Equation (4.13).

An empirical edge method is proposed to replace the original integral limits by a pair of numbers, denoted by $\varepsilon_{u'}$ and $\varepsilon_{v'}$ for the u' and v' variables, respectively. Thus, Equation (4.13) evolves to:

$$A_n = \frac{1}{K_2}\int_{-\varepsilon_{u'}}^{\varepsilon_{u'}}\int_{-\varepsilon_{v'}}^{\varepsilon_{v'}} \frac{D'(u',v')C_n(u',v')}{\sqrt{1-(u')^2}\sqrt{1-(v')^2}}du'dv'. \tag{5.1}$$

The value of the empirical edge is determined by the following empirical equation:

$$\varepsilon_{u'} = \varepsilon_{v'} = 1 - \frac{1}{5\sqrt{N_{\text{data}}}}, \tag{5.2}$$

where N_{data} is the number of points within an areal distance map.

5.1.2 2D Cosine variable method

The singularity issue can also be eliminated by replacing the variable *x* and *y* in the original double integral with a pair of angular variables θ_{x} and θ_{y}, which are defined as:

$$\begin{cases} x = \cos\theta_{\text{x}} \\ y = \sin\theta_{\text{y}} \end{cases}, \tag{5.3}$$

such that:

$$
\begin{aligned}
c_{2,n} &= \frac{1}{K_2}\int_{-1}^{1}\int_{-1}^{1}\frac{f(x,y)\cdot C_n(x,y)}{\sqrt{1-x^2}\sqrt{1-y^2}}dxdy \\
&= \frac{1}{K_2}\int_{0}^{\pi}\int_{0}^{\pi}\frac{f(\cos\theta_x,\cos\theta_y)\cdot C_n(\cos\theta_x,\cos\theta_y)}{\sqrt{1-\cos^2\theta_x}\sqrt{1-\cos^2\theta_y}}d\cos\theta_x d\cos\theta_y \\
&= \frac{1}{K_2}\int_{0}^{\pi}\int_{0}^{\pi}\frac{f(\cos\theta_x,\cos\theta_y)\cdot C_n(\cos\theta_x,\cos\theta_y)}{\sin\theta_x\sin\theta_y}\sin\theta_x\sin\theta d\theta_x d\theta_y \\
&= \frac{1}{K_2}\int_{0}^{\pi}\int_{0}^{\pi} f(\cos\theta_x,\cos\theta_y)\cdot\cos p\theta_x\cdot\cos q\theta_y d\theta_x d\theta_y
\end{aligned}
\quad . \tag{5.4}
$$

Clearly, no empirical edge is needed for evaluating this form of double integral, thus Equation (4.13) is replaced by:

$$
A_n = \frac{1}{K_2}\int_{0}^{\pi}\int_{0}^{\pi} f(\cos\theta_{u'},\cos\theta_{v'})\cdot\cos p\theta_{u'}\cdot\cos q\theta_{v'}d\theta_{u'}d\theta_{v'}, \tag{5.5}
$$

in which,

$$
\begin{cases}
\theta_{u'} = \arccos(u') \\
\theta_{v'} = \arccos(v')
\end{cases} \tag{5.6}
$$

are the angular variables after mapping *u* and *v* to *u'* and to *v'*, respectively.

5.1.3 Delaunay Triangulation and numerical integration

In calculus, a double integral can be treated as the calculation of the volume under a surface (i.e. integer function) over its definition region in the plane (i.e. integral area). The numerical calculation of Equation (5.1) and Equation (5.5) can be implemented by trapezoidal method for gridded data in MATLAB® [63] . However, in practice, raw point clouds are usually non-collinear, imposing an issue of using trapezoidal algorithms. This type of data is known as scattered data. Scattered measured point clouds are usually stored in a matrix, which has three columns (representing the coordinates for X, Y and Z axes)

and numerous rows (point index). The order of each element in the matrix does not represent the order of collection during data acquisition.

To implement the double integral, a preprocessing of the scatted data is needed, which is known as triangulation in the field of computational geometry. Depending on the triangulation criterion, various types of triangulations can be built upon a given set of scattered data. Figure 5.1 illustrates a triangulation of six points (black dots, labeled by P_1 to P_6). The grey dots are the projected points, whose (u', v') coordinates are the same as those of P_1 to P_6. This triangulation generates four pentahedrons, whose bases are formed by the projected points. Because the base triangles of each pentahedron are coplanar, the area of each triangle can be directly calculated by the coordinates of its vertices (u', v'). The height of each pentahedron (marked by yellow dots) is approximated by averaging the values of each vertex of those points that form the triangles of the pentahedron.

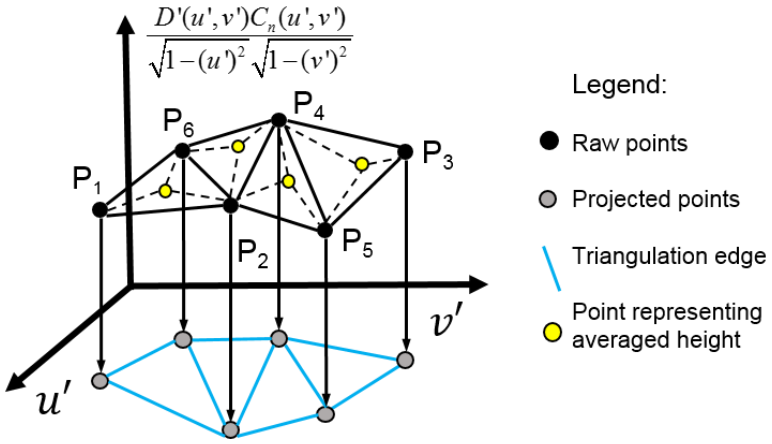

Figure 5.1: Illustration of a 2D triangulation of six spatial points in u'-v' plane for the cacluation of the volume of hexahedron.

The most commonly used triangulation technique is the Delaunay Triangulation, which maximizes the smallest interior angles between two edges of a triangle [64]. A

MATLAB® function "delaunayTriangluation(x,y)" can be used to create a Delaunay Triangulation on a 2D dataset. It is used as the default tool for the numerical integration of Equation (5.1) and Equation (5.5) to calculate the 2D Chebyshev coefficients of a scattered dataset for the first two methods described in Section 5.1.1 and Section 5.1.2.

5.1.4 2D Discrete cosine transform method

The third method to get the 2D Chebyshev coefficients is based on the 2D discrete cosine transform (2D DCT). DCT has been widely applied in the image processing field for image compression due to its strong "energy compaction" properties [65].

For an arbitrary two-dimensional matrix (e.g. M columns and N rows), the 2D discrete cosine transform, denoted by $F_{\text{dct2}}(p,q)$ is:

$$F_{\text{dct2}}(p,q) = \alpha_p \alpha_q \sum_{m=0}^{M-1} \sum_{n=0}^{N-1} f(m,n) \cos\frac{\pi(2m+1)p}{2M} \cos\frac{\pi(2n+1)q}{2N}, \tag{5.7}$$

where

$$\alpha_p = \begin{cases} 1/\sqrt{M}, p = 0 \\ \sqrt{2/M}, 1 \le p \le M-1 \end{cases} \tag{5.8}$$

and

$$\alpha_q = \begin{cases} 1/\sqrt{N}, q = 0 \\ \sqrt{2/N}, 1 \le q \le M-1 \end{cases} \tag{5.9}$$

are the two scaling factors corresponding to the indices p and q (see Equation (5.5)), respectively.

Converting the continuous form of the double integral in Equation (5.5) to a discrete form, the 2D Chebyshev coefficients can be calculated by:

$$A_n = \frac{1}{K_2}\sum_{m=0}^{M-1}\sum_{n=0}^{N-1}\{ f[\theta_{u'}(m),\theta_{v'}(n)]\cdot[\cos p\theta_{u'}(m)\cdot\cos q\theta_{v'}(n)]\cdot\Delta\theta_{u'}\cdot\Delta\theta_{v'}\}, \quad (5.10)$$

where m and n are the index number for M and N discretized values of $\theta_{u'}$ and $\theta_{v'}$, respectively. Equation (5.10) is the discrete form of Equation (5.7). The implementation of 2D DCT in MATLAB can be realized by the built in function "dct2"[66].

In order to apply the 2D DCT function, two more steps are needed, the first one is to interpolate a function out of the scattered data; the second one is to generate a 2D grid based on 2D Chebyshev points for sampling the interpolated function.

As shown in Figure 5.2 (a), six Chebyshev points are generated in both X and Y axes for sampling the function of interest. Using the same scattered data in Section 3.4.3, the sampled points after interpolation are displayed in Figure 5.2 (b), together with the original scattered data.

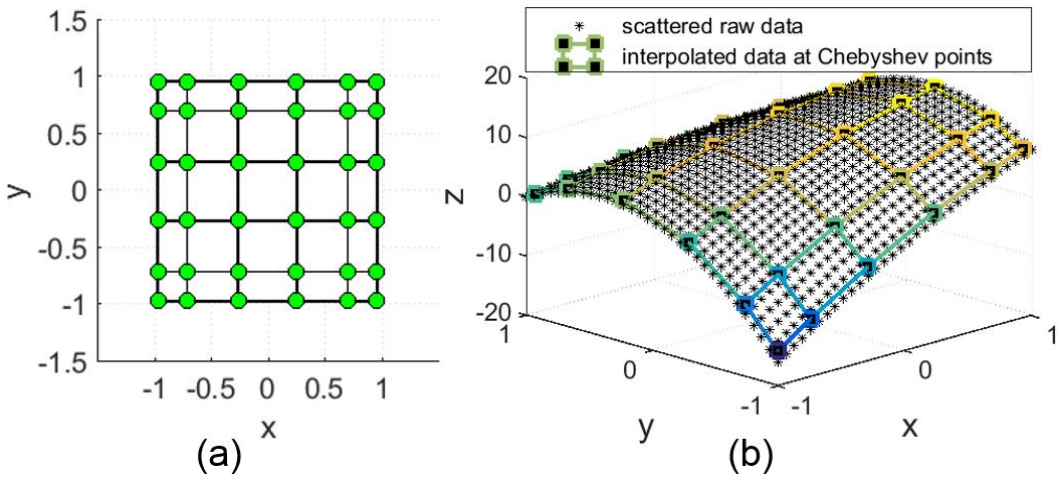

Figure 5.2: Illustration of the calculation of 2D DCT at Chebyshev points: (a), location of 2D Chebyshev points in x and y axes; (b), interpolated surface and sampled data on 2D Chebyshev points.

Comparing the right sides of both equations, the relationship between the first six 2D Chebyshev coefficients and the values of transformed matrix $F_{\text{dct2}}(p,q)$ are given by:

$$\begin{aligned} A_0 &= \frac{1}{\sqrt{M}\sqrt{N}} F_{\text{dct2}}(1,1), \quad A_1 = \frac{\sqrt{2}}{\sqrt{M}\sqrt{N}} F_{\text{dct2}}(2,1), \\ A_2 &= \frac{\sqrt{2}}{\sqrt{M}\sqrt{N}} F_{\text{dct2}}(1,2), \quad A_3 = \frac{\sqrt{2}}{\sqrt{M}\sqrt{N}} F_{\text{dct2}}(3,1), \quad . \\ A_4 &= \frac{2}{\sqrt{M}\sqrt{N}} F_{\text{dct2}}(2,2), \quad A_5 = \frac{\sqrt{2}}{\sqrt{M}\sqrt{N}} F_{\text{dct2}}(1,3). \end{aligned} \tag{5.11}$$

Obviously, a three by three interpolation grid is enough to output the first six matrix entities in F_{dct2}. The number of Chebyshev points in one axis is selected to be six for 2D DCT calculation.

5.2 Distributions of nominal points on flank

Non-uniform spacing and distribution of measured points on a surface can lead to different results of calculated metrological characteristics [67]. Without prior information regarding the spatial amplitude and frequency components on a gear flank, a calculated parameter is prone to discrepancy under different point density and point distribution. According to VDI 2607 [20], three data acquisition procedures are used to collect the raw data on the flank before software evaluation:

- "*A certain number of measuring points are specified for the taking of measured data, independent of module and facewidth*";
- "*The spacing of the measured data is constant related to the roll path or axial way*";
- "*The data are taken with a specified frequency, i.e. the measuring point density is dependent on the tracing velocity*".

These procedures are usually selected during the planning phase of a gear inspection task before the measurement procedure is executed. In conventional tactile gear inspection, three types of measured point distribution are specified as illustrated in Figure 5.3 (a).

The start and end values of the roll angle are determined by the start and end values of diameters as:

$$\begin{cases} \xi_{st} = \tan\left[\arccos\left(\dfrac{r_b}{r_{st}}\right)\right] \\ \xi_{end} = \tan\left[\arccos\left(\dfrac{r_b}{r_{end}}\right)\right] \end{cases}. \tag{5.12}$$

Figure 5.3 (b) illustrates the location of the start and end points on an involute. Figure 5.3 (c) shows the values of seven simulated start and end roll angles corresponding to each the three types of point distribution within the range of r_{st} (29.77 mm) and r_{end} (34.93mm).

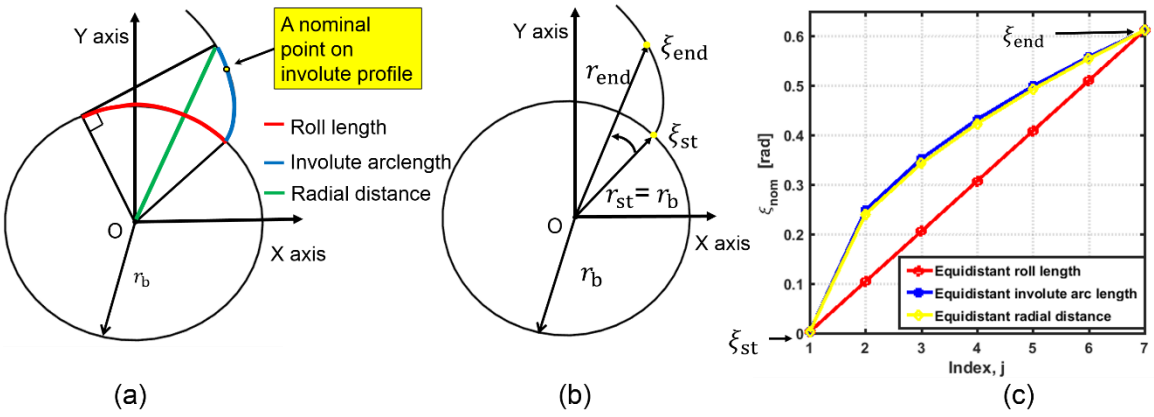

Figure 5.3: Illustration of nominal points distributions on a pure involute profile in the transverse plane: (a), three characteristic distance features for defining the location of a nominal point; (b), locations of the start and end roll angle on a pure invoute; (c), values of seven simulated start and end roll angles corresponding to each type of point distribution.

5.2.1 Three types of equidistant distribution of spatial points

5.2.1.1 Equidistant distribution on roll angle (i.e. length of roll)

This type of equidistant distribution of points is specified on the length of roll on a nominal involute, which can be derived by dividing the length of roll (denoted by L_{AE}) into a given number of sampling intervals. The value of the length of roll is determined by the start and end of roll angle, as:

$$L_{\mathrm{AE}} = r_{\mathrm{b}}(\xi_{\mathrm{end}} - \xi_{\mathrm{st}}). \tag{5.13}$$

Thus, the value of each roll angle (denoted by ξ_{AE}) at the corresponding evenly spaced length of roll is:

$$\xi_{\mathrm{AE}}(j) = \xi_{\mathrm{st}} + \frac{j-1}{n_{\xi}-1}(\xi_{\mathrm{end}} - \xi_{\mathrm{st}}), \quad j = 1, 2, 3, ..., n_{\xi}, \tag{5.14}$$

where j is the index number of each roll angle and n_{ξ} is the total number of roll angles in the discrete data set.

Figure 5.4 (a) illustrates the locations of a set of nominal points generated in a nominal profile. The *u* and *v* values for generating the spatial coordinates of those points are shown in Figure 5.4 (b), where each intersection point of the horizontal and vertical lines represent a pair of (*u*, *v*). The locations of those simulated points in the 3D Cartesian coordinates are illustrated in Figure 5.4 (c).

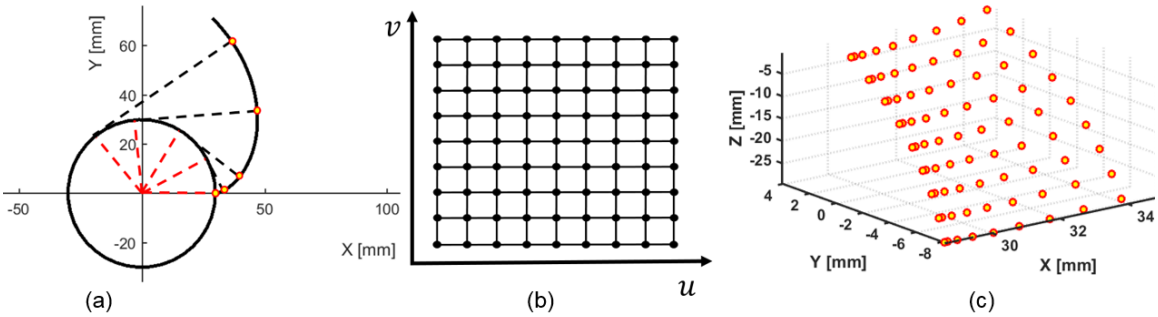

Figure 5.4: Illustration of equidistant distribution of nominal points on roll angle (i.e. length of roll): (a) on transverse plane, (b) values of (*u*, *v*), (c) locations in 3D Cartesian coordinate system.

5.2.1.2 Equidistant on involute arc length

This type of nominal point distribution is the equidistant distribution of the points on the involute arc length. Based on the parametric representation of an involute curve in Equation (2.1), the arc length of an involute (denoted by L_{inv}) can be calculated by the definite integral using the start and the end values as the upper and lower integration limits:

$$L_{\text{inv}} = \int_{\xi_{\text{st}}}^{\xi_{\text{end}}} \sqrt{\left(\frac{dx_{\text{nom}}}{d\xi_{\text{nom}}}\right)^2 + \left(\frac{dy_{\text{nom}}}{d\xi_{\text{nom}}}\right)^2}\, d\xi = \frac{1}{2} r_{\text{b}}{}^2 (\xi_{\text{end}}^2 - \xi_{\text{st}}^2). \tag{5.15}$$

Thus, the value of each roll angle (denoted by ξ_{inv}) for equidistant involute arc length at the corresponding evenly spaced involute arc length is:

$$\xi_{\text{inv}}(j) = \sqrt{\xi_{\text{st}}^2 + \frac{j-1}{n_\xi - 1}\left(\xi_{\text{end}}^2 - \xi_{\text{st}}^2\right)}, \quad j = 1, 2, 3, \ldots, n_\xi, \tag{5.16}$$

where j is the index of each roll angle and n_ξ is the total number of discretized roll angles.

Figure 5.5 (a) illustrates the locations of individual points on a nominal involute for equidistant distribution of involute arc length. The *u* and *v* values for generating the

spatial coordinates of those points are shown in Figure 5.5 (b), where each intersection point of the horizontal and vertical lines represent a pair of (u, v). The locations of those simulated points in the 3D Cartesian coordinates are illustrated in Figure 5.5 (c).

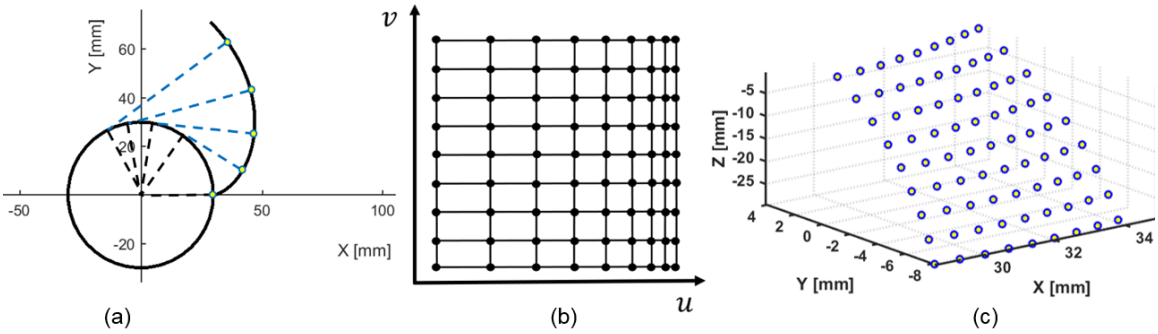

Figure 5.5: Illustration of equidistant distribution of nominal on involute arc length: (a), points on transverse plane; (b), values of (u, v) for each nominal point; (c), locations in 3D Cartesian coordinate system.

5.2.1.3 Equidistant distribution in radial direction

The third type of nominal points distribution of nominal points are specified with respect to the radial distance of the points on the nominal involute. The origin of the base circle coincides with that of the coordinate system for determining the values of the indexed roll angle. Therefore, the radial distance from the origin of the base circle to a point on the nominal involute (denoted by L_{rad}) is:

$$L_{\text{rad}} = \rho = \sqrt{x_{\text{nom}}^2 + y_{\text{nom}}^2} = r_{\text{b}}\sqrt{1+\xi_{\text{nom}}^2}\,. \tag{5.17}$$

Thus, the value of each roll angle (denoted by ξ_{rad}) for equal radial distance distribution is:

$$\xi_{\text{rad}}(j) = \sqrt{\frac{1}{r_{\text{b}}^2}\left[r_{\text{st}} + \frac{j-1}{n_\xi - 1}(r_{\text{end}} - r_{\text{st}})\right]^2} - 1, \quad j = 1, 2, 3, \ldots, n_\xi\,, \tag{5.18}$$

where, j is the index of each roll angle, n_ξ is the total number of discretized roll angle, $r_{st} = r_b\sqrt{1+\xi_{st}^2}$ and $r_{end} = r_b\sqrt{1+\xi_{end}^2}$ are the values of the start and the end radius respectively. Figure 5.6 (a) illustrates the locations of individual nominal points on the involute based on the equidistant distribution of radial distance. The *u* and *v* values for generating the spatial coordinates of those points are shown in Figure 5.6 (b), where each intersection points of the horizontal and vertical lines stand for a pair of (*u*, *v*). The locations of those simulated points in the 3D Cartesian coordinates are illustrated in Figure 5.6 (c).

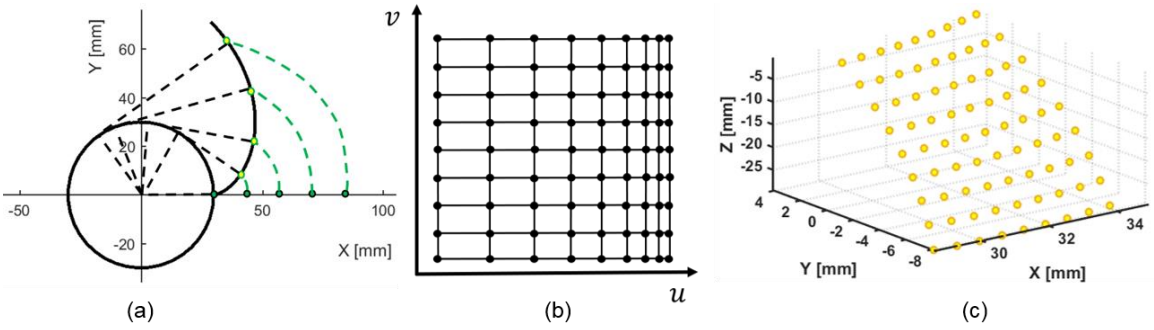

Figure 5.6: Illustration of equidistant distribution of nominal points on radial distance: (a), points on transverse plane; (b), values of (*u*, *v*) for each nominal point; (c), location of simulated nominal points in 3D Cartesian coordinate system.

5.2.2 Comparisons of numerical algorithms

The three algorithms discussed in Section 5.1 are used to compare the influence of point distribution type and point density of a flank to the computational time of the 2D Chebyshev method. Numerical simulations were implemented through MATALB® 2016b on a Dell Precision T5810XL desktop computer, equipped with Intel® Xeon® CPU E5-1620 v3 @ 3.50 GHz and RAM 16.0 GB.

The number of points per flank is specified as an exponential of 2 for a square matrix with equal row and column length for the profile and helix directions, respectively. For example, the number of points of 2^{10} per flank means that a square matrix (2^5 rows and 2^5 columns) is used for simulating the coordinates of points on a flank. The computational time is calculated by the MATLAB functions "tic" and "toc".

The concept of using an iteration loop to resolve non-orthogonality related issues will be discussed in Section 5.3.1, together with the choice of convergence criteria. It is assumed that the following discussion about the number of iterations in this section is based on the same convergence criteria used to study the influence of point distributions, the number of points per flank and the calculation algorithms etc.

Figure 5.7 (a) shows the computation time of three different point distributions as a function of points per flank by the empirical edge method. The more points per flank, the more computation time is needed. It is noticeable that the starting number per flank for equidistant roll involute arc length and radial distance are 2^{12} and 2^{14} respectively. This is because insufficient points per flank leads to a loss of orthogonality issue, which may cause the iteration fail to converge.

Figure 5.7 (b) shows the corresponding number of iterations as a function of points per flank. As the number of points per flank increases, the number of iterations decreases for all three types of point distributions. The number of iterations are the same when the points per flank is at 2^{18}. This trend is due to the improvement of numerical orthogonality as the number of points per flank is increased. A similar performance of using the 2D Cosine variable method is shown in Figure 5.8.

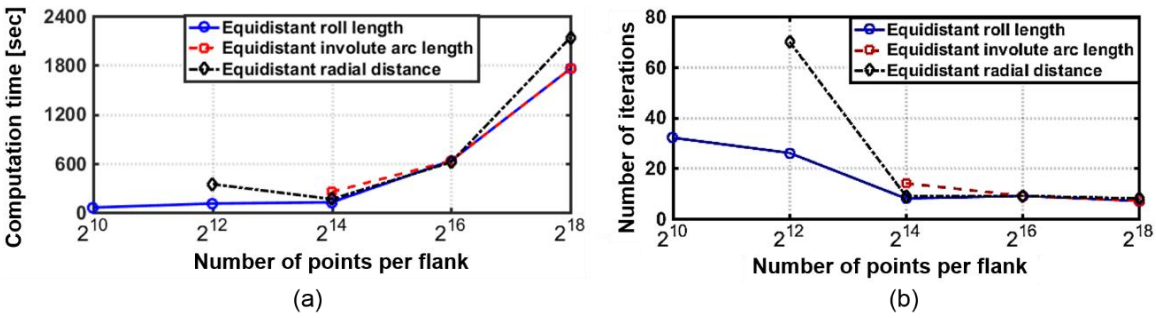

Figure 5.7: Computational performance on simulated three types of points distributions: (a), computing time (by the empirical edge method) as a function of points per flank; (b), number of iterations as a function of points per flank.

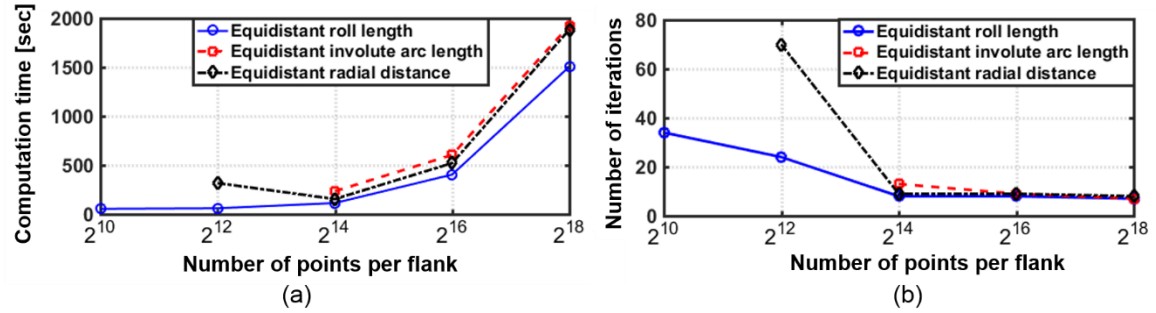

Figure 5.8: Computational performance on simulated three types of points distributions: (a), computational time (by the 2D Cosine variable method) as a function of points per flank; (b), number of iterations as a function of points per flank.

As shown in Figure 5.9, the 2D DCT method provides a significant computational performance improvement, compared to the other two methods. Firstly, for all three types of point distributions, this method offers convergent results when the number of point per flank is changing from 2^{10} to 2^{18} as shown in Figure 5.9 (a). Secondly, the computation time is about 4 times shorter compared to the other two methods. Lastly, the number of iterations needed for all three types of point distributions are all less than 10 as shown in Figure 5.9 (b).

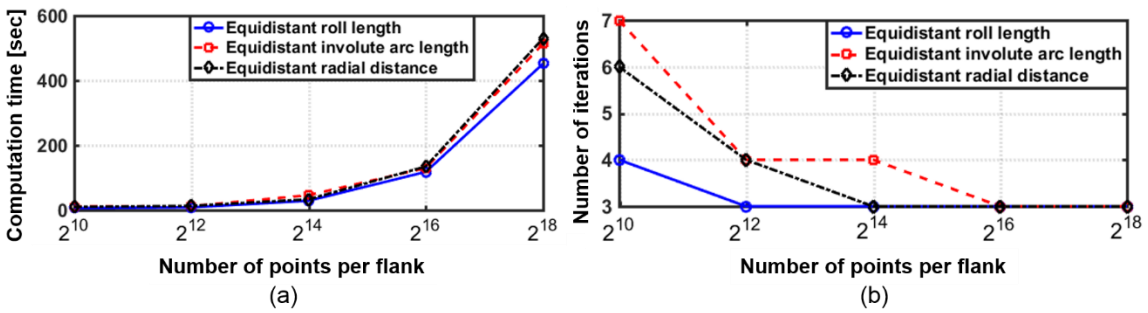

Figure 5.9: Computational performance on simulated three types of points distributions: (a), computational time (by the 2D DCT method) as a function of points per flank; (b), number of iterations as a function of points per flank.

5.2.3 Random distributed points on flank

Moreover, a point cloud with randomly distributed *u*-*v* values is used to test the capability and limitations of each calculation method. A simulated gear with flank modifications is shown in Figure 5.10 (a). The simulated points are randomly located on the flank and the amount of modification with respect to the pure involute surface is color-coded. The right flanks of all teeth are shown in Figure 5.10 (b).

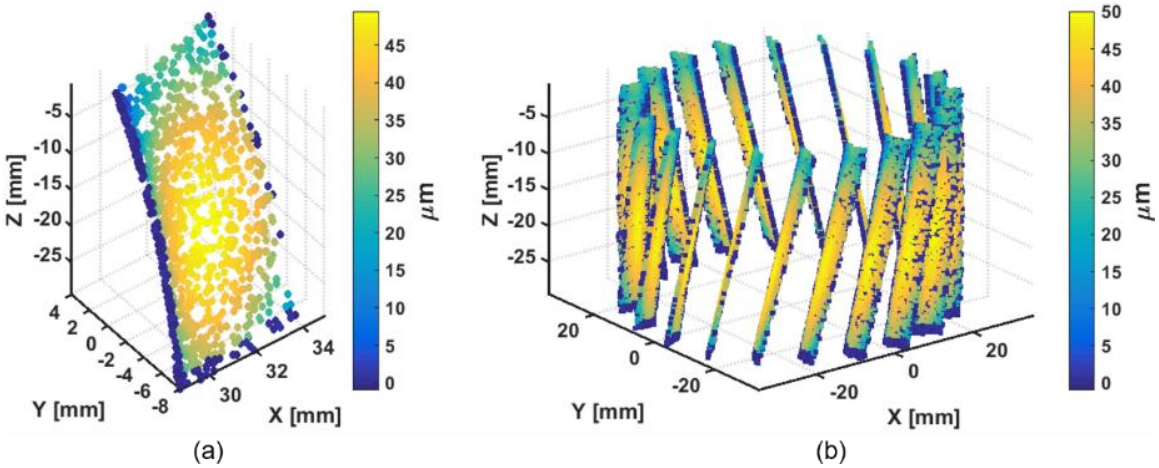

Figure 5.10: Randomly distributed points (2^{10} points per flank) with simulated modifications: (a), points on a flank; (b), points on a complete gear view (only right flanks are shown).

Figure 5.11 shows the relationship between the number of points per flank and the number of iterations needed for convergence, when the points are randomly distributed on each flank. A comparison of the corresponding time cost of each computation method is shown in Figure 5.12. In Figure 5.12 (b), it is possible to achieve the convergence in nearly half a minute when the number of points per flank is set to 2^8, 2^{10} and 2^{12}, respectively.

The selected criterion for terminating the iteration loop is based on the relative error, calculated as the ratio between the improved value of each areal gear parameters in the current iteration with respect to the approximated value them from last iteration. No noise was added to the simulated areal distance map and the relative error was set to 0.1%.

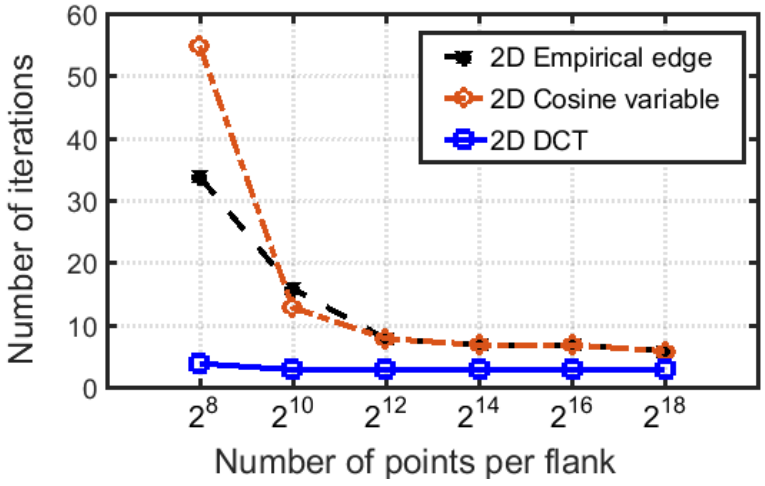

Figure 5.11: Relationship between number of iterations for convergence of the three algorithms as a function of the number of points per flank (random spatial points distribution).

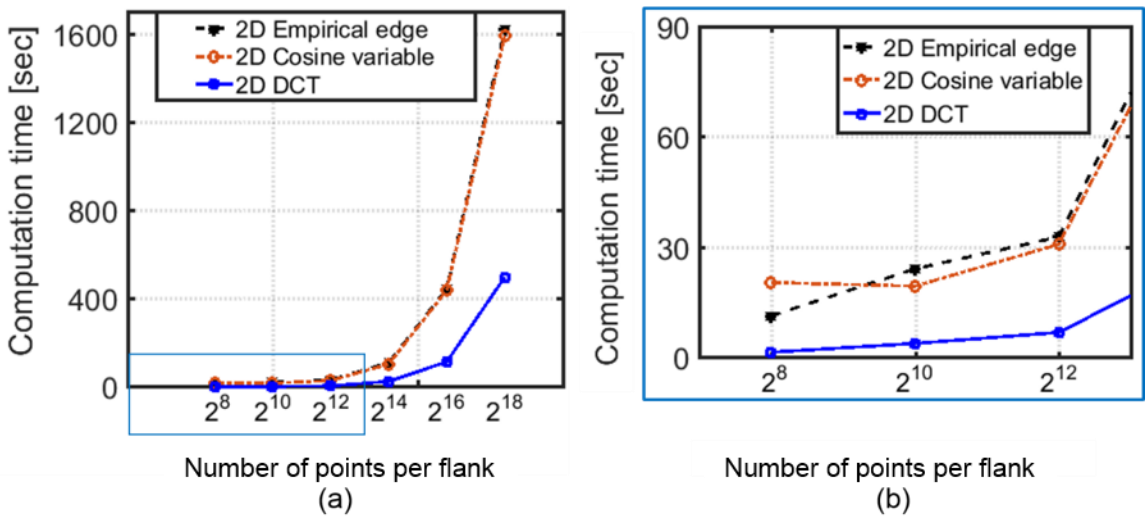

Figure 5.12: Computational performance on simulated randomly distributed points on flank: (a), computing time (by the three algorithms) as a function of the number of points; (b), a zoomed in view of (a).

For randomly distributed points, the 2D Empirical edge method and 2D Cosine variable method can also reach to a convergence. This result is neither achieved for the distribution of equidistant involute arc length nor the distribution of equidistant radial distance.

5.3 Non-orthogonality and post-sampling related issues

5.3.1 Loss of orthogonality on pixelated data

When a set of orthogonal functions are used to approximate an unknown measured dataset, the loss of orthogonality is a typical issue due to the discrete nature of the pixelated data. In the 1D case, discrete orthogonality can be obtained only if the sampling and evaluation points are located exactly at the Chebyshev points on the interval of [-1,1] [57]. This condition is rarely satisfied in metrology practice, since raw data are either uniformly sampled or randomly sampled in an area for evaluation. One typical solution to the non-

orthogonality issue is to increase the number of pixels. For example, in optical interferometry, using an imaging detector with a higher number of pixels can mitigate the numerical issues caused by the non-orthogonality, when Zernike polynomials are applied [68]. The same strategy is used here to improve the relative error, when the 2D Chebyshev coefficients are to be evaluated on a pixelated dataset, namely an areal distance map.

However, an increased number of points per flank leads to a longer computation time. Therefore, it is a tradeoff to select a reasonable number of points, given an acceptable value of numerical accuracy from a computational perspective. Table 5.1 shows the values of the simulated and approximated six 2D Chebyshev coefficients from areal distance maps of different sizes. The point distribution is random and no noise was added in this simulation. The algorithm used in the following comparison is the 2D DCT algorithm.

Table 5.1: The nominal and calculated values of the first five 2D Chebyshev coefficients from a simulated flank with different grid size (unit: μm).

Coefficient	Nominal value	Grid size			
		32 by 32	64 by 64	128 by 128	256 by 256
A_1	2.5	2.4812	2.4988	2.4997	2.4997
A_2	5	5.0194	5.0086	5.0002	5.0001
A_3	-7.5	-7.5325	-7.4987	-7.5001	-7.4999
A_4	-6.25	-6.2249	-6.2419	-6.2494	-6.2501
A_5	-10	-9.9562	-10.0000	-9.9990	-10.000

The relative errors for each calculated 2D Chebyshev coefficients in Table 5.1 are plotted in Figure 5.13. When the pixel size is increased to 128 by 128, all the relative errors are below ± 0.01%.

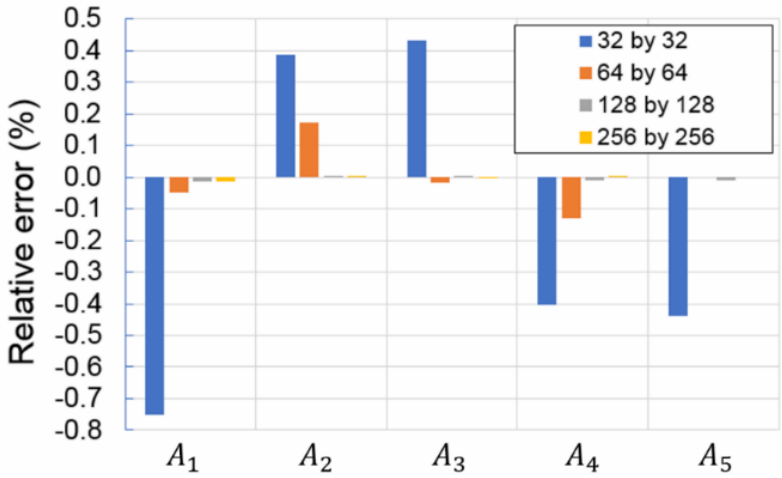

Figure 5.13: The relative errors of the calculated 2D Chebyshev coefficients with respect to the nominal values in Table 5.1.

Another way to reduce the relative error caused by non-orthogonality is to use a looped algorithm that iteratively extracts the low order components from an areal distance map.

As illustrated in the flow chart in Figure 5.14, this algorithm starts with basic gear geometric parameters to form the plumb line distance equation and a predetermined convergent criteria (usually a relative error or a maximum number of iterations). Then, the raw point clouds are fed into the plumb line distance and generate an areal distance map in the *u*-*v* domain. Afterwards, the 2D Chebyshev method is used to obtain areal flank parameters and reconstruct the areal map based on the calculated 2D Chebyshev coefficients. Lastly, a residual map is obtained by point wise comparison between the

reconstructed areal map to the original areal map. If a convergence criterion is not met, then the residual map will be fed back as the original areal map for the next iteration.

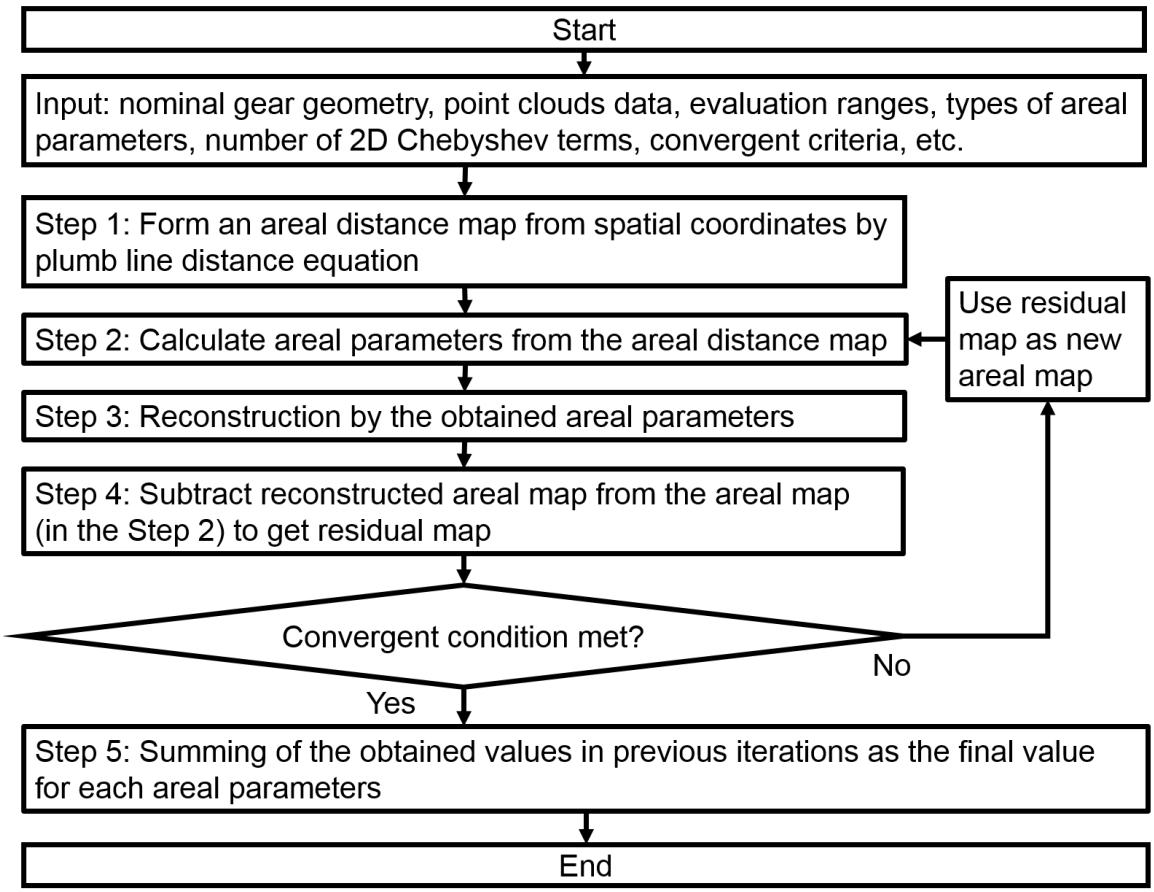

Figure 5.14: Flow chart for iterative improvement of areal parameters for single flank.

Two types of criteria are used to terminate the iteration loop. The first one is the relative error of the improved value of the areal parameters to the previous value. Usually 1% is sufficient. The other type is the total number of iterations. Usually 10 iterations are sufficient.

5.3.2 Sub-flank areal evaluation

A complete flank is bounded by the evaluation range in both profile and helix direction during areal evaluation. As shown in Figure 5.15, a portion of a complete flank with different size and located arbitrarily on the flank is referred to as a sub-flank. An analogous concept is called “sub-aperture” used in optical surface metrology [69]. A sub-flank can be of arbitrary shape as shown in Figure 5.15 (a); in this dissertation, only sub flanks of rectangular shapes whose two sides are aligned in the profile and helix evaluation range respectively are used as shown in Figure 5.15 (b).

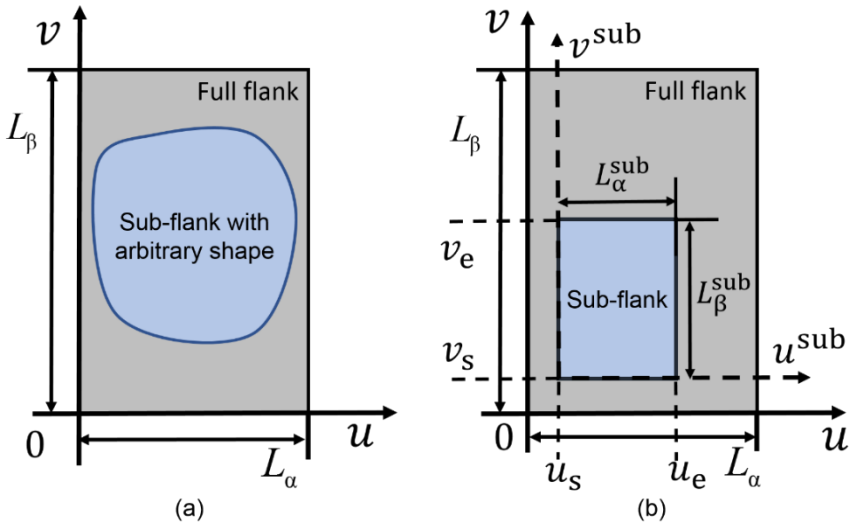

Figure 5.15: Illustration of sub-flank sampling: (a), schematic of a sub-flank of arbitrary shape on the full flank; (b), schematic of a rectangular sub-flank of the full flank.

The study of sub-flank evaluation has two major impacts for future areal gear metrology. If an instrument has difficulty accessing a full flank, or it is too time-consuming to be captured, then it is necessary to investigate the feasibility of the 2D Chebyshev method for extracting full flank information from a sub-flank. In particular, as far as the

low order form information is concerned, it is important to know how well the areal parameters for a full gear flank can be retained on its sub-flanks. Lastly, it is essential to determine the critical characteristics of a sub-flank for obtaining reliable sub-flank evaluation results. Those characteristics could be the shape of the sub-flank, the location of the sub-flank as described on the *u*-*v* plane; the relative size of the sub-flank with respect to the full flank and the number of points within the sub-flank compared to the full flank etc.

As shown in Figure 5.16 (a), six sub-flanks are specified in the *u*-*v* plane and assigned a zone number. Figure 5.16 (b) shows the spatial location of each sub-flank in the Cartesian coordinate system. The basic information of the full-flank is summarized in Figure 5.16 (c), including the evaluation range in the profile and helix directions, the full-flank area, the number of points in the full flank and the type of point distributions in the full flank.

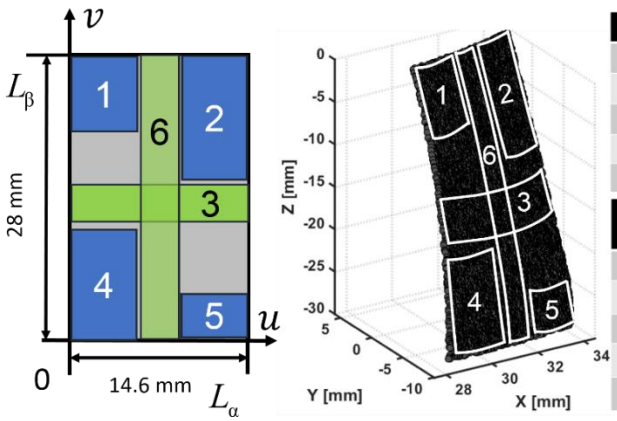

Full flank geometry	Value	Unit
Profile evaluation range	14.6	mm
Helix evaluation range	28	mm
Full flank area	459.2	mm²
Number of points	59914	No unit
Points distribution type	Random	No unit

Full flank modifications	Value	Unit
$C_{H\alpha}^{A}$	5	µm
$C_{H\beta}^{A}$	10	µm
C_{α}^{A}	15	µm
$S_{\alpha\beta}^{A}$	25	µm
C_{β}^{A}	20	µm

(c)

Figure 5.16: Design of sub-flank for simulation: (a), full flank and the locations of six sub-flank zones on a gear flank in *u*-*v* domain; (b), locations of sub flank zones on the right flank of a gear in Cartesian coordinate system; (c), evaluation and modification parameters.

Table 5.2 shows the values of start and end locations denoted by u_s, u_e, v_s and v_e for each sub-flank, area percentage, number of points in sub-flank and the number of point percentage for the corresponding sub-flank.

Table 5.2: Information of rectangular sub-flank zones.

Zone #	u_s [mm]	u_e [mm]	v_s [mm]	v_e [mm]	Area percentage	Points in zone	Number of points percentage
1	0	5.84	19.6	28	12%	4129	7%
2	8.76	14.6	16.8	28	16%	13492	22%
3	0	14.6	9.8	14	15%	8898	15%
4	0	5.84	0	14	20%	6927	12%
5	10.22	14.6	0	8.4	9%	8014	13%
6	5.11	8.03	0	28	20%	11256	19%

The following results listed from Table 5.3 to Table 5.5 were obtained on the three algorithms by five iterations respectively. The relative error between the nominal areal parameters and the calculated sub-flank parameters by three different algorithms are summarized from Figure 5.17 to Figure 5.19.

It is noticeable that the areal profile slope parameter is much more sensitive in sub-flank evaluation compared to other areal parameters regardless which evaluation algorithm was applied. Moreover, in sub-flank zone #4, the areal profile slope parameter from the first two algorithms show significant deviation compared to that from the 2D DCT method.

Table 5.3: Areal gear parameters calculated from sub-flank data on a simulated gear flank using empirical edge method (5 iterations, unit: μm).

Zone #	$C_{H\alpha}^{A}$	$C_{H\beta}^{A}$	C_{α}^{A}	$S_{\alpha\beta}^{A}$	C_{β}^{A}
Full flank	5	10	15	25	20
1	5.62	9.58	14.84	25.13	19.86
2	5.19	9.81	14.93	25.6	19.91
3	5.19	10.00	14.99	24.98	19.98
4	3.48	9.63	15.53	25.36	20.12
5	5.22	9.96	15.02	25.03	20.01
6	5.01	9.99	15.25	25.06	20.00

Table 5.4: Areal gear parameters calculated from sub-flank data on a simulated gear flank using change of cosine variable method (5 iterations, unit: μm).

Zone #	$C_{H\alpha}^{A}$	$C_{H\beta}^{A}$	C_{α}^{A}	$S_{\alpha\beta}^{A}$	C_{β}^{A}
Full flank	5	10	15	25	20
1	5.77	9.37	14.79	25.24	19.79
2	5.23	9.85	14.94	25.05	19.93
3	5.19	10.03	14.99	24.97	19.93
4	3.69	9.67	15.48	25.20	20.13
5	5.23	9.95	15.02	25.02	20.02
6	4.97	9.99	15.31	25.06	20.00

Table 5.5: Areal gear parameters calculated from sub-flank data on simulated gear using 2D DCT method (5 iterations, unit: μm).

Zone #	$C_{H\alpha}^{A}$	$C_{H\beta}^{A}$	C_{α}^{A}	$S_{\alpha\beta}^{A}$	C_{β}^{A}
Full flank	5	10	15	25	20
1	5.24	9.99	15.00	25.00	20.00
2	5.36	9.98	15.00	25.00	20.00

3	5.19	9.99	15.00	25.00	20.00
4	5.00	10.00	15.00	25.00	20.00
5	5.18	9.99	15.00	25.00	20.00
6	5.14	9.99	15.00	25.00	20.00

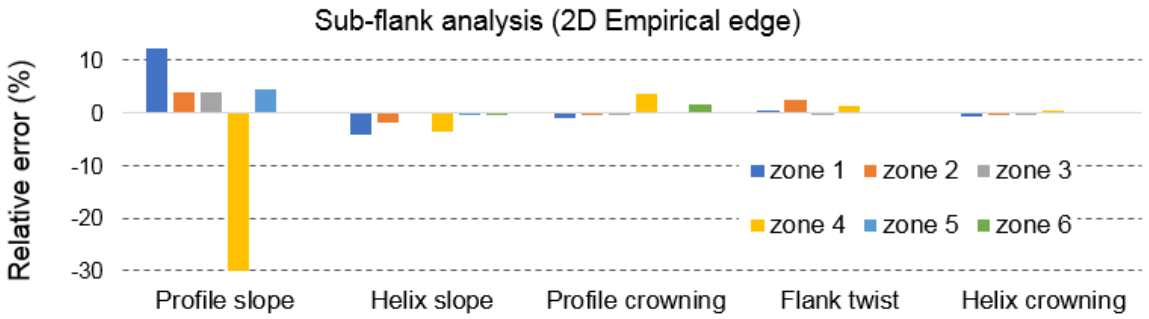

Figure 5.17: Relative errors of obtained sub-flank areal parameters with respect to full flank areal parameters (2D Emprical edge method).

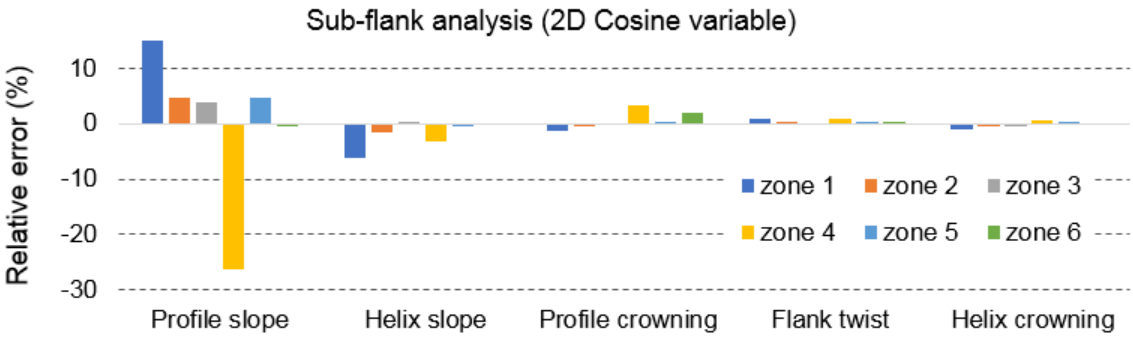

Figure 5.18: Relative errors of obtained sub-flank areal parameters with respect to full flank areal parameters (2D Cosine variable method).

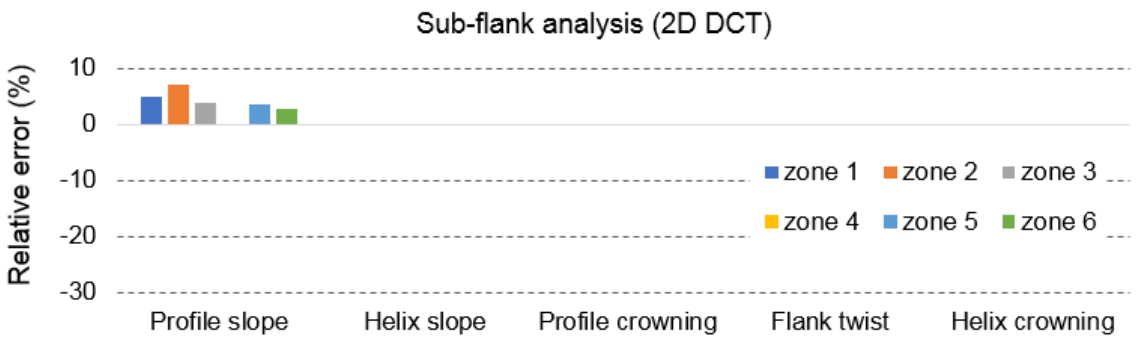

Figure 5.19: Relative errors of obtained sub-flank areal parameters with respect to full flank areal parameters (2D DCT method).

The computation time is the time spent on five iterations to obtain the areal parameters of the simulated complete gear (right flanks). For each sub-flank zone, the computation time is linearly proportional to the corresponding number of points percentage as shown in Figure 5.20 (a) and Figure 5.20 (b).

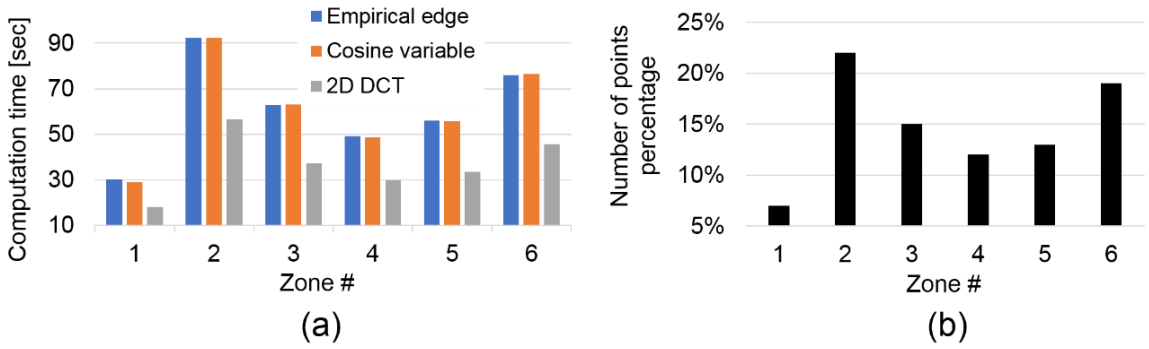

Figure 5.20: Computation time for each sub-flank: (a), computation time for each sub-flank zone by three algorithms; (b), number of points percentage for each sub-flank zones with respect to the full flank.

5.4 Influence of misalignment

In coordinate metrology, alignment has two meanings in different technical contexts. For example, alignment could refer to the procedure of setting up a workpiece

coordinate system according to the engineering drawing of a workpiece. The completion of this process establishes a workpiece coordinate system (CSY) for the measuring instrument to generate, measure and evaluate geometric features on the workpiece in a digital environment autonomously [67]. In addition, after a feature is measured, it is imperative to know the comparison between the nominal and the measured according to defined deviations (e.g. the defined distance functions in Section 2.3), which is frequently referred to as matching, registration, or correspondence in different disciplines [70]. This procedure usually involves iterative calculation, using the six degree of freedom as iteration parameters to obtain an optimized objective function, which leads to a numerically aligned measured feature and an evaluated deviation simultaneously [49]. The latter alignment is therefore purely mathematical and no mechanical operation is involved.

When measuring a gear, the workpiece CSY (e.g. Figure 5.21) can be built on datum features on the gear body such as the center bore and the datum face. In practice, numerous factors can lead to a misaligned workpiece CSY based on the measured datum features with respect to the nominal one. For example, the form deviation of the center bore might lead to an eccentricity error between the origin of the measured CSY to its nominal; the tip or tilt motion of the rotary table, on which the gear sample is clamped, might result in an orientation error of one of the measured CSY's axis etc.

In this section, a variety of kinematic motions are simulated to investigate the change of areal gear parameters under their influence. The abstraction of kinematic motions (three linear translations and three angular rotations) is denoted by T in Figure 5.21, which

has six components of ΔX, ΔY, ΔZ, θ_X, θ_Y and θ_Z representing the linear translation and angular rotations in and with respect to the X, Y and Z axes, respectively.

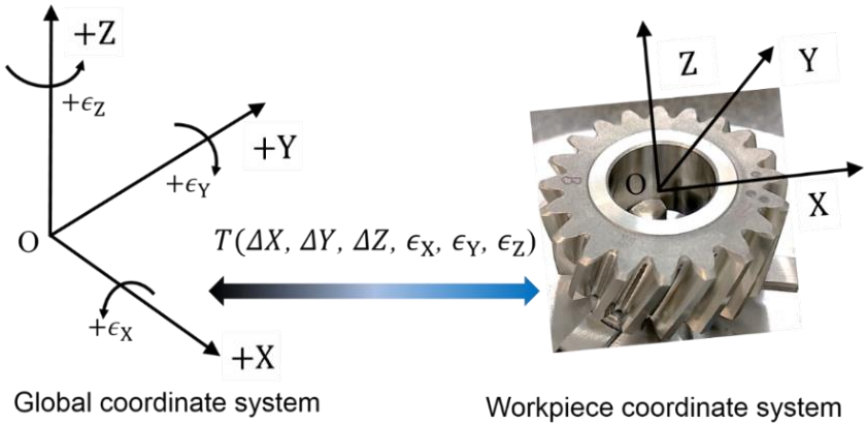

Figure 5.21: Schematic of global coordinate system and workpiece coordinate systems.

T can be represented by a four by four matrix, known as a homogeneous transformation matrix (HTM). Equation (5.19) is the HTM representations for rotational matrices with respect to the X, Y and Z axis (denoted by $\mathbf{T}_{\epsilon_X}$, $\mathbf{T}_{\epsilon_Y}$ and $\mathbf{T}_{\epsilon_Z}$) respectively.

$$\mathbf{T}_{\theta_X} = \begin{bmatrix} 1 & 0 & 0 & 0 \\ 0 & \cos\epsilon_X & \sin\epsilon_X & 0 \\ 0 & -\sin\epsilon_X & \cos\epsilon_X & 0 \\ 0 & 0 & 0 & 1 \end{bmatrix}, \mathbf{T}_{\theta_Y} = \begin{bmatrix} \cos\epsilon_Y & 0 & \sin\epsilon_Y & 0 \\ 0 & 1 & 0 & 0 \\ -\sin\epsilon_Y & 0 & \cos\epsilon_Y & 0 \\ 0 & 0 & 0 & 1 \end{bmatrix},$$
$$\mathbf{T}_{\theta_Z} = \begin{bmatrix} \cos\epsilon_Z & \sin\epsilon_Z & 0 & 0 \\ -\sin\epsilon_Z & \cos\epsilon_Z & 0 & 0 \\ 0 & 0 & 1 & 0 \\ 0 & 0 & 0 & 1 \end{bmatrix}. \quad (5.19)$$

Equation (5.20) is the HTM representations of the three translational matrices in the X, Y and Z axes (denoted by $\mathbf{T}_{\epsilon_X}$, $\mathbf{T}_{\epsilon_Y}$ and $\mathbf{T}_{\epsilon_Z}$) respectively:

$$\mathbf{T}_X = \begin{bmatrix} 1 & 0 & 0 & \Delta X \\ 0 & 1 & 0 & 0 \\ 0 & 0 & 1 & 0 \\ 0 & 0 & 0 & 1 \end{bmatrix}, \mathbf{T}_Y = \begin{bmatrix} 1 & 0 & 0 & 0 \\ 0 & 1 & 0 & \Delta Y \\ 0 & 0 & 1 & 0 \\ 0 & 0 & 0 & 1 \end{bmatrix}, \mathbf{T}_Z = \begin{bmatrix} 1 & 0 & 0 & 0 \\ 0 & 1 & 0 & 0 \\ 0 & 0 & 1 & \Delta Z \\ 0 & 0 & 0 & 1 \end{bmatrix}. \quad (5.20)$$

A simulation process is proposed to investigate the influence of a misalignment between the nominal workpiece coordinate system to the areal gear parameters. A simulated misalignment is mathematically represented by a HTM including either translational errors or rotational errors. The steps of this simulation are:

- Step 1 : generate nominal point clouds of the flanks of a complete gear (left and right flanks) without deviations and modifications and store the spatial coordinates of the nominal points into matrices of multiple rows and three columns;
- Step 2: simulate translational or rotational errors and form them into a HTM, representing the effect as if an alignment error between the nominal workpiece coordinate system to the established workpiece cooridnate system in measurement process;
- Step 3: apply matrix multiplication on the nominal spatial coordinates by the HTM and store the new spatial coordinates after multiplication;
- Step 4: apply the 2D Chebyshev method on the new spatial coordinates (i.e. transformed point clouds) to obtain the areal gear parameters under the influence of a specific simulated kinematic error.

The purpose of this study is aimed at investigating the pattern of different areal parameters of each flank on all teeth, under the influences of various kinematic errors.

Therefore, it would offer insights regarding how to apply the information exhibited in the pattern to identify the influence of misalignment to areal parameters.

5.4.1 Areal parameters influenced by translational errors

Figure 5.22 shows the location of the new coordinate system after two translational errors in the X axis direction. It is worthwhile to point out that if the shift of the origin of the new CSY with respect to the original one is in the negative direction, then the HTM which maps the old spatial coordinates of nominal points in the original CSY should have an opposite positive sign for the corresponding translational components.

The following observations and discussion are made regarding the simulated configuration of the CSY and the tooth counting direction. For the areal cumulative pitch deviation, it is a convention to set the cumulative pitch deviation of the first tooth (both left and right flanks) to zero and plot the rest of teeth with respect to the first tooth. For gear flank deviations other than pitch deviations, the conventional gear inspection method only measures four teeth (also marked by #1, #6, #11 and #16) on a gear sample with line oriented deviations. Thus, the following simulation can provide extra information such as a systematic global pattern (including amplitudes, peak to valley and phase change) as a function of teeth number, when the areal parameter from all teeth are available.

5.4.1.1 Translational error in X direction

Figure 5.23 and Figure 5.24 show the change of six areal gear parameters under the influences of the translational errors simulated in Figure 5.22 (a) and Figure 5.22 (b) respectively. Obviously, the areal cumulative pitch has the biggest peak to valley difference in response to the simulated translational errors. The peak and valley are found at teeth #6

and #16 because the cumulative pitch on those two flanks (regardless of left or right) are most sensitive to the translational error in the X axis.

Moreover, a 180-degree phase change between the left and right flanks can be observed on the areal cumulative pitch and areal helix slope parameters ($C_{H\beta}^{A}$). This is because the surface normal vector is pointing out of the material and the plumb line distance is a vectorial quantity, pointing from a measured point to its counterpart on the nominal gear flank. A shift will affect a pair of left and right flank in the opposite direction in terms of the sign of the plumb line distance. The same pattern shown in Figure 5.24 is observable, when the translational error in the X axis is in the opposite direction.

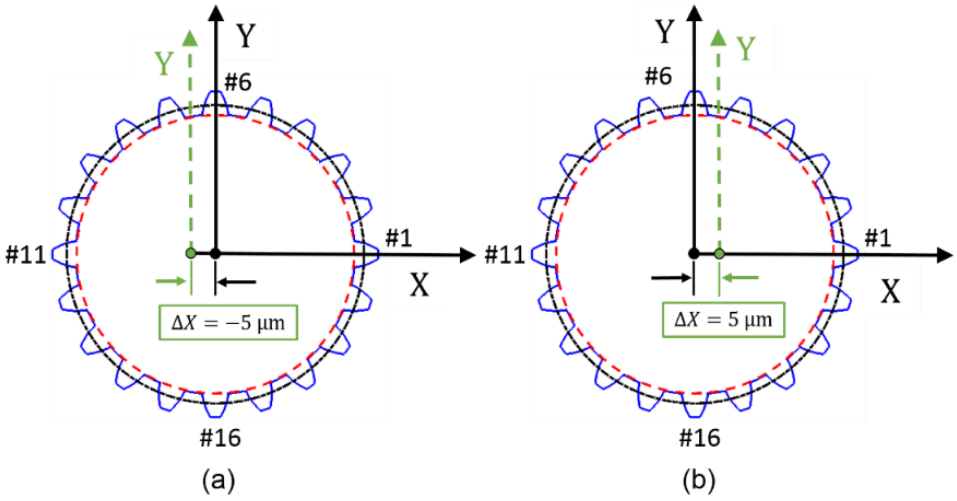

Figure 5.22: Simulated translational errors of the origin of the new CSY, relative to the nominal origin of the gear sample in the X directions: (a), -5 µm; (b),+5 µm.

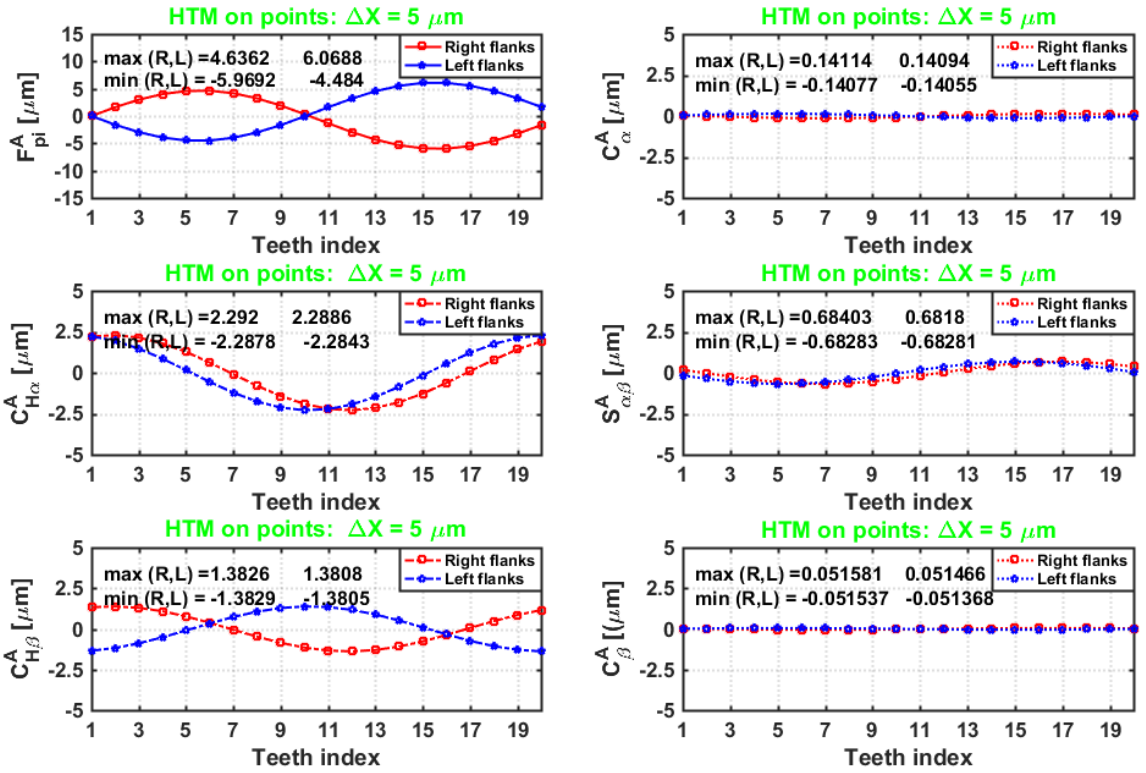

Figure 5.23: Change of areal gear parameters under a HTM of simulated translational error by +5 μm in the X axis, according to Figure 5.22 (a).

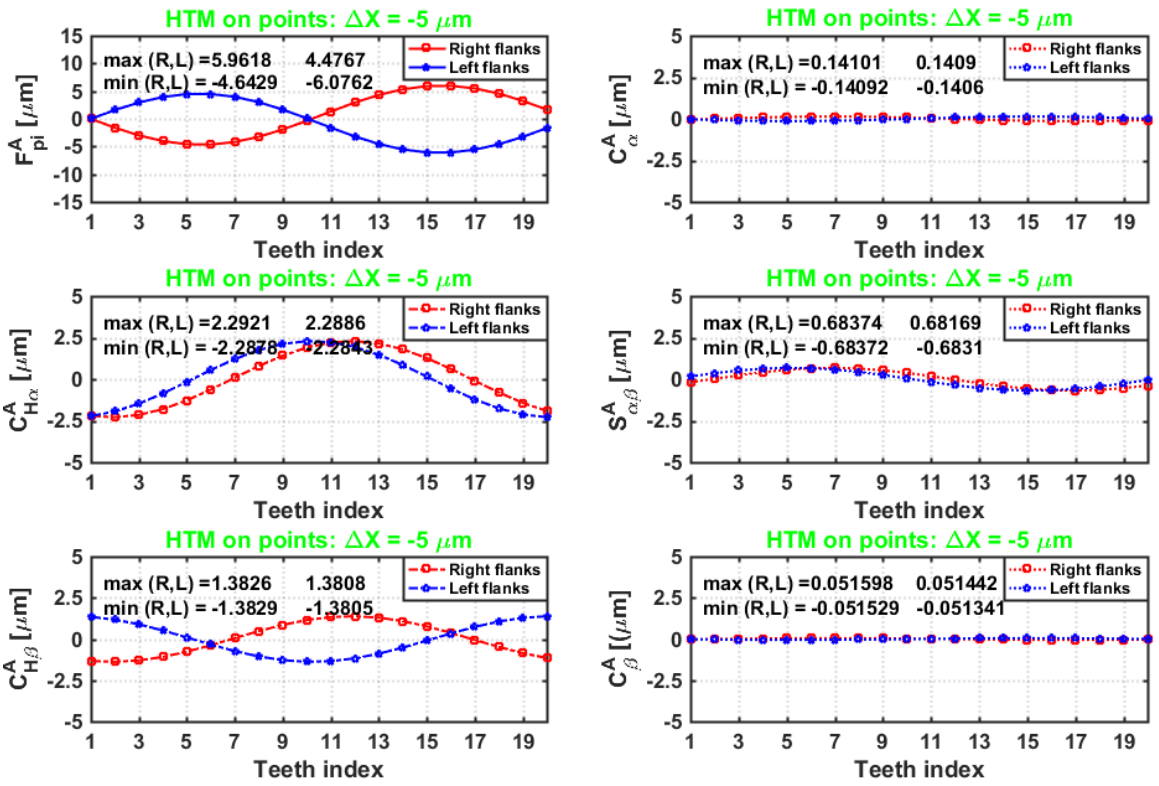

Figure 5.24: Change of areal gear parameters under a HTM of simulated translational error by -5 µm in the X axis, according to Figure 5.22 (b).

5.4.1.2 Translational error in Y direction

When the translational error is induced in the Y direction as given in Figure 5.25, the areal cumulative pitch deviation has a different pattern for both right and left flanks. Starting from the first tooth, the areal cumulative pitch curve is a sine wave, whose mean value of the cumulative pitch remains either positive or negative for right flanks and left flanks, respectively, as shown in Figure 5.26. The same pattern shown in Figure 5.27 is observable, when the translational error in the Y axis is in the opposite direction.

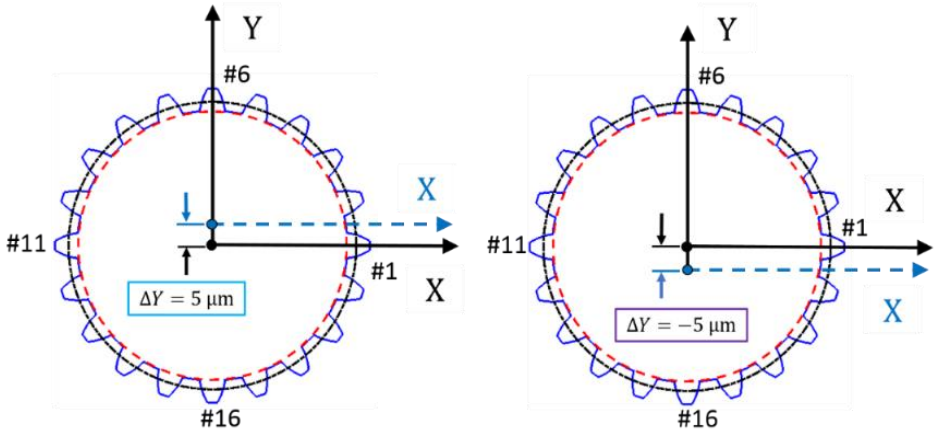

Figure 5.25: Simulated translational error of the origin of the CSY, relative to the nominal origin of the gear in the Y directions: (a), +5 µm; (b), -5 µm.

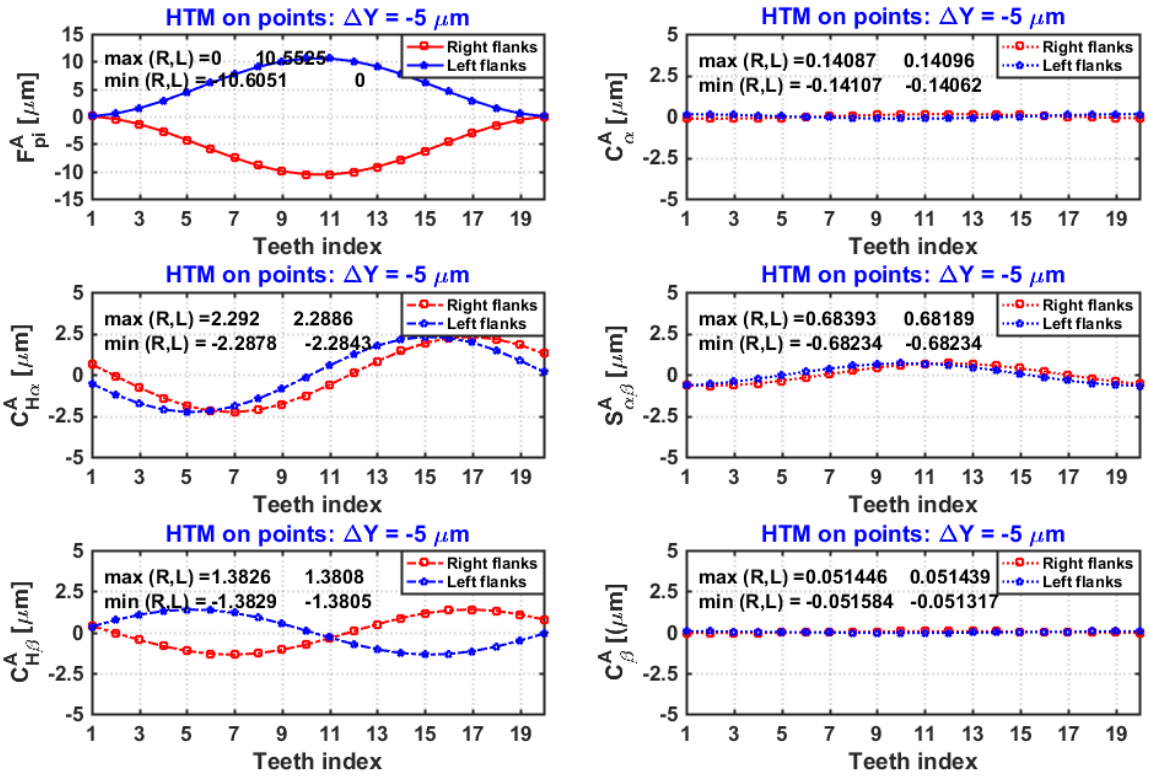

Figure 5.26: Change of areal gear parameters under a HTM of simulated translational error by -5 µm in the Y axis, according to Figure 5.25 (a).

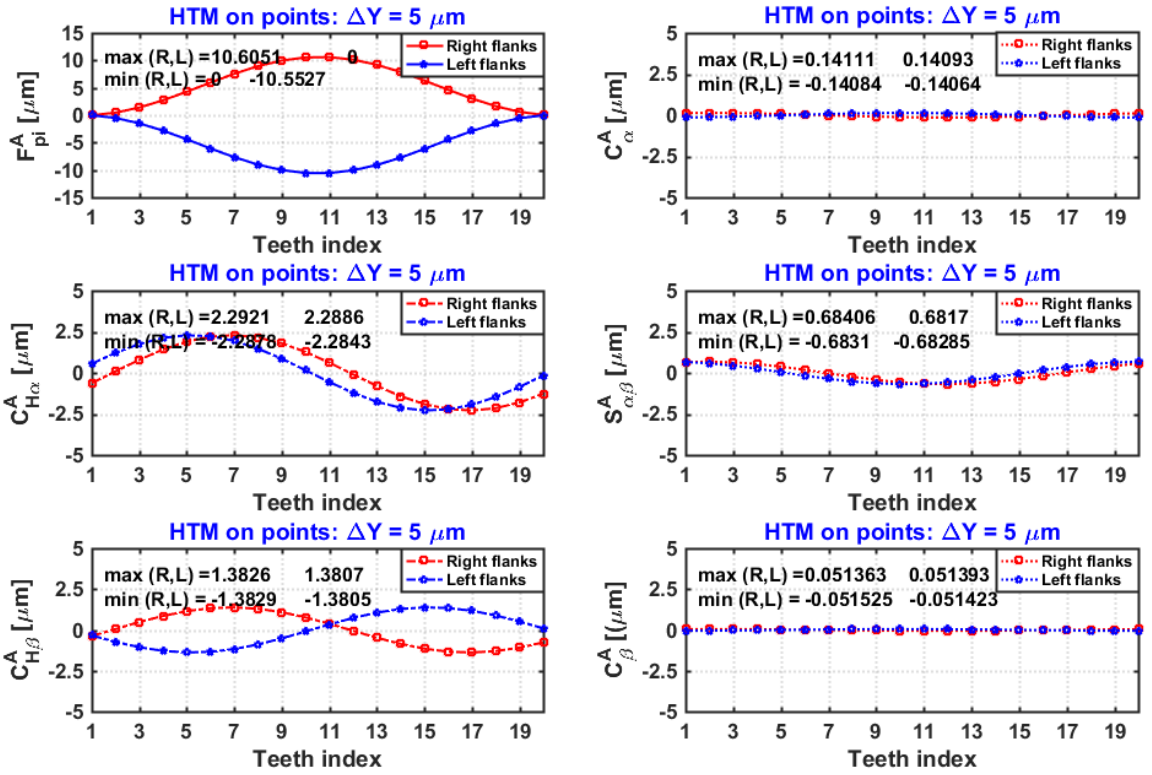

Figure 5.27: Change of areal gear parameters under a HTM of simulated translational error by +5 μm in the Y axis, according to Figure 5.25 (b).

5.4.1.3 Translational error in both X and Y directions

The last scenario is a combined translational error in both X and Y directions as shown in Figure 5.28. Two specific cases are simulated, namely the equal translational errors (same magnitude and same signs) for the two perpendicular axes. The areal parameter pattern plotted in Figure 5.29 and Figure 5.30 collectively indicate that tooth #8 is the most sensitive one under this translational error.

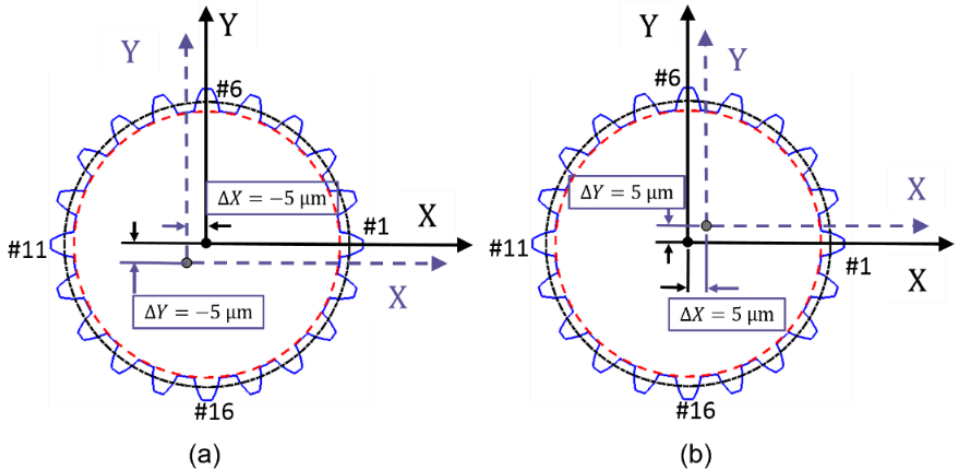

Figure 5.28: Simulated translational error of the origin of the new CSY, relative to the nominal origin of the gear in both the X direction and the Y direction: (a), -5 µm; (b), +5 µm.

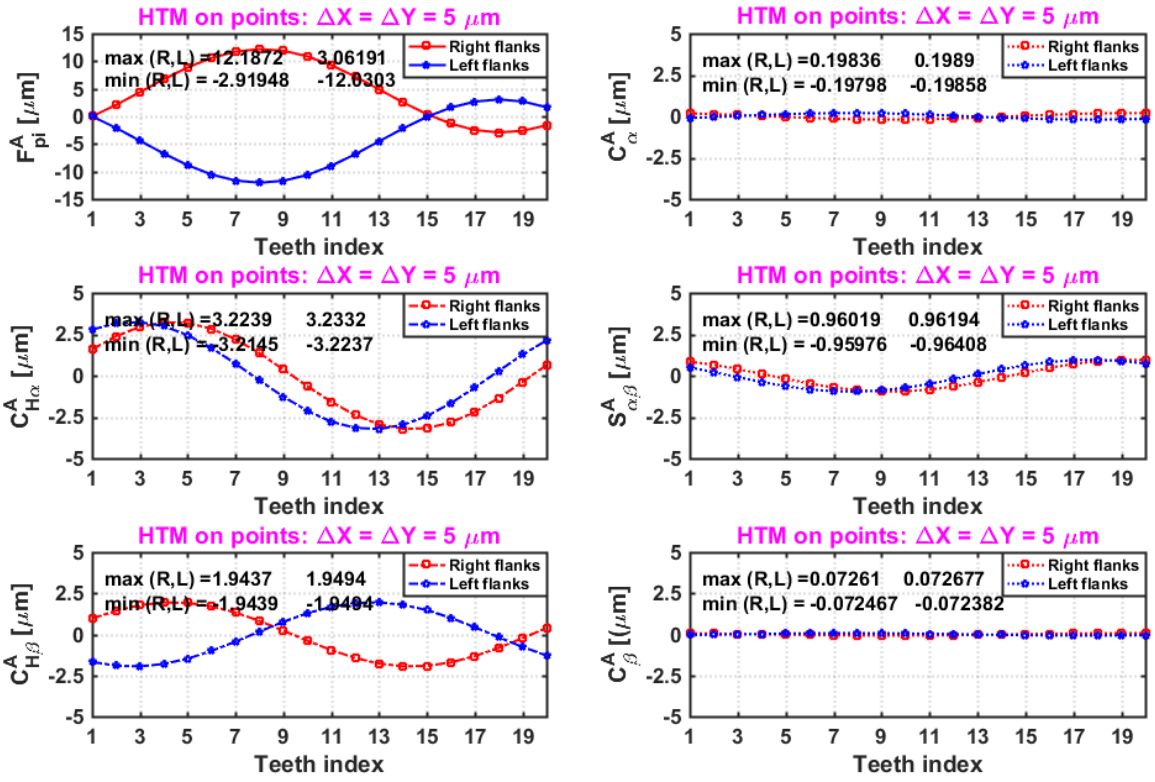

Figure 5.29: Change of areal gear parameters under a HTM of simulated translational error by +5 µm in both the X axis and the Y axis according to Figure 5.28 (a).

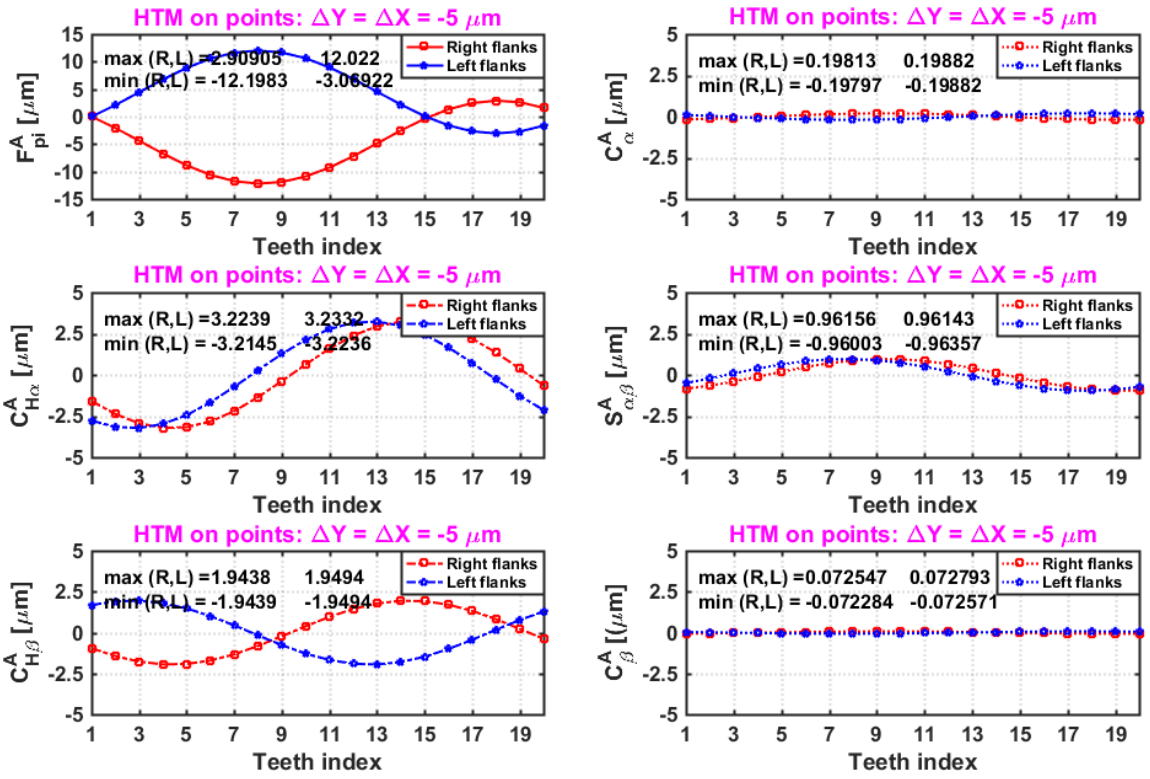

Figure 5.30: Change of areal gear parameters under a HTM of simulated translational error by -5 μm in both the X axis and the Y axis according to Figure 5.28 (b).

Despite its exploratory nature of the three cases above, this study offers several insights into the influence of translational error to the areal gear parameters:

Firstly, the response of the zero order and first order areal parameters (e.g. areal pitch, areal slope) is more significant than the second order areal parameters (e.g. crowning and twists). Thus, the zero order and the first order parameters should be more suitable as indicators for identifying which translational error is present. Secondly, on individual flanks, different areal parameters exhibit different magnitudes and signs under the same translational error. Thus, on all teeth, they collectively show a distinguishable pattern caused by different translational errors.

5.4.2 Areal parameters influenced by rotational errors

Besides the three translational error motions between the nominal coordinate system and the simulated measured coordinate system, there are three rotational error motions, usually referred to as, pitch, roll and yaw in CMM technology. To maintain a consistent description of the coordinate system in this section (i.e. as shown in Figure 5.21), the rotation angle is referred to as "with respect to the X axis", "with respect to the Y axis" and "with respect to the Z axis" instead of pitch, roll and yaw.

5.4.2.1 Rotation of new CSY with respect to the X axis of the nominal CSY by 0.01 degree

The rotational error between CSYs with respect to the X axis is denoted by ϵ_X. Therefore, the corresponding value of ϵ_X in a HTM should have the opposite sign. The calculated areal parameters are shown in Figure 5.31 under the influence of this HTM. Compared to the change of areal cumulative pitch deviations, the areal helix slope parameters, areal profile parameters and the areal flank twist parameters are more significant under the same rotational error.

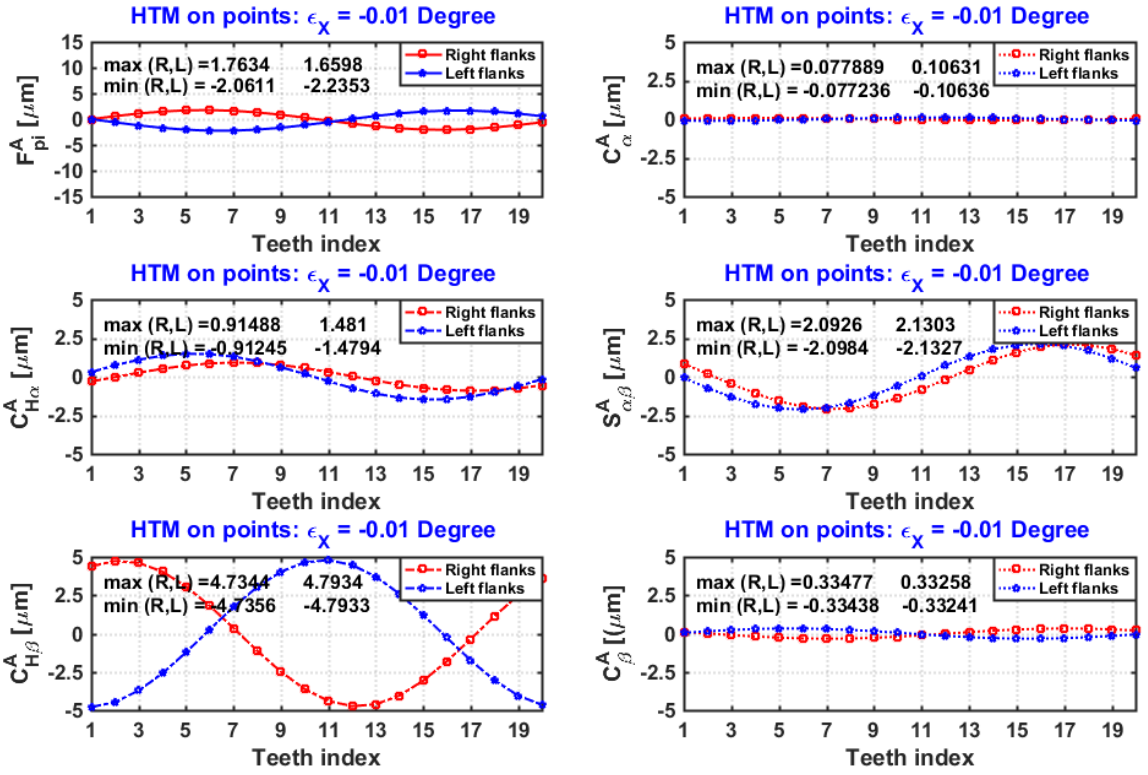

Figure 5.31: Change of areal gear parameters under a HTM of simulated rotational error by -0.01 degree with respect to the X axis.

5.4.2.2 Rotation of new CSY with respect to the Y axis of the nominal CSY by 0.01 degree

The rotational error between two CSYs with respect to the Y axis is denoted by ϵ_Y. Therefore the corresponding value of ϵ_Y in a HTM should have the opposite sign. The calculated areal parameters are shown in Figure 5.32 under the influence of this HTM. Compared to the change of areal cumulative pitch deviations, the areal helix slope parameters, areal profile parameters and the areal flank twist parameters are more significant under the same rotational error.

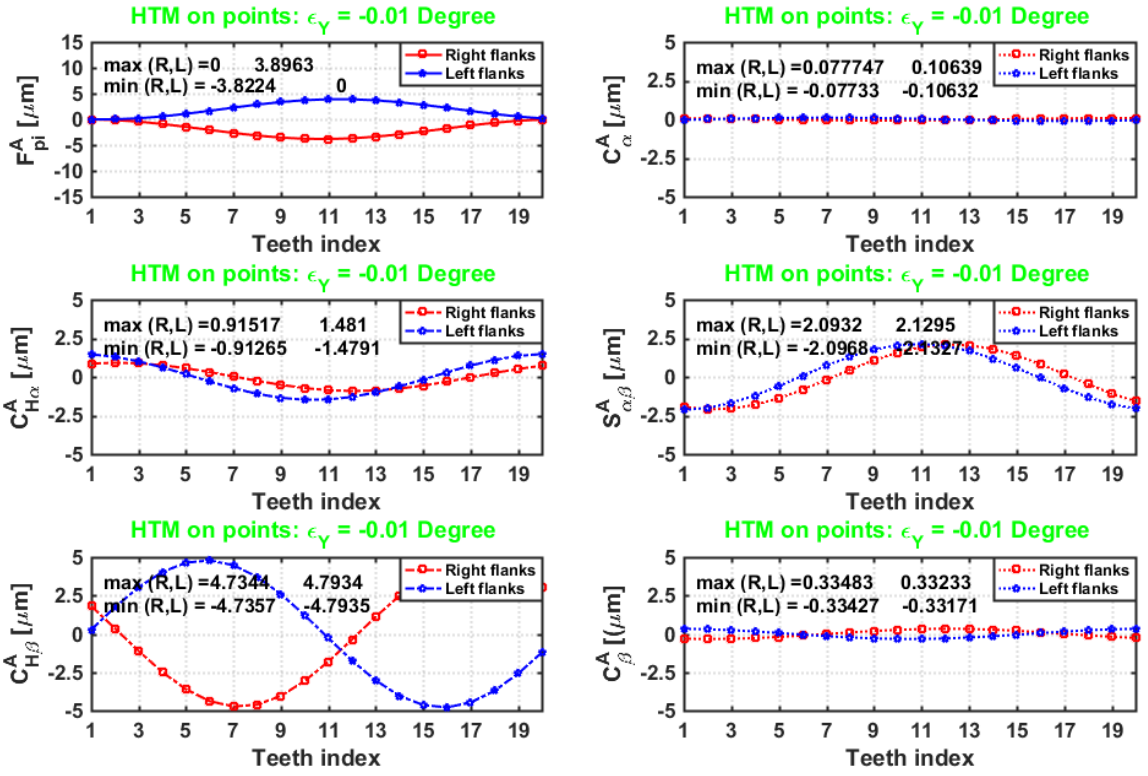

Figure 5.32: Change of areal gear parameters under a HTM of simulated rotational error by -0.01 degree with respect to the Y axis.

The rotational error with respect to the Z axis is not simulated for two reasons: firstly, a complete gear geometry rotation is symmetrical with respect to the gearing axis (usually selected as the Z axis); secondly, when specify the angular location of each tooth and flank, the angular deviation can be treated to the pitch deviations as discussed earlier in this chapter.

No deterministic modeling and compensation method has been investigated in this section. In fact, the dynamic nature of kinematic errors during a measurement process might be too complex to model by first principles, namely a HTM with multiple time-dependent kinematic errors. When prior information about the kinematic errors of an

instrument is available, this study can provide opportunities to characterize the contribution to measurement uncertainty of areal gear parameters from instrument kinematic error. If no prior information is available, this study can be utilized as a tool to measure a calibrated artifact and retrieve the influence of the kinematic errors of an instrument.

CHAPTER 6 : VALIDATION ON GEAR MODIFICATION ARTIFACT

In this chapter, conventional line oriented and areal measurements are carried out to verify the effectiveness of characterizing gear modification by the developed 2D Chebyshev method. Areal parameters evaluated from measured point clouds are compared to the conventional line oriented parameters.

6.1 Conventional measurement of a calibrated modification artifact

A calibrated modification artifact (referred to as "M") manufactured by FRENCO is shown in Figure 6.1 (a). This artifact is an "Identity Condition" artifact, since it is designed and manufactured to have the closest geometry similarity to a helical gear [71]. The basic geometry information of "M" is listed in Figure 6.1 (b). A variety of flank modifications on 28 left flanks and pitch modifications on 3 right flanks are intentionally introduced to this part.

Four modified left flanks on the tooth (referred to as "L#10", "L#19", "L#20" and "L#30") with profile slope, profile crowning, helix slope and helix crowning, respectively, are used in this chapter to verify the effectiveness of the 2D Chebyshev method. The locations of different amplitude and signs of modifications are shown in Figure 6.2.

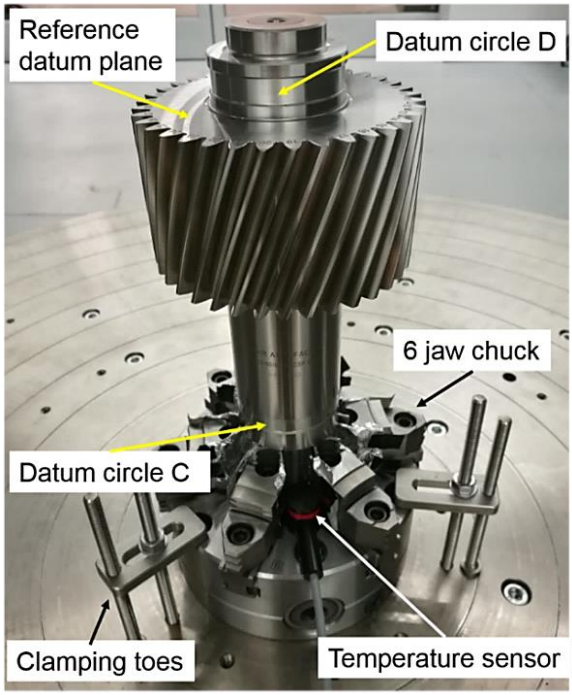

(a)

GEAR ARTEFACT M

Involute		
Number of teeth	Z	36
Module / DP	Mn/DP	3.0000
Pressure angle	PA	20.0000°
Helix angle	HA	20.0000°
Direction of helix	-	Right Hand
Reference diameter	D	114.9312
Base diameter	DB	107.1728
Tip diameter	DA	122.0000 ±0.0500
Tip form diameter	DFA	121.0000
Root form diameter	DFF	109.0000
Root diameter, max	DF	106.5000

Datum axis: C-D		Tolerances for individual errors B - DIN3970
Profile deviation, total	Fα	0.0050
Cumulative pitch deviation, total	Fp	0.0070
Single pitch deviation	fp	0.0025
Runout	Fr	0.0070
Helix deviation, total	Fβ	0.0050

(b)

Figure 6.1: Calibrated gear modification artifact: (a), measurement setup of the artifact "M" on Leitz PMMF; (b), basic geometry information of the artifact "M" [71].

Profile slope modification	Tooth Nr.	fHα, µm
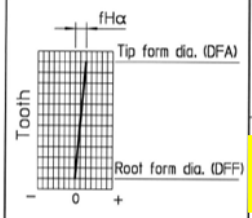	1	-10
	10	+10

Crowning	Tooth Nr.	Cβ, µm
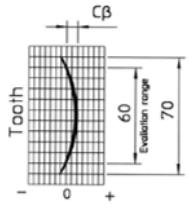	3	0
	12	-20
	21	+5
	30	+10

Helix slope modification	Tooth Nr.	fHβ, µm *
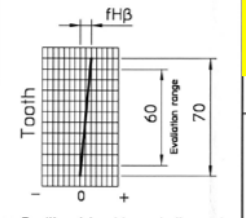	19	-20
	28	+20

* Positive (+) = bigger helix angle

Crowning height	Tooth Nr.	Cα, µm
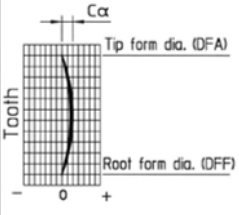	2	0
	11	-5
	20	+5
	29	+10

Figure 6.2: Specifications of slope and crowning modifications on artifact "M" (selected tooth and amount of modifications in yellow box) [71].

The artifact was measured on a gear measuring instrument, which has been calibrated by national masters (involute, helix, pitch and tooth, provided by the PTB) to maintain the traceability of the measurement results claimed in the certificates of "M".

According to the calibration certificate, the intended, measured value and the extended measurement of four flank modifications are summarized in Table 6.1. All measurements were carried out in an environment of temperature of 20 ˚C ± 1 ˚C and a humidity of 50% ± 10%.

Table 6.1: Certificated line oriented evaluation results of four modifications on "M" [71] (unit: μm).

Feature	Intended value	Measured value	Feature form deviation	Extended uncertainty
Profile slope (flank: L#10)	10	10.2	0.9	± 3.0
Helix slope (flank: L#19)	-20	-17.6	0.8	± 3.0
Profile crowning (flank: L#20)	5	5.7	1.7	± 3.0
Helix crowning (flank: L#30)	10	9.5	1.7	± 3.0

6.1.1 Alignment and measurement process on Leitz PMMF302016

The same selected teeth were measured by the CMM without using a rotary table. Two types of measurements including standard measurements (on profile line, one helix line on each flank) and multiple lines (in profile and helix directions) were selected to compare the results by conventional line oriented evaluation with the areal evaluation. A star probe configuration was selected, to ensure the accessibility for the measurement of this artifact on the CMM. The typical probe qualification results are shown in Table 6.2.

Table 6.2: Typical qualification results (stylus sphericity deviation) of an eight-star probe with eight 1.5 mm diameter styli (unit: μm).

Name of stylus	StarPrb(21)	StarPrb(22)	StarPrb(23)	StarPrb(24)
Result	0.8	0.7	0.7	0.7
Name of stylus	StarPrb(25)	StarPrb(26)	StarPrb(27)	StarPrb(28)
Result	0.6	0.9	0.6	0.5

The process of mechanical alignment for a workpiece coordinate system is shown in Figure 6.3 and Figure 6.4. The reference plane was manually probed by four styli with 29 probed points (indicated by the red dots in Quindos 7 graphical interface) in total. These probed points were calculated and evaluated as a plane for $z = 0$. The datum circle "C" and circle "D" were measured and the two calculated center coordinates were used to build the center axis. The origin of the workpiece coordinate system is obtained by intersecting the center axis to the reference plane.

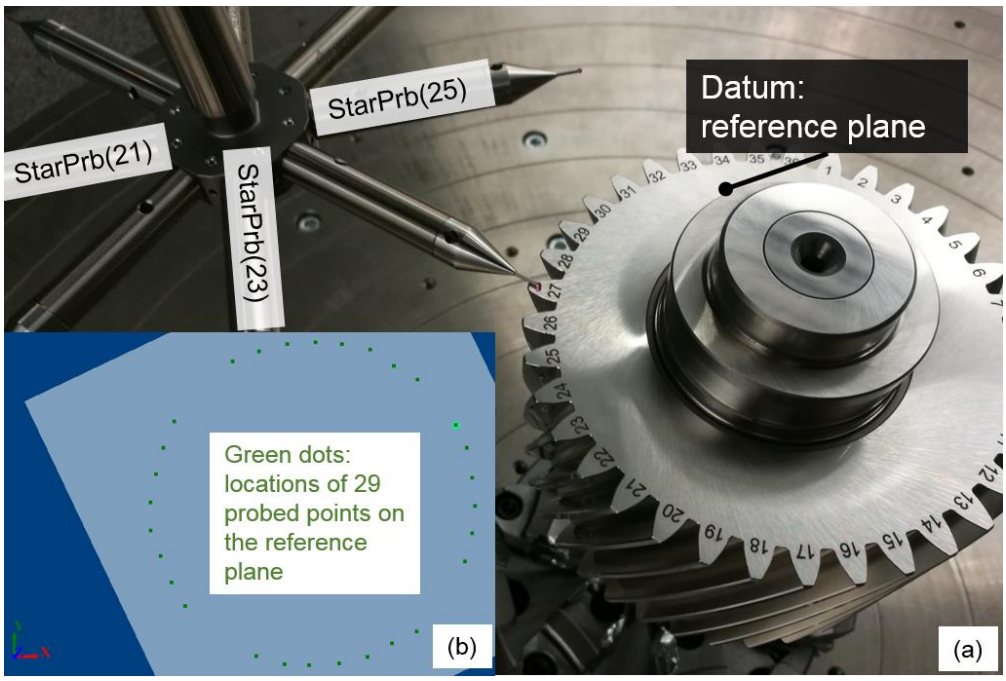

Figure 6.3: Measurement of datum features on the gear artifact using 8-star-probe: (a), measurement of datum reference plane; (b), locations of the probed points.

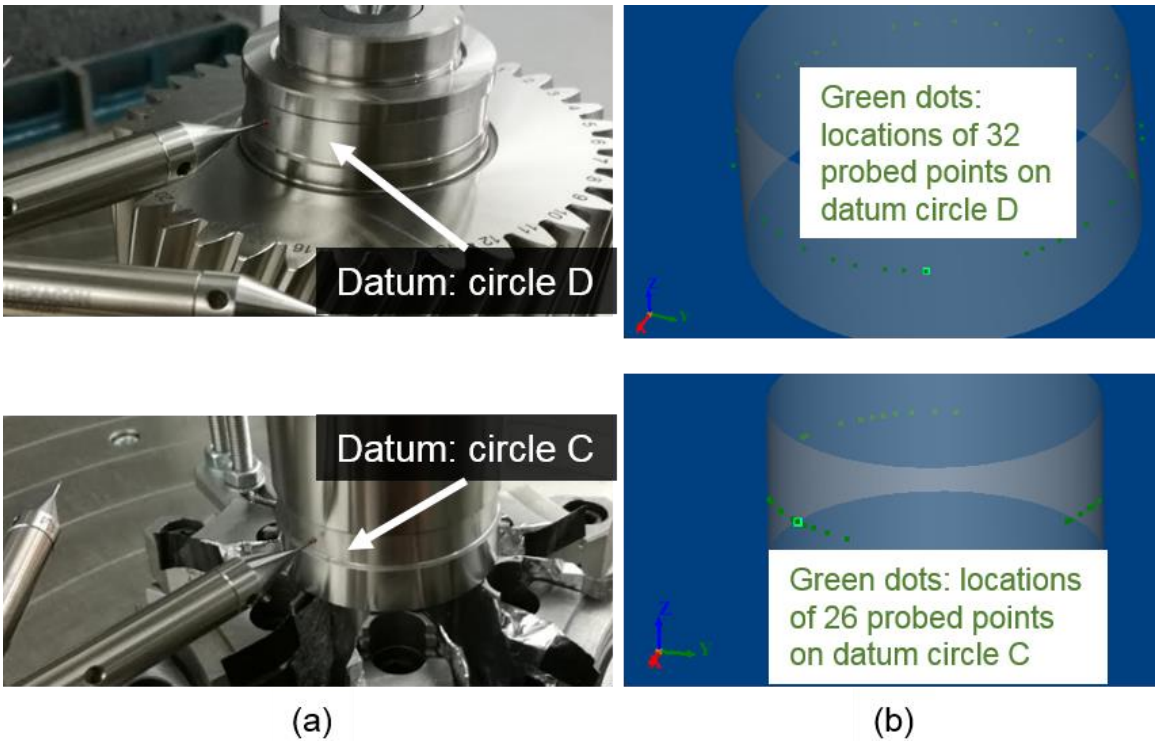

Figure 6.4: Measurement setup for mechanical alignment of artifact "M": (a), probing datum circle C and D on artifact "M"; (b), locations of the probed points.

The "GEAR" measurement function embedded in Quindos 7 with the CMM is developed by Hexagon Manufacturing Intelligence and certificated by PTB for gear evaluation. In the following sections, oriented evaluation results from the CMM is cited without any statement regarding the measurement uncertainty of conventional measurands.

6.1.2 Conventional evaluation on Leitz PMMF302016

Three standard measurements were repeated on artifact "M" by the CMM. The average values listed on the third column of Table 6.3 are calculated based on these three measurement results for each feature. At each repetition, the alignment routine was automatically carried out for building a new workpiece CSY, before the measurement of

gear deviations. The measured values are used as a baseline reference for comparing the areal evaluation of areal measurement data in the next section.

Table 6.3. Standard measurements of modification on artifact "M" measured by the CMM (3 repetitions).

Modification feature	Location of measurement	Average [μm]
Profile slope (L#10)	z = 35 mm	9.9
Helix slope (L#19)	d_M = 114.9312 mm	-17.7
Profile crowning (L#20)	z = 35 mm	5.5
Helix crowning (L#30)	d_M = 114.9312 mm	9.8

6.2 Areal measurement of artifact "M" using Leitz PMMF302016

The certificate provides only one profile and one helix line measured on each flank, therefore no calibrated areal evaluation information is available to support the quality of the entire flank. For this reason, a measurement strategy for capturing areal data of the modified flanks are used. It includes both conventional measurement of multiple profile and helix lines and conventional evaluation of multiple line oriented features.

As shown in Figure 6.5, 99 profile lines (denoted by P1, P2, P3 and P99) and 23 helix lines (denoted by L1, L2 and L23) were measured on both flanks of all teeth. The scanning speed for each line feature (helix and profile) was set to 2 mm/sec. The time spent on measuring 99 profile lines for both left and right flanks on all teeth is 17.9 hours. The time spent on measuring 23 helix lines for both left and right flanks on all teeth is 13.8 hours.

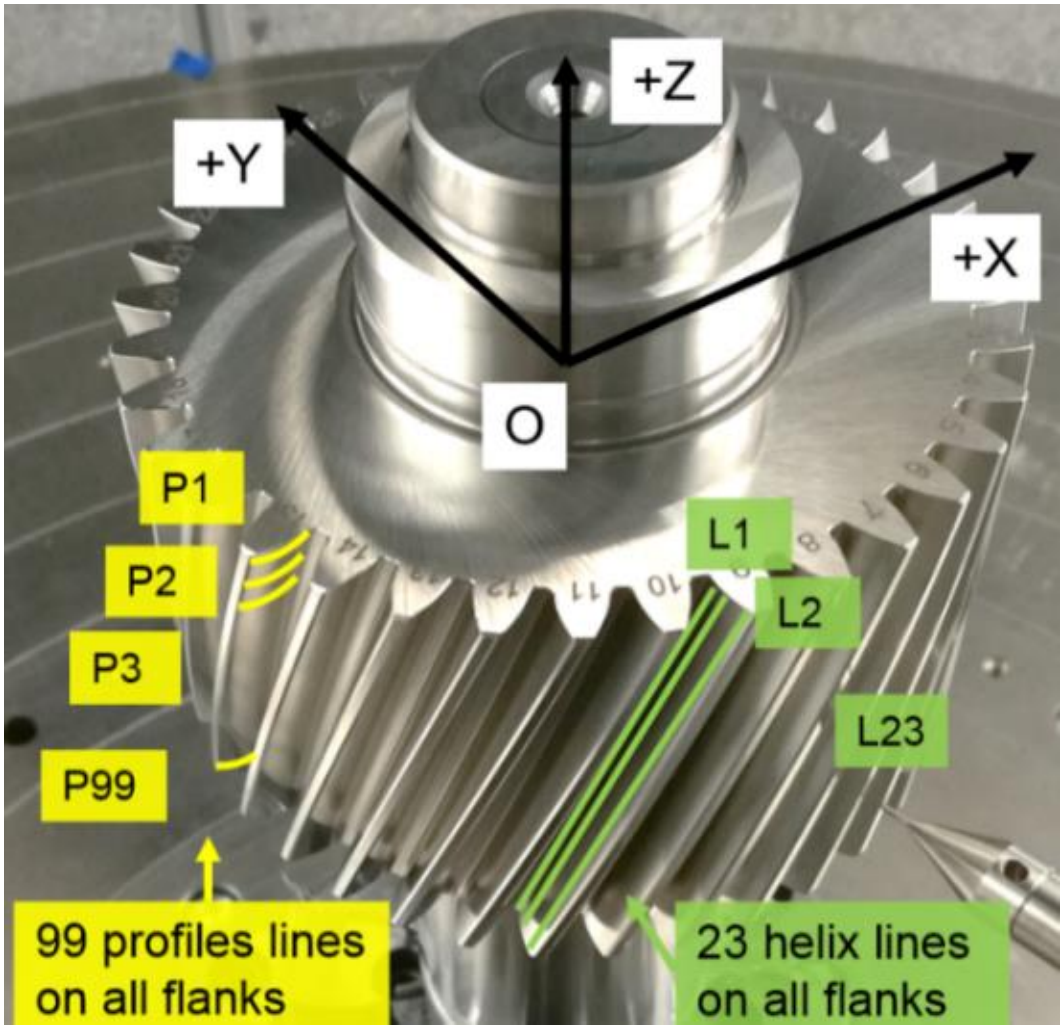

Figure 6.5: Illustration of the workpiece CSY of artifact “M” and the locations of multiple lines on flanks.

For areal evaluation of helix modification, 23 helix lines were measured on the left flanks of tooth #19 and tooth #30. The measured helix lines are distributed with equidistant diameter increments from 109 mm to 121 mm. The average value of each helix feature by conventional evaluation of three repeated measurements are shown in the third column of Table 6.4. The standard deviation calculated from the 23 evaluation results shows the uniformness of a manufactured helix modification across the whole flank.

Table 6.4: Summary of the conventional evaluation of 23 helix lines by Quindos 7 (3 repetitions).

Modification and location	Average of 23 measured helix features [µm]		Standard deviation from 23 measured helix features [µm]	
Helix slope (L#19)	repetition 1	-17.87	repetition 1	0.29
	repetition 2	-17.86	repetition 2	0.30
	repetition 3	-17.88	repetition 3	0.27
Helix crowning (L#30)	repetition 1	9.80	repetition 1	0.21
	repetition 2	9.81	repetition 2	0.20
	repetition 3	9.82	repetition 3	0.21

For areal evaluation of profile modification, 99 profile lines were measured covering the entire helix evaluation range, as shown in Figure 6.5. The measured 99 profile lines are distributed equidistantly from z = -5 mm to z = -65 mm. The average value of each profile feature by conventional evaluation of three repeated measurements are shown in the third column of Table 6.5. The standard deviation calculated from the 99 evaluation results show how uniform the manufactured profile modification is over the whole flank.

Table 6.5: Summary of the conventional evaluation of 99 profile lines by Quindos 7 (3 repetitions).

Modification and location	Average of the 99 evaluated profile features [µm]		Standard deviation of the 99 evaluated profile features [µm]	
Profile slope (L#10)	repetition 1	10.4	repetition 1	0.21
	repetition 2	10.3	repetition 2	0.22
	repetition 3	9.9	repetition 3	0.21
Profile crowning (L #20)	repetition 1	5.5	repetition 1	0.14
	repetition 2	5.5	repetition 2	0.13
	repetition 3	5.9	repetition 3	0.14

6.2.1 Areal evaluation of flank modifications by 2D Chebyshev method

As shown in Figure 6.6, the scanned spatial points of 99 profile lines are used for areal evaluation.

It is worthwhile mentioning that, the coordinates of each measured point used in this areal evaluation are the center coordinates of the sphere on each stylus. No radius correction was applied to the coordinates of those points. The widely used radius correction method for a CMM measured point is carried out in the measured surface normal vector of that point. Since the surface normal vector is the deflection vector of the tactile probe head during probing or scanning, the radius correction is prone to the uncertainty of the numerical values of those vectors. In addition, no digital filtration was applied to those measured coordinates. Therefore, the calculated form deviation can reflect the quality of the raw data quality, collected by the CMM instrument.

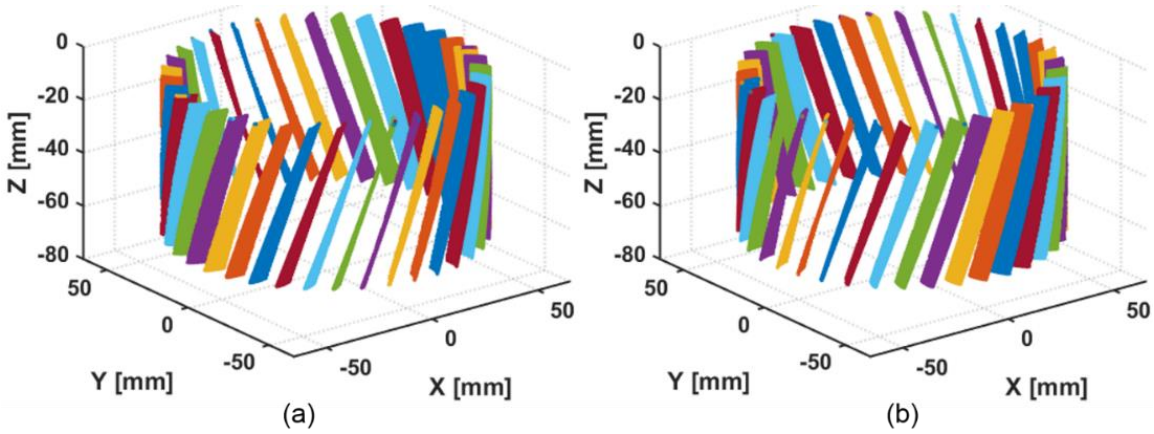

Figure 6.6: Raw data on artifact "M": (a), point cloud of 36 measured left flanks; (b), point cloud of 36 measured right flanks.

The following figures from Figure 6.7 to Figure 6.10 show the 99 profile measurements and areal evaluation results of the four selected left flanks on artifact "M".

Each areal map (for a flank) contains nearly 31280 raw points with all points from the 99 profile lines combined. A blue dot represents the calculated plumb line distance value from each measured point with respect to the pure involute flank. The red dots represent the reconstructed areal map by using the first six terms of 2D Chebyshev coefficients. The green dots are the difference between the areal distance map and the reconstructed map, which is known as the residual map.

The 2D DCT method was used to calculate the 2D Chebyshev coefficients, and the number of iterations for each flank was 9 in this chapter.

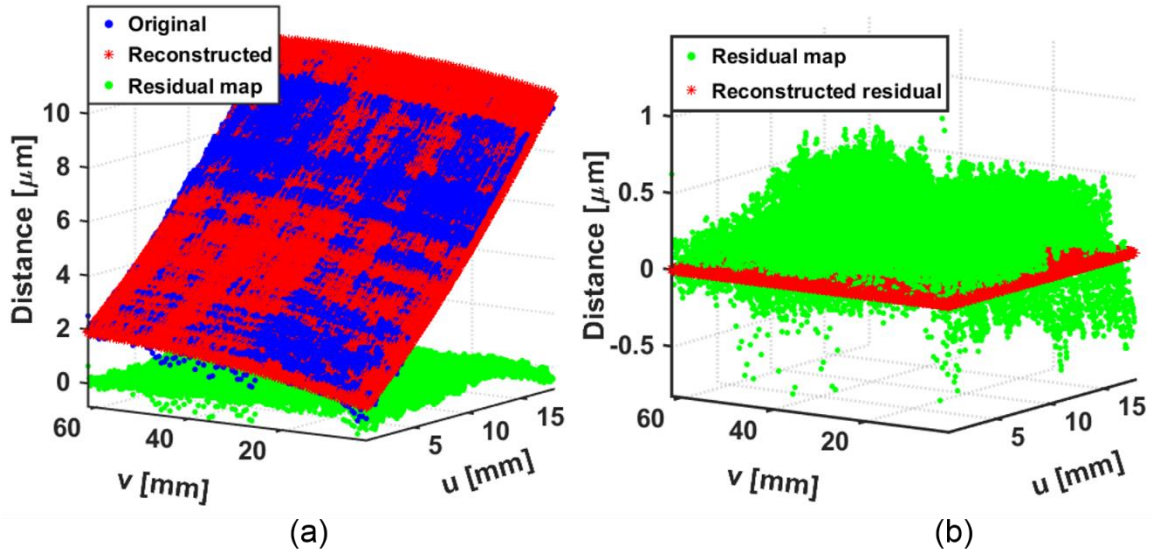

Figure 6.7: Approximation of areal measurement data of L#10 flank; (a), the original (blue), reconstructed (red), and the residual (green) areal maps; (b), the residual map (green) and reconstructed residual map (red).

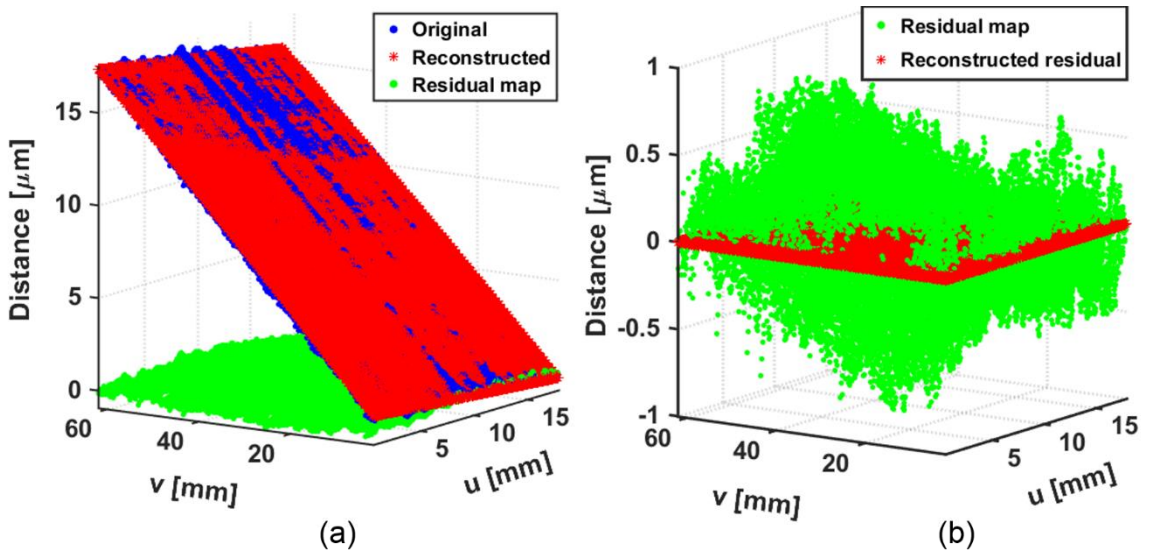

Figure 6.8: Approximation of areal measurement data of L#19 flank; (a), the original (blue), reconstructed (red), and the residual (green) areal maps; (b), the residual map (green) and reconstructed residual map (red).

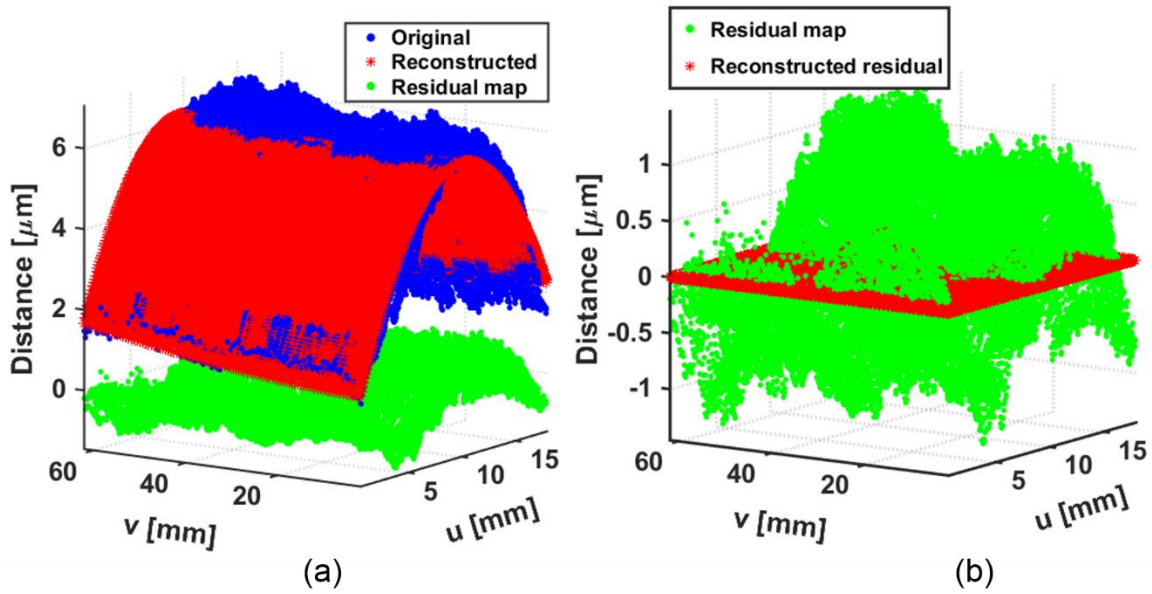

Figure 6.9: Approximation of areal measurement data of L#20 flank; (a), the original (blue), reconspectued (red), and residual (green) areal maps; (b), the residual map (green) and reconstructed residual map (red).

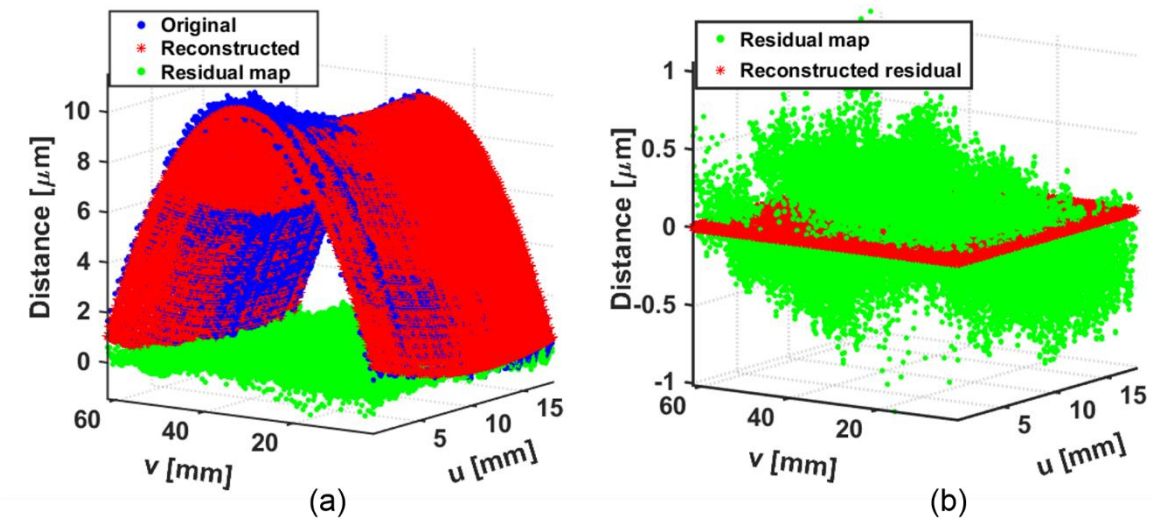

Figure 6.10: Approximation of areal measurement data of L#30 flank; (a), the original (blue), reconstructed (red), and residual areal maps (green); (b), the residual map (green) and the reconstructed residual map (red).

The areal evaluation results for the above four flanks are summarized in Table 6.6. The discrepancy between the areal evaluation using the entire areal point cloud and the averaged value of line oriented evaluation is within ±1.5 μm.

Table 6.6: Comparison of the areal evaluation and the conventional evaluation of the four flank modifications on artifact M.

Feature and location	Areal evaluation [μm]	Conventional evaluation [μm]
Profile slope (L#10)	$C_{\mathrm{H}\alpha}^{\mathrm{A}} = 9.6$	$C_{\mathrm{H}\alpha} = 10.3$
Helix slope (L#19)	$C_{\mathrm{H}\beta}^{\mathrm{A}} = -17.3$	$C_{\mathrm{H}\beta} = -17.9$
Profile crowning (L#20)	$C_{\alpha}^{\mathrm{A}} = 4.6$	$C_{\alpha} = 5.7$
Helix crowning (L#30)	$C_{\beta}^{\mathrm{A}} = 10.9$	$C_{\beta} = 9.8$

The areal form deviation, denoted by $f_{\mathrm{f}}^{\mathrm{A}}$, is calculated as the peak-to-valley value from the residual map from Figure 6.7 to Figure 6.10. In fact, this peak-to-valley value is

notoriously sensitive to extreme values caused by instrument noise or dust on surface, given the fact that 31280 points are used in evaluation. The obtained form deviations, namely the peak to valley distance of the residual map after a certain modification is removed, for the measured areal features on the flanks are all below 3 μm, which is reasonable for such a measurement, conducted on the Leitz PMMF302016 CMM.

Table 6.7 summarizes both areal and conventional evaluation results of the form deviations measured on the modification features. The obtained areal form deviations are larger than their counterparts obtained by conventional evaluation. This is a reasonable phenomenon since the conventional evaluation is based on just one line oriented feature on the entire flank.

Table 6.7: Comparison of the areal evaluation the conventional evaluation of form deviation of the four flank modifications on artifact M.

Feature and location	Areal evaluation [μm]	Conventional evaluation [μm]
Profile slope (L#10)	$f_f^A = 2.1$	$f_{f\alpha} = 0.9$
Helix slope (L#19)	$f_f^A = 1.7$	$f_{f\beta} = 1.2$
Profile crowning (L#20)	$f_f^A = 2.9$	$f_{f\alpha} = 2.1$
Helix crowning (L#30)	$f_f^A = 2.1$	$f_{f\beta} = 1.3$

6.2.2 Evaluation of pitch modifications

The 2D Chebyshev method has also been tested on pitch modifications. As shown Figure 6.12 (a), three pitch modifications are introduced to the right flanks of tooth #30, tooth #31 and tooth #32 respectively. The modified pitch on those three teeth leads to the graphical representation of individual single pitch deviation and individual cumulative pitch shown in Figure 6.12 (b) and (c).

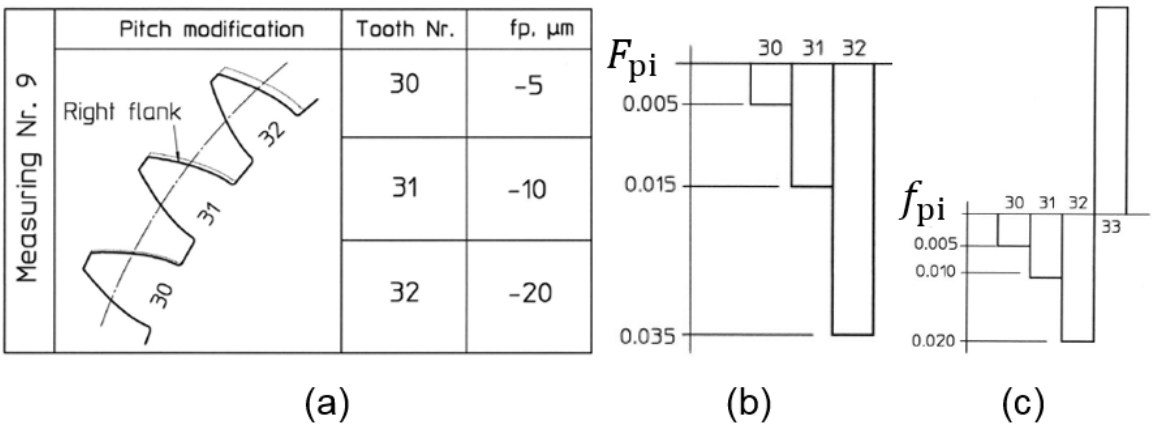

Figure 6.11: Intended pitch modications of artifact "M": (a), location of modifications on the right flanks of tooth #30, #31 and #32; (b), graphical representation of nominal individual cumulative pitch deviation; (c), graphical representation of nominal individual single pitch deviation [71].

In the following discussion, the measurement diameter for evaluating pitch deviation is d_M = 115.769 mm. This value is used for programming conventional point oriented pitch measurement on two tactile instruments and for calculating the areal pitch deviations by the 2D Chebyshev method. Besides the above graphical representation, in conventional pitch evaluation standards, two parameters are used to characterize the pitch deviations for classification of gear quality.

The total cumulative pitch deviation is defined as the difference between the maximum and minimum value of F_{pi}:

$$F_p = \max(F_{pi}) - \min(F_{pi}). \tag{5.21}$$

The total single pitch deviation is defined as the maximum absolute value of f_{pi}:

$$f_p = \max(|f_{pi}|). \tag{5.22}$$

The pitch evaluation results from the measurement certificate are shown in Figure 6.12 and the two pitch deviation parameters in Table 6.8. The claimed measurement uncertainty is ± 3 µm [71].

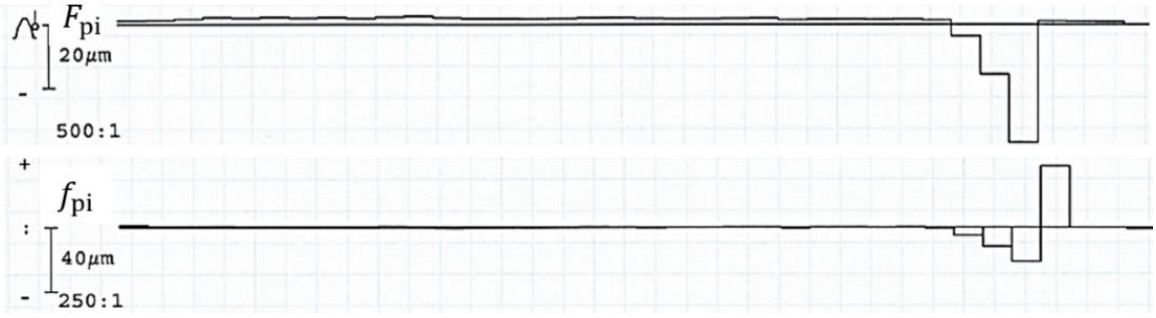

Figure 6.12: Conventional pitch deviations from certificate issued by FRENCO [71]: individual cumulative pitch deviation (top); individual single pitch deviation (bottom).

Table 6.8: Pitch deviations from certificate issued by FRENCO [71] (unit: µm).

Parameter	Intended	Manufacturing tolerance	Evaluation result	Measurement uncertainty
Total cumulative pitch deviation	$F_p = 35$	± 7.0	$F_p = 39.5$	± 3.0
Total single pitch deviation	$f_p = 35$	± 2.5	$f_p = 38.0$	± 3.0

The graphical representation of conventional pitch evaluation from the Leitz PMMF302016 is shown in Figure 6.13. The corresponding values of the total single pitch deviation and the total cumulative pitch deviation are given in the first column of Table 6.9.

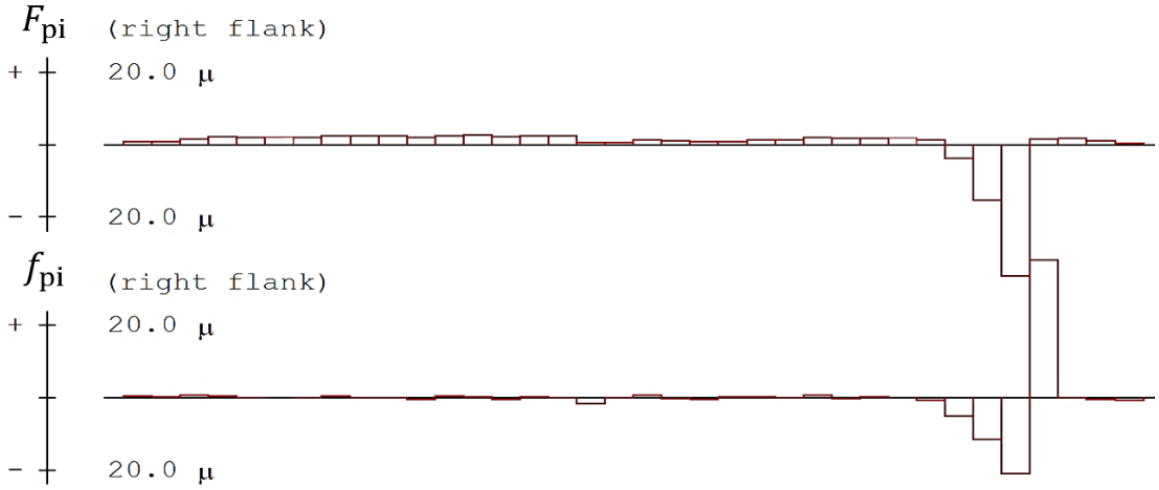

Figure 6.13: Conventional pitch deviations measured by Leitz PMMF302012: individual cumulative pitch deviation (top); individual single pitch deviation (bottom).

The graphical results of areal pitch evaluation by 2D Chebyshev method are shown in Figure 6.14. The raw data used in the evaluation was the same scanned 99 profile lines.

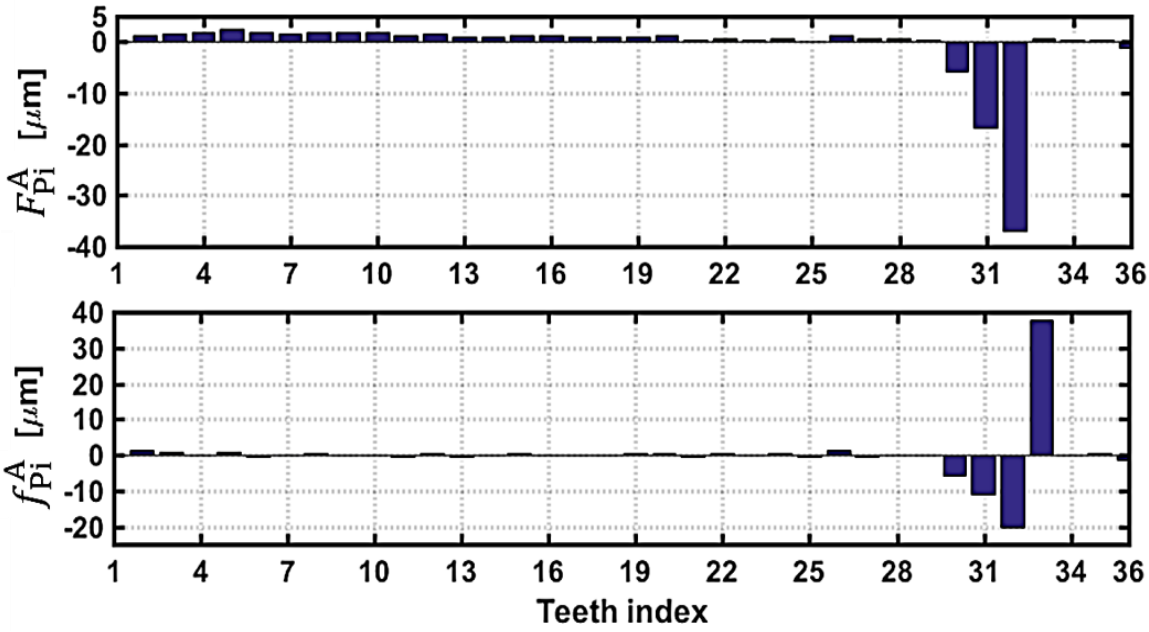

Figure 6.14: Areal pitch deviations calculated by the 2D Chebyshev method from areal measurement point clouds: areal individual cumulative pitch deviation (top); areal individual single pitch deviation (bottom).

Table 6.9: Comparison of conventional pitch deviations and areal pitch deviations measured by Leitz PMMF302016 from 3 repetitions (unit: μm).

Parameter	Conventional (average)	Areal (average)
Total cumulative pitch deviation	$F_p = 39.2$	$F_p^A = 39.0$
Total single pitch deviation	$f_p = 38$	$f_p^A = 37.7$

All three reported measurement results for the two pitch deviation parameters (conventional and areal) are within the agreement of ± 0.5 μm. This agreement confirms the effectiveness of the 2D Chebyshev method for areal pitch evaluations.

In addition, Table 6.10 and Table 6.11 list values of the areal individual cumulative pitch and the areal individual single pitch deviation plotted in Figure 6.14. The bolded "#1" means the right flank of tooth #1 and the value below is the areal pitch parameters on the flank.

Table 6.10: Areal individual cumulative pitch deviations (F_{pi}^A) of the 36 right flanks (tooth #1 to #36) of "M" (unit: μm; value rounded to two digits after the decimal point).

#1	**#2**	**#3**	**#4**	**#5**	**#6**	**#7**	**#8**	**#9**	**#10**	**#11**	**#12**
0	1.12	1.62	1.65	2.28	1.74	1.47	1.88	1.64	1.65	1.15	1.45
#13	**#14**	**#15**	**#16**	**#17**	**#18**	**#19**	**#20**	**#21**	**#22**	**#23**	**#24**
0.90	0.91	1.18	1.04	1.00	0.85	0.91	1.13	0.41	0.50	0.18	0.44
#25	**#26**	**#27**	**#28**	**#29**	**#30**	**#31**	**#32**	**#33**	**#34**	**#35**	**#36**
0.00	1.14	0.67	0.44	0.31	-5.72	-16.8	-37.2	0.48	0.27	0.36	-1.21

Table 6.11: Areal individual single pitch deviations ($f_{\mathrm{pi}}^{\mathrm{A}}$) of the 36 right flanks (tooth #1 to #36) of "M" (unit: μm; value rounded to two digits after the decimal point).

#1	**#2**	**#3**	**#4**	**#5**	**#6**	**#7**	**#8**	**#9**	**#10**	**#11**	**#12**
0	1.12	0.5	0.03	0.63	-0.54	-0.27	0.41	-0.24	0.01	-0.51	0.31
#13	**#14**	**#15**	**#16**	**#17**	**#18**	**#19**	**#20**	**#21**	**#22**	**#23**	**#24**
-0.55	0.01	0.27	-0.14	-0.04	-0.15	0.06	0.22	-0.72	0.09	-0.32	0.27
#25	**#26**	**#27**	**#28**	**#29**	**#30**	**#31**	**#32**	**#33**	**#34**	**#35**	**#36**
-0.45	1.15	-0.47	-0.24	-0.12	-6.03	-11.0	-20.4	37.7	-0.22	0.09	-1.57

Equation (5.23) gives the summation of the areal individual single pitch deviation:

$$\delta_{f_{\mathrm{pi}}}^{\mathrm{A}} = \sum_{\mathrm{i}=1}^{\mathrm{z}} f_{\mathrm{pi}}^{\mathrm{A}} = -1.21\,(\mu\mathrm{m})\,, \tag{5.23}$$

where a new parameter denoted by $\delta_{f_{\mathrm{pi}}}^{\mathrm{A}}$ is defined as a measure of the evaluation results of areal single pitch deviations. Compared to the theoretical value of the summation (i.e. zero) as mentioned in Section 2.4.2, the obtained value -1.21 μm is reasonable, given the number of teeth of this artifact. This value might also be used as a quality measure for areal pitch evaluation in the future.

In addition, other areal parameters of 36 right flanks can be evaluated from the same point clouds in Figure 6.6 (b). The values of deviation on each flank are given in Figure 6.15 and Figure 6.16 for the first order parameters and second order parameters respectively. Since no modifications are designed on the other 33 right flanks, the value obtained might provide potential applications to correlate mechanical misalignment to the obtained areal flank parameters.

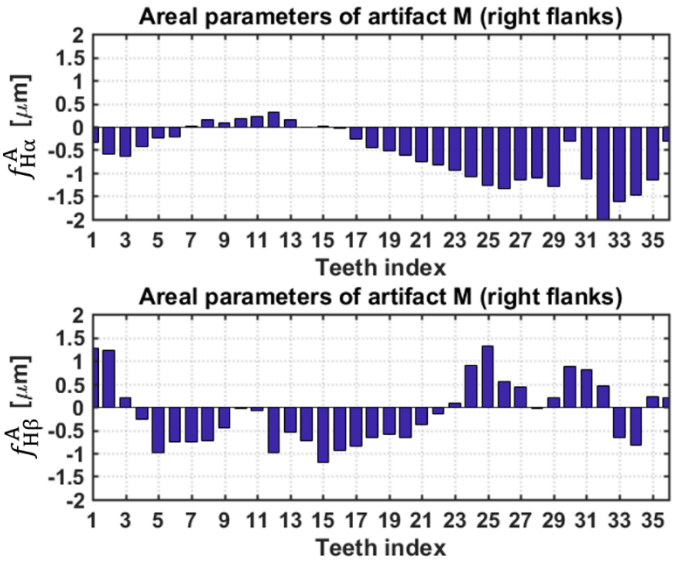

Figure 6.15: First order areal parameters of 36 right flanks: areal profile slope deviations (top); areal helix slope deviations (bottom).

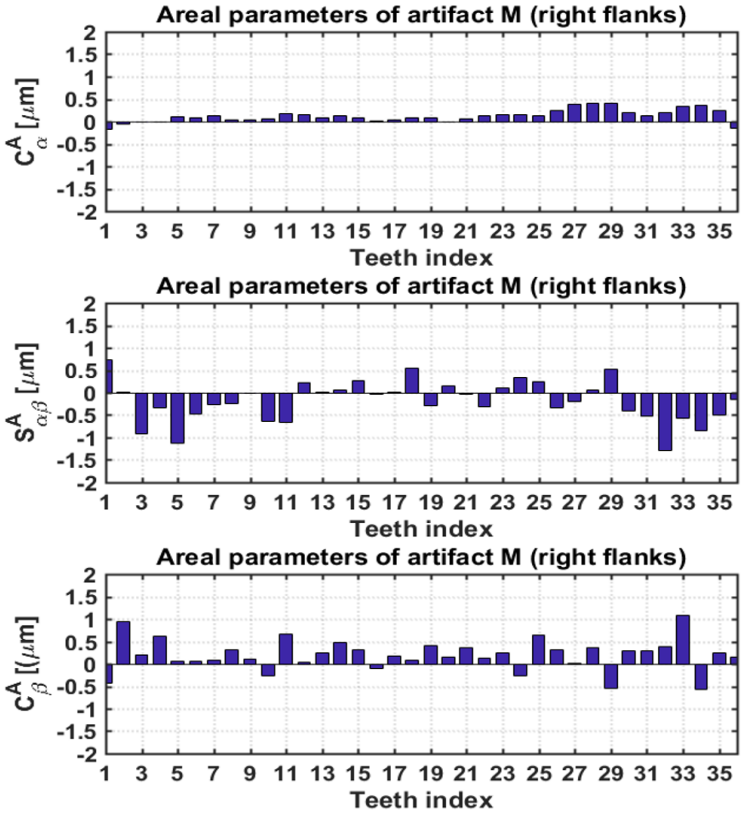

Figure 6.16: Second order areal parameters of 36 right flanks: areal profile crowning (top); areal flank twist (middle); areal helix crowning (bottom).

CHAPTER 7 : CONCLUSIONS AND FUTURE WORK

7.1 Conclusions

In summary, this dissertation provides a foundation for a paradigm change of gear inspection technology. Based on the plumb line distance equation, a 3D geometric model of a cylindrical gear is derived and interpreted as the nominal implicit formula for the complete gear geometry including both flanks of all teeth. An areal distance map is defined as the aggregation of the evaluated plumb line distances evaluated from the measured point clouds within the zone of evaluation. Collectively, the calculated areal distance maps contain all geometric deviations and/or modifications of the gear, including individual flank deviations (both profile and helix directions) and tooth-to-tooth deviations (e.g. pitch deviation). A new set of areal gear parameters is developed to characterize those information, which offers a new mathematical tool for quantitative assessment of gear flank topography.

2D Chebyshev polynomials defined on a square domain, are first recognized to possess geometric similarity to the shapes of low order flank modifications. The flank analysis method based on orthogonal decomposition and using the 2D Chebyshev polynomials (i.e. as base functions) is proposed as a tool, which uniquely links the 2D Chebyshev coefficients and the low order areal gear modification and/or deviation parameters. Three algorithms for evaluating the 2D Chebyshev polynomials have been proposed and compared with simulated flank data with a variety of spatial distributions and point density on the flank. The 2D DCT algorithm is preferred as the implementation algorithm for the method, in terms of fast computation speed among all types of points distributions. Several factors influencing the outcome of the areal gear parameters are

identified and investigated, such as the non-orthogonality of the pixelated data sets, the evaluation of sub-flank data and misalignment related issues. Improvement of computation performance includes, but is not limited to, an increasing point density on the flank, and using random distribution of spatial points on the flank.

A gear modification artifact with certificated measurement uncertainty for several line oriented gear parameters is used to verify the effectiveness of the 2D Chebyshev method. A multiple line scanning strategy that collects spatial data covering the entire flank surface is carried out using a Leitz PMMF302016 CMM. The 2D Chebyshev method can extract simultaneously four areal flank modification parameters and two areal pitch deviation parameters from the measured point clouds. The agreement between corresponding areal and line oriented parameters based on conventional and areal evaluation is within the range of ± 1.5 μm.

7.2 Future work

While the potential of applying the 2D Chebyshev method for areal gear metrology is promising, there are still several important topics that need to be investigated thoroughly.

7.2.1 Uncertainty analysis

First and foremost, a new scheme for estimating the areal measurement uncertainty is needed for area oriented evaluation. Compared to the well-established measurement process by either CMMs or GMIs, areal measurement lacks a guideline to estimate the measurement uncertainty of areal gear parameters. Methods such as Monte Carlo might be suitable for estimating the areal measurement uncertainty given the high point density available.

7.2.2 Holistic evaluation

Another important investigation should be focused on a holistic evaluation scheme based on the areal evaluation method. For example, one aspect of a holistic evaluation is to investigate the applicability of using information from individual areal distance map (of all flanks) to represent the quality of the gear. Beyond the low order information on the flank that can be represented by the first six 2D Chebyshev terms, other spatial frequency components such as waviness and roughness could also be extracted from in the residual map after removing the low order terms. Numerous mathematical tools such as Fourier analysis, structure function and wavelet decomposition are readily available for analyzing those types of surface information of gear flanks.

In addition, flank information on different teeth may leave a signature caused by a specific manufacturing process deviation, which differs from tooth to tooth, such as the motion control errors, tool wear of the cutter and localized temperature variation on a gear. Flank information present uniformly on all teeth might indicate a global tendency of the manufacturing process variation, for example the deviation of tool geometry and misalignment of tool to workpiece. Thus, with this strategic classification of flank information, correlation could be established for better understanding of a manufacturing process.

7.2.3 Function oriented analysis

Lastly, with the completion of both individual and global information of a gear, its interaction with a mating gear might be assessed with the help of tools like tooth contact analysis. Thus, with more quantitative areal information, the correlation between gear pair

functional performance such as transmission error, noise emission and failure rate might be better estimated.

REFERENCES

[1] F. Litvin and A. Fuentes, *Gear Geometry and Applied Theory*, 2nd ed. Cambridge University Press, 2004.

[2] G. Goch, "Gear Metrology," *CIRP Annals - Manufacturing Technology*, vol. 52, no. 2, pp. 659–695, 2003.

[3] K. D. Bouzakis, E. Lili, N. Michailidis, and O. Friderikos, "Manufacturing of cylindrical gears by generating cutting processes: A critical synthesis of analysis methods," *CIRP Annals - Manufacturing Technology*, vol. 57, no. 2, pp. 676–696, 2008.

[4] B. Karpuschewski, H. J. Knoche, and M. Hipke, "Gear finishing by abrasive processes," *CIRP Annals - Manufacturing Technology*, vol. 57, no. 2, pp. 621–640, 2008.

[5] C. Heinzel and A. Wagner, "Fine finishing of gears with high shape accuracy," *CIRP Annals - Manufacturing Technology*, vol. 62, no. 1, pp. 359–362, 2013.

[6] K. Erkorkmaz, A. Katz, Y. Hosseinkhani, D. Plakhotnik, M. Stautner, and F. Ismail, "Chip geometry and cutting forces in gear shaping," *CIRP Annals - Manufacturing Technology*, vol. 65, no. 1, pp. 133–136, 2016.

[7] E. Savio, L. De Chiffre, S. Carmignato, and J. Meinertz, "Economic benefits of metrology in manufacturing," *CIRP Annals - Manufacturing Technology*, vol. 65, no. 1, pp. 495–498, 2016.

[8] H. Kunzmann, T. Pfeifer, and R. Schmitt, "Productive metrology-Adding value to manufacture," *CIRP Annals- Manufacturing Technology*, vol. 54, no. 1, pp. 155–168, 2005.

[9] G. Goch, K. Ni, Y. Peng, and A. Guenther, "Future gear metrology based on areal measurements and improved holistic evaluations," *CIRP Annals - Manufacturing Technology*, vol. 66, no. 1, pp. 469–474, 2017.

[10] W. Lotze and F. Haertig, "3D gear measurement by CMM," *Laser Metrology & Machine Performance V*, vol. 34, pp. 333–344, 2001.

[11] W. Lotze, "General solution for Tsebyshev approximation of form elements in coordinate measurement," *Measurement*, vol. 12, no. 4, pp. 337–344, 1994.

[12] T. Pfeifer, S. Kurokawa, and S. Meyer, "Derivation of parameters of global form deviations for 3-dimensional surfaces in actual manufacturing processes," *Measurement: Journal of the International Measurement Confederation*, vol. 29, no. 3, pp. 179–200, 2001.

[13] J. Y. Dantan, J. Bruyere, C. Baudouin, and L. Mathieu, “Geometrical Specification Model for Gear - Expression, Metrology and Analysis,” *CIRP Annals - Manufacturing Technology*, vol. 56, no. 1, pp. 517–520, 2007.

[14] J. Y. Dantan, J. P. Vincent, G. Goch, and L. Mathieu, “Correlation uncertainty - Application to gear conformity,” *CIRP Annals - Manufacturing Technology*, vol. 59, no. 1, pp. 509–512, 2010.

[15] ISO, “Gears - Cylindrical involute gears and gear pairs - Concepts and geometry,” vol. 21771. 2007.

[16] A. Guenther, “Flaechenhafte Beschreibung und Ausrichtung von Zylinderraedern mit Evolventenprofil,” Universitaet Ulm, 1996.

[17] G. Goch, W. Knapp, and F. Härtig, “Precision engineering for wind energy systems,” *CIRP Annals - Manufacturing Technology*, vol. 61, no. 2, pp. 611–634, Jan. 2012.

[18] ISO, *ISO 1328:1-2013: Cylindrical Gears - ISO System of Flank Tolerance Classification - Part 1 : Definitions and Allowable Values of Deviations Relevant to Flanks of Gear Teeth*. 2013.

[19] VDI, “Pitch and runout testing on gearings Cylindrical gears, wormwheels, bevel gears.” 2003.

[20] VDI, “Computer-aided evaluation of profile and helix measurements on cylindrical gears with involute profile.” 2000.

[21] J. Tang, J. Jia, Z. Fang, and Z. Shi, “Development of a gear measuring device using DFRP method,” *Precision Engineering*, vol. 45, pp. 153–159, 2016.

[22] B. Xu, Y. Shimizu, S. Ito, and W. Gao, “Pitch deviation measurement of an involute spur gear by a rotary profiling system,” *Precision Engineering*, vol. 39, pp. 152–160, 2015.

[23] F. Härtig, H. Lin, K. Kniel, and Z. Shi, “Standard conforming involute gear metrology using an articulated arm coordinate measuring system,” *Measurement Science and Technology*, vol. 23, no. 10, p. 105011, 2012.

[24] F. Klocke, E. Brinksmeier, and K. Weinert, “Capability Profile of Hard Cutting and Grinding Processes,” *CIRP Annals - Manufacturing Technology*, vol. 54, no. 2, pp. 22–45, 2005.

[25] I. G. Artifacts and T. Protocol, “Physikalisch – Technische Bundesanstalt EURAMET Intercomparison Involute Gear Artifacts Technical Protocol,” pp. 1–25, 2013.

[26] T. Pfeifer and G. Spur, “Task-Specific Gauge for the Inspection of Coordinate Measuring Machines,” *CIRP Annals - Manufacturing Technology*, vol. 43, no. 1, pp.

465–468, 1994.

[27] M. Komori *et al.*, “Evaluation method of lead measurement accuracy of gears using a wedge artefact,” *Measurement Science and Technology*, vol. 20, no. 2, p. 25109, 2009.

[28] Y. Kondo *et al.*, “Evaluation of instruments for helix measurement using wedge artifact,” *Precision Engineering*, vol. 34, no. 4, pp. 667–674, 2010.

[29] Y. Kondo, K. Sasajima, S. Osawa, O. Sato, and M. Komori, “Traceability strategy for gear-pitch-measuring instruments: development and calibration of a multiball artifact,” *Measurement Science and Technology*, vol. 20, no. 6, p. 65101, 2009.

[30] A. Guenther, K. Kniel, F. Härtig, and I. Lindner, “Introduction of a new bevel gear measurement standard,” *CIRP Annals - Manufacturing Technology*, vol. 62, no. 1, pp. 515–518, 2013.

[31] G. Lanza and B. Viering, “A novel standard for the experimental estimation of the uncertainty of measurement for micro gear measurements,” *CIRP Annals - Manufacturing Technology*, vol. 60, no. 1, pp. 543–546, 2011.

[32] F. Balzer *et al.*, “Recent advances in optical gear measurements A new approach for fast measurements of large gears Bremen Institute for Metrology , Automation and Quality Science (BIMAQ), University of Bremen,” pp. 1–11.

[33] G. Lanza, B. Haefner, and P. Science, “Areal Characterization of Micro Gears By Means of Computed Tomography,” pp. 11–14, 2013.

[34] FRENCO, “Gear Flank Analyzer,” 2016. .

[35] R. J. Hocken, N. Chakraborty, C. Brown, and N. Carolina, “Optical Metrology of Surfaces,” vol. 1, no. 1.

[36] F. Takeoka *et al.*, “Design of Laser Interferometric Measuring Device of Involute Profile,” *Journal of Mechanical Design*, vol. 130, no. 5, p. 52602, 2008.

[37] G. Lu, S. Wu, N. Palmer, and H. Liu, “Application of Phase Shift Optical Triangulation to Precision Gear Gauging,” vol. 3520, no. November, pp. 52–63, 1998.

[38] J. Peters, G. Goch, and A. Günther, “Helical gear measurement using structured light,” *Proceedings of the XVI IMEKO World Congress*, pp. 2–5, 2000.

[39] S. Fang, L. Wang, M. Komori, and A. Kubo, “Simulation method for interference fringe patterns in measuring gear tooth flanks by laser interferometry.,” *Applied optics*, vol. 49, no. 33, pp. 6409–15, 2010.

[40] S. Fang, L. Wang, P. Yang, L. Meng, M. Komori, and A. Kubo, “Improvement of

the oblique-incidence optical interferometric system to measure tooth flanks of involute helical gears," *Journal of the Optical Society of America A*, vol. 28, no. 4, p. 590, 2011.

[41] S. Fang, X. Zhu, P. Yang, Q. Cai, M. Komori, and A. Kubo, "Affect of interference fringe width for processing accuracy and its recognition in measuring form deviation of tooth flank with laser interferometry," *Optics Communications*, vol. 328, pp. 49–56, 2014.

[42] MS3D, "3D INSPECTION OF GEAR." [Online]. Available: http://www.ms3d.eu/en/our-machines/3d-inspection-of-gear-gearinspection/.

[43] Nikon, "HN-C3030." [Online]. Available: https://www.nikonmetrology.com/images/brochures/hn-c3030-en.pdf.

[44] Gleason, "300GMSL Multi-Sensor Inspection Machine." [Online]. Available: http://www.gleason.com/en/news/472/300gmsl-multi-sensor-inspection-machine.

[45] D. Stöbener, A. Von Freyberg, M. Fuhrmann, and G. Goch, "Areal parameters for the characterisation of gear distortions," *Materialwissenschaft und Werkstofftechnik*, vol. 43, no. 1–2, pp. 120–124, 2012.

[46] A. Günther *et al.*, "Einsatz von Koordinatenmessgeräten (KMG) an Großverzahnungen," in *VDI Fachtagung Koordinaten messtechnik*, 2014, p. 16.

[47] M. E. Mortenson, *Geometric Modeling*, 3rd ed. Industrial Press Inc., 2006.

[48] G. Goch, "Algorithm for the Combined Approximation of Continuously Differentiable Profiles Composed of Straight Lines and Circle Segments," vol. 40, pp. 7–10, 1991.

[49] G. Goch, U. Tschudi, and J. Pettavel, "A Universal Algorithm for the Alignment of Sculptured Surfaces," *CIRP Annals - Manufacturing Technology*, vol. 41, no. 1, pp. 597–600, 1992.

[50] L. Trefethen, *Approximation Theory and Approximation Practice*. 2013.

[51] G. T. Anthony *et al.*, "Reference software for finding Chebyshev best-fit geometric elements," *Precision Engineering*, vol. 19, no. 1, pp. 28–36, 1996.

[52] C. M. Shakarji and A. Clement, "Reference Algorithms for Chebyshev and One-Sided Data Fitting for Coordinate Metrology," *CIRP Annals - Manufacturing Technology*, vol. 53, no. 1, pp. 439–442, 2004.

[53] J. P. Boyd and R. Petschek, "The relationships between Chebyshev, Legendre and Jacobi polynomials: The generic superiority of chebyshev polynomials and three important exceptions," *Journal of Scientific Computing*, vol. 59, no. 1, pp. 1–27, 2014.

[54] T. Hopp, “Computational metrology.pdf,” *Manufacturing Review*, vol. 6, no. 4, pp. 295–304, 1993.

[55] V. Srinivasan, “Computational Metrology for the Design and Manufacture of Product Geometry: A Classification and Synthesis,” *Journal of Computing and Information Science in Engineering*, vol. 7, no. 1, p. 3, 2007.

[56] G. Goch and K. Luebke, “Tschebyscheff approximation for the calculation of maximum inscribed/minimum circumscribed geometry elements and form deviations,” *CIRP Annals - Manufacturing Technology*, vol. 57, no. 1, pp. 517–520, 2008.

[57] R. W. Hamming, “Numerical Methods for Scientists and Engineers,” *Numerical Methods for Scientists and Engineers*. pp. 393–411, 1973.

[58] J. C. Mason and D. C. Handscomb, *CHEBYSHEV POLYNOMIALS*. 2003.

[59] J. P. Boyd, “Chebyshev and Fourier Spectral Methods,” *New York*, p. 688, 2000.

[60] K. J. Stout, P. J. Sullivan, and P. A. McKeown, “The Use of 3-D Topographic Analysis to Determine the Microgeometric Transfer Characteristics of Textured Sheet Surfaces through Rolling,” *CIRP Annals - Manufacturing Technology*, vol. 41, no. 1, pp. 621–624, 1992.

[61] Y. Peng, “Personal communication.” 2017.

[62] X. J. Jiang and D. J. Whitehouse, “Technological shifts in surface metrology,” *CIRP Annals - Manufacturing Technology*, vol. 61, no. 2, pp. 815–836, Jan. 2012.

[63] Mathworks, “Trapezoidal numerical integration,” 2017. [Online]. Available: https://www.mathworks.com/help/matlab/ref/trapz.html.

[64] D. T. Lee and B. J. Schachter, “Two algorithms for constructing a Delaunay triangulation,” *International Journal of Computer & Information Sciences*, vol. 9, no. 3, pp. 219–242, 1980.

[65] S. A. Khayam, “The Discrete Cosine Transform (DCT): Theory and Application,” *Components*, 2003.

[66] Mathworks, “2-D discrete cosine transform,” 2017. [Online]. Available: https://www.mathworks.com/help/images/ref/dct2.html?searchHighlight=dct2&s_tid=doc_srchtitle.

[67] R. J. Hocken and P. H. Pereira, *Coordinate Measuring Machines and Systems*, 2nd ed. CRC Press, 2012.

[68] J. Y. Wang and D. E. Silva, “Wave-front interpretation with Zernike polynomials.,” *Applied optics*, vol. 19, no. 9, pp. 1510–8, 1980.

[69] C. J. Kim, “Polynomial fit of interferograms.,” *Applied optics*, vol. 21, no. 24, pp. 4521–5, 1982.

[70] Y. Li and P. Gu, “Free-form surface inspection techniques state of the art review,” *CAD Computer Aided Design*, vol. 36, no. 13, pp. 1395–1417, 2004.

[71] FRENCO, “IC - Gear Artefacts The solution to determine the measurement uncertainty,” 2013. [Online]. Available: http://www.eurotechcorp.com/eurotech/PDFs/2013GearArtefacts.pdf.

APPENDIX A: DERIVATION OF 3D NOMINAL HELICAL SURFACE

The parametric representation is:

$$\begin{cases} u = r_{\mathrm{b}}\xi_{\mathrm{nom}} = r_{\mathrm{b}}\xi \\ v = z_{\mathrm{nom}} = z \end{cases}$$

The starting angle is :

$$\Lambda = \eta_{\mathrm{b}} + z\frac{\tan\beta_{\mathrm{b}}}{r_{\mathrm{b}}}$$

Take the partial derivative at nominal point with respect to u:

$$\frac{\partial P_{\mathrm{nom}}}{\partial u} = \begin{pmatrix} \frac{\partial x_{\mathrm{nom}}}{\partial u} \\ \frac{\partial y_{\mathrm{nom}}}{\partial u} \\ \frac{\partial z_{\mathrm{nom}}}{\partial u} \end{pmatrix} = \begin{pmatrix} \frac{\partial x_{\mathrm{nom}}}{\partial \xi}\frac{\partial \xi}{\partial u} \\ \frac{\partial y_{\mathrm{nom}}}{\partial \xi}\frac{\partial \xi}{\partial u} \\ \frac{\partial z_{\mathrm{nom}}}{\partial \xi}\frac{\partial \xi}{\partial u} \end{pmatrix}$$

$$\frac{\partial P_{\mathrm{nom}}}{\partial u} = \begin{pmatrix} -\sin(\xi+\Lambda)\left(1+\frac{\partial \Lambda}{\partial \xi}\right) + \sin(\xi+\Lambda) + \xi\cos(\xi+\Lambda)\left(1+\frac{\partial \Lambda}{\partial \xi}\right) \\ \cos(\xi+\Lambda)\left(1+\frac{\partial \Lambda}{\partial \xi}\right) - \cos(\xi+\Lambda) + \xi\sin(\xi+\Lambda)\left(1+\frac{\partial \Lambda}{\partial \xi}\right) \\ 0 \end{pmatrix}$$

$$= \begin{pmatrix} \xi\cos(\xi+\Lambda) + \frac{\partial \Lambda}{\partial \xi}[-\sin(\xi+\Lambda) + \xi\cos(\xi+\Lambda)] \\ \xi\sin(\xi+\Lambda) + \frac{\partial \Lambda}{\partial \xi}[\cos(\xi+\Lambda) + \xi\sin(\xi+\Lambda)] \\ 0 \end{pmatrix} = \begin{pmatrix} \xi\cos(\xi+\Lambda) \\ \xi\sin(\xi+\Lambda) \\ 0 \end{pmatrix}.$$

Taking the partial derivative at nominal point with respect to v:

$$\frac{\partial P_{\mathrm{nom}}}{\partial v} = \frac{\partial P_{\mathrm{nom}}}{\partial z} = \begin{pmatrix} \frac{\partial x_{\mathrm{nom}}}{\partial z} \\ \frac{\partial y_{\mathrm{nom}}}{\partial z} \\ \frac{\partial z_{\mathrm{nom}}}{\partial z} \end{pmatrix}$$

$$\frac{\partial P_{\text{nom}}}{\partial v} = \begin{pmatrix} r_{\text{b}}[-\sin(\xi+\Lambda)\frac{\partial \Lambda}{\partial z} + \xi\cos(\xi+\Lambda)\frac{\partial \Lambda}{\partial z} \\ r_{\text{b}}[\cos(\xi+\Lambda)\frac{\partial \Lambda}{\partial z} + \xi\cdot\sin(\xi+\Lambda)\frac{\partial \Lambda}{\partial z} \\ 1 \end{pmatrix}$$

$$= \begin{pmatrix} \frac{\partial \Lambda}{\partial z} r_{\text{b}}[-\sin(\xi+\Lambda) + \xi\cos(\xi+\Lambda)] \\ \frac{\partial \Lambda}{\partial z} r_{\text{b}}[\cos(\xi+\Lambda) + \xi\sin(\xi+\Lambda)] \\ 1 \end{pmatrix} = \begin{pmatrix} -\frac{\partial \Lambda}{\partial z} y_{\text{nom}} \\ \frac{\partial \Lambda}{\partial z} x_{\text{nom}} \\ 1 \end{pmatrix}$$

$$= \begin{pmatrix} -\frac{\tan\beta_{\text{b}}}{r_{\text{b}}} y_{\text{nom}} \\ \frac{\tan\beta_{\text{b}}}{r_{\text{b}}} x_{\text{nom}} \\ 1 \end{pmatrix}$$

Taking cross product of two vectors:

$$\frac{\partial P_{\text{nom}}}{\partial u} \times \frac{\partial P_{\text{nom}}}{\partial z} = \begin{pmatrix} \xi\cos(\xi+\Lambda) \\ \xi\sin(\xi+\Lambda) \\ 0 \end{pmatrix} \times \begin{pmatrix} -\frac{\tan\beta_{\text{b}}}{r_{\text{b}}} y_{\text{nom}} \\ \frac{\tan\beta_{\text{b}}}{r_{\text{b}}} x_{\text{nom}} \\ 1 \end{pmatrix} = \begin{pmatrix} \xi\sin(\xi+\Lambda) \\ -\xi\cos(\xi+\Lambda) \\ \xi\tan\beta_{\text{b}} \end{pmatrix}$$

to obtain surface normal vector:

$$\vec{N} = \begin{pmatrix} \xi\sin(\xi+\Lambda) \\ -\xi\cos(\xi+\Lambda) \\ \xi\tan\beta_{\text{b}} \end{pmatrix}$$

which can be normalized to:

$$\vec{n} = \frac{\vec{N}}{|\vec{N}|} = \frac{1}{\xi\sqrt[2]{1+(\tan\beta_{\text{b}})^2}} \begin{pmatrix} \xi\sin(\xi+\Lambda) \\ -\xi\cos(\xi+\Lambda) \\ \xi\tan\beta_{\text{b}} \end{pmatrix}$$

$$\vec{n} = \frac{1}{\sqrt[2]{1+(\tan\beta_{\text{b}})^2}} \begin{pmatrix} \sin(\xi+\Lambda) \\ -\cos(\xi+\Lambda) \\ \tan\beta_{\text{b}} \end{pmatrix}$$

APPENDIX B: DERIVATION OF PLUMB LINE DISTANCE

Vectorial equation between nominal point and the measured point:

$$\vec{p}_{\mathrm{m}} = \vec{p}_{\mathrm{nom}} + \vec{d}_{\mathrm{lot}} = \vec{p}_{\mathrm{nom}} + \left|\vec{d}_{\mathrm{lot}}\right| \cdot \vec{n}$$

Using the explicit expression of unit surface normal vector:

$$\begin{pmatrix} x_{\mathrm{m}} \\ y_{\mathrm{m}} \\ z_{\mathrm{m}} \end{pmatrix} = \begin{pmatrix} x_{\mathrm{nom}} \\ y_{\mathrm{nom}} \\ z_{\mathrm{nom}} \end{pmatrix} + \frac{\left|\vec{d}_{\mathrm{lot}}\right|}{\sqrt[2]{1 + (\tan\beta_{\mathrm{b}})^2}} \begin{pmatrix} \sin(\xi + \Lambda) \\ -\cos(\xi + \Lambda) \\ \tan\beta_{\mathrm{b}} \end{pmatrix}$$

$$= \begin{pmatrix} r_{\mathrm{b}} \cdot [\cos(\xi + \Lambda) + \xi \cdot \sin(\xi + \Lambda)] + \dfrac{\left|\vec{d}_{\mathrm{lot}}\right|}{\sqrt[2]{1 + (\tan\beta_{\mathrm{b}})^2}} \cdot \sin(\xi + \Lambda) \\ r_{\mathrm{b}} \cdot [\sin(\xi + \Lambda) - \xi \cdot \cos(\xi + \Lambda)] - \dfrac{\left|\vec{d}_{\mathrm{lot}}\right|}{\sqrt[2]{1 + (\tan\beta_{\mathrm{b}})^2}} \cdot \cos(\xi + \Lambda) \\ z + \dfrac{\left|\vec{d}_{\mathrm{lot}}\right|}{\sqrt[2]{1 + (\tan\beta_{\mathrm{b}})^2}} \cdot \tan\beta_{\mathrm{b}} \end{pmatrix}$$

$$= \begin{pmatrix} r_{\mathrm{b}} \cdot [\cos(\xi + \Lambda) + \xi \cdot \sin(\xi + \Lambda) + \dfrac{\left|\vec{d}_{\mathrm{lot}}\right| \cdot \sin(\xi + \Lambda)}{r_{\mathrm{b}} \cdot \sqrt[2]{1 + (\tan\beta_{\mathrm{b}})^2}}] \\ r_{\mathrm{b}} \cdot [\sin(\xi + \Lambda) - \xi \cdot \cos(\xi + \Lambda) \dfrac{\left|\vec{d}_{\mathrm{lot}}\right|}{r_{\mathrm{b}} \cdot \sqrt[2]{1 + (\tan\beta_{\mathrm{b}})^2}} \cdot \cos(\xi + \Lambda)] \\ z + \dfrac{\left|\vec{d}_{\mathrm{lot}}\right|}{\sqrt[2]{1 + (\tan\beta_{\mathrm{b}})^2}} \cdot \tan\beta_{\mathrm{b}} \end{pmatrix}$$

$$= \begin{pmatrix} r_{\mathrm{b}} \cdot [\cos(\xi + \Lambda) + \left(\xi + \dfrac{\left|\vec{d}_{\mathrm{lot}}\right|}{r_{\mathrm{b}} \cdot \sqrt[2]{1 + (\tan\beta_{\mathrm{b}})^2}}\right) \cdot \sin(\xi + \Lambda)] \\ r_{\mathrm{b}} \cdot [\sin(\xi + \Lambda) - \left(\xi + \dfrac{\left|\vec{d}_{\mathrm{lot}}\right|}{r_{\mathrm{b}} \cdot \sqrt[2]{1 + (\tan\beta_{\mathrm{b}})^2}}\right) \cdot \cos(\xi + \Lambda)] \\ z + \dfrac{\left|\vec{d}_{\mathrm{lot}}\right|}{\sqrt[2]{1 + (\tan\beta_{\mathrm{b}})^2}} \cdot \tan\beta_{\mathrm{b}} \end{pmatrix}$$

The expression of the plumb line distance equation in Cartesian coordinate system is:

$$|\vec{d}_{\mathrm{lot}}| = \frac{r_b}{\sqrt{1+(\tan\beta_{\mathrm{b}})^2}}\left\{\sqrt{\frac{x_{\mathrm{m}}^2+y_{\mathrm{m}}^2}{r_{\mathrm{b}}^2}-1} - \operatorname{atan}\left(\sqrt{\frac{x_{\mathrm{m}}^2+y_{\mathrm{m}}^2}{r_{\mathrm{b}}^2}-1}\right) - \operatorname{atan}\left(\frac{y_{\mathrm{m}}}{x_{\mathrm{m}}}\right) + \eta_{\mathrm{b}} + z_{\mathrm{m}}\cdot\frac{\tan\beta_{\mathrm{b}}}{r_{\mathrm{b}}}\right\}$$

Converting the plumb line distance equation from Cartesian coordinate system to cylindrical coordinate system

$$\rho_{\mathrm{m}} = \sqrt[2]{x_{\mathrm{m}}^2+y_{\mathrm{m}}^2} = r_{\mathrm{b}}\cdot\sqrt[2]{1+\left(\xi+\frac{|\vec{d}_{\mathrm{lot}}|}{r_{\mathrm{b}}\cdot\sqrt[2]{1+(\tan\beta_{\mathrm{b}})^2}}\right)^2}$$

$$\phi_{\mathrm{m}} = \arctan\left(\frac{y_{\mathrm{m}}}{x_{\mathrm{m}}}\right)$$

$$= \arctan\left[\frac{\sin(\xi+\Lambda)-\left(\xi+\frac{|\vec{d}_{\mathrm{lot}}|}{r_{\mathrm{b}}\cdot\sqrt[2]{1+(\tan\beta_{\mathrm{b}})^2}}\right)\cdot\cos(\xi+\Lambda)}{\cos(\xi+\Lambda)+\left(\xi+\frac{|\vec{d}_{\mathrm{lot}}|}{r_{\mathrm{b}}\cdot\sqrt[2]{1+(\tan\beta_{\mathrm{b}})^2}}\right)\cdot\sin(\xi+\Lambda)}\right]$$

$$= \arctan\left[\frac{\tan(\xi+\Lambda)+\left(\xi+\frac{|\vec{d}_{\mathrm{lot}}|}{r_{\mathrm{b}}\cdot\sqrt[2]{1+(\tan\beta_{\mathrm{b}})^2}}\right)}{1-\left(\xi+\frac{|\vec{d}_{\mathrm{lot}}|}{r_{\mathrm{b}}\cdot\sqrt[2]{1+(\tan\beta_{\mathrm{b}})^2}}\right)\cdot\tan(\xi+\Lambda)}\right]$$

$$= \arctan\left[\tan\left(\xi+\Lambda-\arctan\left(\xi+\frac{|\vec{d}_{\mathrm{lot}}|}{r_{\mathrm{b}}\cdot\sqrt[2]{1+(\tan\beta_{\mathrm{b}})^2}}\right)\right)\right]$$

$$= \xi+\Lambda-\arctan\left(\xi+\frac{|\vec{d}_{\mathrm{lot}}|}{r_b\cdot\sqrt[2]{1+(\tan\beta_{\mathrm{b}})^2}}\right)$$

$$z_{\mathrm{m}} = z_{\mathrm{nom}} + \frac{\left|\vec{d}_{\mathrm{lot}}\right|}{\sqrt[2]{1+(\tan\beta_{\mathrm{b}})^2}} \cdot \tan\beta_{\mathrm{b}}$$

In summary:

$$\begin{cases} \rho_{\mathrm{m}} = r_{\mathrm{b}} \cdot \sqrt[2]{1+\left(\xi + \dfrac{\left|\vec{d}_{\mathrm{lot}}\right|}{r_{\mathrm{b}}\sqrt[2]{1+(\tan\beta_{\mathrm{b}})^2}}\right)^2} \\ \phi_{\mathrm{m}} = \xi + \Lambda - \arctan\left(\xi + \dfrac{\left|\vec{d}_{\mathrm{lot}}\right|}{r_b\sqrt[2]{1+(\tan\beta_{\mathrm{b}})^2}}\right) \\ z_{\mathrm{m}} = z_{\mathrm{nom}} + \dfrac{\left|\vec{d}_{\mathrm{lot}}\right|}{\sqrt[2]{1+(\tan\beta_{\mathrm{b}})^2}} \cdot \tan\beta_{\mathrm{b}} \end{cases}$$

The expression of the plumb line distance equation is cylindrical coordinate system is:

$$\left|\vec{d}_{\mathrm{lot}}\right| = \frac{r_{\mathrm{b}}}{\sqrt{1+(\tan\beta_{\mathrm{b}})^2}}\left\{\sqrt{\frac{\rho_{\mathrm{m}}^2}{r_{\mathrm{b}}^2}-1} - \arctan\left(\sqrt{\frac{\rho_{\mathrm{m}}^2}{r_{\mathrm{b}}^2}-1}\right) - \phi_{\mathrm{m}} + \eta_{\mathrm{b}} + z_{\mathrm{m}} \cdot \frac{\tan\beta_{\mathrm{b}}}{r_{\mathrm{b}}}\right\}$$